



저작자표시-비영리-변경금지 2.0 대한민국

이용자는 아래의 조건을 따르는 경우에 한하여 자유롭게

- 이 저작물을 복제, 배포, 전송, 전시, 공연 및 방송할 수 있습니다.

다음과 같은 조건을 따라야 합니다:



저작자표시. 귀하는 원저작자를 표시하여야 합니다.



비영리. 귀하는 이 저작물을 영리 목적으로 이용할 수 없습니다.



변경금지. 귀하는 이 저작물을 개작, 변형 또는 가공할 수 없습니다.

- 귀하는, 이 저작물의 재이용이나 배포의 경우, 이 저작물에 적용된 이용허락조건을 명확하게 나타내어야 합니다.
- 저작권자로부터 별도의 허가를 받으면 이러한 조건들은 적용되지 않습니다.

저작권법에 따른 이용자의 권리는 위의 내용에 의하여 영향을 받지 않습니다.

이것은 [이용허락규약\(Legal Code\)](#)을 이해하기 쉽게 요약한 것입니다.

[Disclaimer](#)

의학박사 학위논문

Comprehensive studies on Kv4.1 and Kv4.2 in
mature granule cells of hippocampal dentate gyrus:
distinct roles, subcellular distributions, and
pathophysiological implications

해마 치상회의 성숙한 과립세포에서 Kv4.1 과
Kv4.2 의 구분된 역할, 세포 이하에서의 분포,
병리학적 영향에 대한 종합적인 연구

2017 년 02 월

서울대학교 대학원
의과학과 생리학전공
김 경 란

A thesis of the Degree of Doctor of Philosophy

해마 치상회의 성숙한 과립세포에서 Kv4.1 과
Kv4.2 의 구분된 역할, 세포 이하에서의 분포,
병리학적 영향에 대한 종합적인 연구

Comprehensive studies on Kv4.1 and Kv4.2 in
mature granule cells of hippocampal dentate gyrus:
distinct roles, subcellular distributions, and
pathophysiological implication

February 2017

The Department of Biomedical Sciences,
Seoul National University
College of Medicine
Kyung-Ran Kim

해마 치상회의 성숙한 과립세포에서 Kv4.1 과
Kv4.2 의 구분된 역할, 세포 이하에서의 분포,
병리학적 영향에 대한 종합적인 연구

지도교수 호 원 경

이 논문을 의학박사 학위논문으로 제출함

2016년 12월

서울대학교 대학원
의과학과 생리학전공
김 경 란

김경란의 의학박사 학위논문을 인준함

2016년 12월

위 원 장 _____ (인)
부위원장 _____ (인)
위 원 _____ (인)
위 원 _____ (인)
위 원 _____ (인)

Comprehensive studies on Kv4.1 and Kv4.2 in
mature granule cells of hippocampal dentate gyrus:
distinct roles, subcellular distributions, and
pathophysiological implication

by
Kyung-Ran Kim

A thesis submitted to the Department of
Biomedical Sciences in partial fulfillment of the
requirements for the Degree of Doctor of
Philosophy in Medical Science at Seoul National
University College of Medicine

December 2016

Approved by Thesis Committee:

Professor _____ Chairman
Professor _____ Vice chairman
Professor _____
Professor _____
Professor _____

ABSTRACT

Comprehensive studies on Kv4.1 and Kv4.2 in mature granule cells of hippocampal dentate gyrus: distinct roles, subcellular distributions, and pathophysiological implication

Background: Dentate gyrus (DG), the main gateway to the hippocampus and where adult neurogenesis occurs, play key roles in pattern separation by forming distinct representation of similar inputs. Sparse action potential generation in dentate gyrus granule cells (DG-GCs) has been thought as a cellular mechanism of pattern separation. The balance between excitatory and inhibitory synaptic inputs was reported to be important for determining low excitability of DG-GCs, but the ion channel mechanisms underlying sparse action potential firing remain unclear. Calbindin-D_{28K} (CB) is a major Ca²⁺ buffer in DG-GCs of the hippocampus. Reduction of CB expression in DG-GCs is reported in various pathologic conditions that accompany with cognitive dysfunction, including Alzheimer's disease (AD). However, the link between intracellular Ca²⁺ dysregulation and neuronal excitability in DG-GCs has not been investigated.

Methods: I investigated the mechanism of sparse action potential firing in DG-GCs at the age of 1–2 months old mice, and examined how this mechanism was altered in transgenic mice (Alzheimer’s disease model mice (Tg2576) and Calbindin-D_{28K} knock-out mice (CBKO)). Using voltage- and current-clamp techniques, voltage-dependent K⁺ currents and intrinsic excitability of DG-GCs and CA1 pyramidal cells (PCs) in acute brain slices were analyzed. For molecular analysis, quantitative real-time reverse transcription PCR (qRT-PCR), Western blot, and immunohistochemistry were performed. Anti-Kv4.1 and anti-Kv4.2 antibodies were used for selective blockade of corresponding ion channels as well as molecular analysis. Behavior tests for analyzing pattern separation were performed in control, Tg2576, and CBKO mice.

Results: Immunohistochemistry analysis showed that Kv4.1 subunits are strongly expressed in mature DG-GCs, but weak in CA1 in the hippocampus. Whole-cell current clamp analysis showed that Kv4.1 antibody increased firing frequency in mature DG-GCs, but did not affect any parameters of intrinsic excitability in immature DG-GCs and CA1 PCs, suggesting that Kv4.1 play a selective role in limiting firing frequency of mature

DG-GCs. Whole-cell voltage-clamp analysis revealed that Kv4.1-mediated currents ($I_{Kv4.1}$) in DG-GCs have distinct properties from A-type K^+ channels, showing slow inactivation kinetics and sensitivity to intracellular Ca^{2+} . Reduction of Kv4.1 expression in DG was found in CBKO and Tg2576 mice. Consistently, firing frequency in mature DG-GCs was increased in CBKO and Tg2576 mice. Furthermore, CBKO and Tg2576 mice showed a deficit in pattern separation without impairment in memory acquisition, supporting the link between sparse firing of DG-GCs and pattern separation. Unexpectedly, I found that the endogenous Ca^{2+} buffer capacity in mature DG-GCs was reduced in Tg2576 mice to a level comparable to CBKO mice. The reduction of Ca^{2+} buffering in Tg2576 DG-GCs was mimicked by the exogenous application of oligomeric amyloid β ($A\beta$)₁₋₄₂ protein and restored by the antioxidant Trolox, suggesting that $A\beta$ -induced oxidative stress induces CB dysfunction in Tg2576 mice. When Tg2576 mice were treated with Trolox for 1 week, hyperexcitability of DG-GCs and impairment of pattern separation were restored.

Conclusion: These data suggest that Kv4.1 channels, selectively expressed in DG-GCs and acting as a regulator to prevent

hyperexcitability of DG-GCs, are essential for pattern separation. Reduction of Kv4.1 expression in AD and CBKO mice suggests the pathophysiological significance of Kv4.1 in various conditions causing Ca²⁺ dysregulation.

Keywords: somatic intrinsic property, dentate gyrus mature granule cell, CA1 pyramidal cell, A-type K⁺ channel, Kv4.1, Kv4.2, Calbindin-D_{28K}, Alzheimer's disease

Student number: 2009-23550

CONTENTS

Abstract	i
Contents	v
List of tables and figures	vii
List of Abbreviations.....	xi
Chapter 1	2
Role of Kv4.1 in intrinsic properties of dentate gyrus mature granule cells	
Introduction.....	3
Material and Methods.....	7
Results.....	20
Discussion.....	86
Chapter 2.....	93
Links between reduced expression of Kv4.1 and hyperexcitability of dentate granule cell in Alzheimer's disease model mice	
Introduction.....	94
Material and Methods.....	97
Results.....	102
Discussion.....	131

References	139
Abstract in Korean.....	161

LIST OF TABLES AND FIGURES

Chapter 1

Figure 1	Immunofluorescent localization of the Kv4.1 and Kv4.2 subunit in hippocampus region.....	47
Figure 2	Inhibition of total K^+ current in Kv4.1-expressing HEK 293T cells using anti-Kv4.1 or anti-Kv4.2 antibody.....	49
Figure 3	Inhibition of total outward K^+ current in hippocampal cell types using anti-Kv4.1 antibody.....	51
Figure 4	Expression of Kv4.1 channel during the maturation of DG-GCs.....	53
Figure 5	Comparison of intrinsic property between mature and immature GCs.....	55
Figure 6	Comparison of electrical properties and contribution of anti-Kv4.1 antibody on firing frequency between mature and immature DG-GCs.....	57
Figure 7	Contribution of anti-Kv4.2 antibody on firing frequency in mature DG-GCs.....	59
Figure 8	Scheme of K^+ current measurements in	

	hippocampal cells	61
Figure 9	Comparison of K^+ current between mature and immature DG-GCs.....	62
Figure 10	Characterization of Kv4.1-mediated currents using anti-Kv4.1 antibody	64
Figure 11	Contribution of D-type currents in mature DG-GCs.....	66
Figure 12	Contribution of KCNQ/M channel in mature DG-GCs.....	68
Figure 13	Ca^{2+} -sensitivity of Kv4.1-mediated currents in mature DG-GCs.....	69
Figure 14	Contribution of Kv4.1 and comparison of outward K^+ current in CA1-PCs.	71
Figure 15	Selective downregulation of Kv4.1 expression and $I_{Kv4.1}$ in DG of CBKO.....	74
Figure 16	Contribution of I_{TEA} and I_D in CBKO mature DG-GCs.....	77
Figure 17	Increased firing frequency in mature DG-GCs of CBKO.....	79
Figure 18	Firing frequency of CA1-PCs in Control and CBKO mice.....	81
Figure 19	The level of anxiety and locomotor activity between Control and CBKO mice.....	82

Figure 20	Impaired pattern separation in CBKO mice.....	83
Table 1	Double exponential fitting data of I_{4-AP} at +30 mV.....	85

Chapter 2

Figure 1	Estimation of endogenous Ca^{2+} binding ratios (κ_E) in WT and Tg2576 mature DG-GCs.....	116
Figure 2	Hyperexcitability of mature DG-GCs in Tg2576	118
Figure 3	K^+ current measurements in mature DG-GCs .	120
Figure 4	TEA and 40 μ M 4-AP sensitive K^+ current in WT and Tg2576 mature DG-GCs.....	122
Figure 5	Reduced sustained component of 5 mM 4-AP sensitive current in Tg2576 mature DG-GCs.	124
Figure 6	Effects of pre-treatment with Trolox in the Tg2576 and CBKO mice	126
Figure 7	Impaired pattern separation in Tg2576 mice restored by Trolox	128
Table 1	The threshold current for AP generation and passive electrical properties of mature DG-	

GCs..... 130

LIST OF ABBREVIATIONS

DG	Dentate gyrus
GCs	Granule cells
PCs	Pyramidal cells
GCL	Granule cell layer
ML	Molecular layer
Pyr	Pyramidal layer
Rad	Striatum radiatum
4-AP	4-aminopyridine
MAP-2	Microtubule associated protein 2
F	Fluorescence intensity
Kv	Voltage gated K channel
$I_{Kv4.1}$	Kv4.1-mediated current
IHC	Immunohistochemistry
AP	Action potential
I	Injected current
F	Firing frequency
RMP	Resting membrane potential
R_{in}	Input resistance
CB	Calbindin-D _{28K}
CBKO	Calbindin-D _{28K} Knockout
TEA	Tetraethylammonium chloride
I_{TEA}	TEA sensitive current
I_D	D-type potassium current

I _A	A-type potassium current
I _{4-AP}	4-aminopyridine sensitive current
HEK293T	Human embryonic kidney 293T cell
PFA	Paraformaldehyde
PBS	Phosphate buffered saline
PBS-T	Phosphate buffered saline with 0.3% Triton X-100
RT	Room temperature
AD	Alzheimer's disease
qRT-PCR	Quantitative real-time reverse transcription polymerase chain reaction
TTX	Tetrodotoxin
CNQX	6-cyano-7-nitroquinoxaline-2,3-dione
DCX	Doublecortin
PW	Postnatal week
aCSF	Artificial cerebrospinal fluid
DIC	Differential interference contrast
ROI	Region of interest
κ_E	Endogenous calcium binding ratios
CaTs	Evoked Ca ²⁺ transients
ROS	Reactive oxygen species
i.p.	Intraperitoneal

CHAPTER 1

Role of Kv4.1 in intrinsic properties
of dentate gyrus mature granule
cells

INTRODUCTION

The hippocampus is important for new memory acquisition, the storage of memory independently of each other, and memory retrieval from partial cues. Each subregion within the hippocampus (dentate gyrus (DG), CA3, and CA1) may contribute differently to these memory processes, but the underlying mechanisms are poorly understood. Different features of each region in network configuration are considered to play important roles in different cognitive functions (Rolls and Kesner, 2006). For example, a previous computational modeling study suggests that extensive autoassociative networks in the CA3 area underlie pattern completion (McNaughton and Morris, 1987). On the other hand, sparse activity of dentate granule cells (DG-GCs) and the low innervation ratio of dentate mossy fibers to CA3 pyramidal cells (PCs) are key mechanisms underlying pattern separation (Marr, 1971; O'Reilly and McClelland, 1994; Rolls, 2013; Treves and Rolls, 1994). The role of CA1 is also poorly understood, but it was suggested that CA1 is neither separating nor completing, but exhibits a linear transformation (Vazdarjanova and

Guzowski, 2004; Yassa and Stark, 2011).

A hallmark of the DG is the continuous production of new neurons that develop over several weeks to integrate into the circuitry, and grow further over several months to reach full maturation (Dieni et al., 2013; van Praag et al., 2002). It has been of great interest to elucidate functional changes during maturation. In particular, the mechanism of low excitability of DG-GCs has been extensively investigated, because function of DG in pattern separation relies on sparse firing (Jinde et al., 2012). The decision to fire action potentials is determined by a combination of synaptic drives and intrinsic excitability, but previous studies have focused on changes in synaptic inputs, showing that the increase in the inhibitory to excitatory ratio during maturation is the major mechanism of low excitability of mature DG-GCs (Dieni et al., 2013; Marin-Burgin et al., 2012). The contribution of intrinsic excitability to firing properties of DG-GCs remains to be elucidated.

A-type K^+ currents, I_A , which are characterized by their rapid inactivation kinetics and sensitivity to 4-aminopyridine (4-AP) blockade, play a key role in the regulation of neuronal excitability in various brain regions,

including the hippocampus (Hoffman et al., 1997; Locke and Nerbonne, 1997; Ramakers and Storm, 2002; Shibata et al., 2000). The Kv4 gene subfamily, consisting of Kv4.1, Kv4.2, and Kv4.3, is known to mediate I_A (Baldwin et al., 1991; Pak et al., 1991; Serodio et al., 1996). Kv4.2 is the most abundant isoform and the major contributor to I_A in hippocampal CA1 pyramidal cells (CA1-PCs) (Kim et al., 2005; Martina et al., 1998; Serodio and Rudy, 1998), whereas Kv4.3 is selectively distributed in specific subpopulations of interneurons and regulates intrinsic rhythmic activity (Bourdeau et al., 2007). When expressed in heterologous expression systems, Kv4.1 has similar electrophysiological and pharmacological properties to those of Kv4.2 and Kv4.3 (Pak et al., 1991), but the role of Kv4.1 in native neurons is little understood. Kv4.1 is expressed only in the restricted regions of the brain with a low expression level, and it is interesting to note that DG-GCs show relatively stronger signals than other regions (Martina et al., 1998; Serodio and Rudy, 1998). However, functional significance of Kv4.1 expression in DG-GCs has never been investigated.

In the present study, I characterized Kv4.1-mediated currents ($I_{Kv4.1}$) and investigated its role in control of the

excitability of DG-GCs. I found that $I_{Kv4.1}$ are distinct from classical I_A , showing a slow inactivation kinetics, and that blockade of $I_{Kv4.1}$ results in increases in firing frequency without changes in other parameters for intrinsic excitability in DG-GCs. I also found that immature DG-GCs in contrast do not exhibit Kv4.1 channels and when blocking $I_{Kv4.1}$ no evident changes take place in firing frequency. Furthermore, I also found that dysregulation of Ca^{2+} homeostasis caused by calbindin-D_{28K} (CB) knockout (CBKO) resulted in downregulation of Kv4.1 mRNA expression, increased firing rates in DG-GCs, and impaired pattern separation. My study highlights the exclusive role of Kv4.1 in the maintenance of low intrinsic excitability in mature DG-GCs and provides evidence for the pathophysiological significance of Kv4.1 downregulation.

MATERIALS AND METHODS

1. Hippocampal slice preparation

Brain slices were prepared from male control mice and calbindin-D_{28K} (CB) knockout (CBKO) mice aged from 1 to 2 months old. Average ages of control and CBKO mice used in the present study were 5.7 (n = 75) and 5.8 (n = 53) week, respectively. Experiments for DG-GCs were mostly conducted using mice at postnatal week (PW) 4 to PW 7, while experiments for CA1-3 PCs were conducted using mice at PW 3 to PW 4. Mice were sacrificed by decapitation after being anesthetized with isoflurane, and the whole brain was immediately removed from the skull and chilled in artificial cerebrospinal fluid (aCSF) at 4 °C. Transverse hippocampal slices (350 μm thick) were prepared using a vibratome (VT1200S, Leica, Germany). All experimental procedures were conducted in accordance with the guidelines of University Committee on Animal Resource in Seoul National University (Approval No. SNU-090115-7). Slices were incubated at 35 °C for 30 min and thereafter maintained at 32 °C until recording.

2. *In vitro* electrophysiological recording

Hippocampal principal neurons were visualized using an upright microscope equipped with differential interference contrast (DIC) optics (BX51WI, Olympus, Japan). Electrophysiological recordings were made by the whole-cell patch clamp technique with EPC-8 amplifier (HEKA, Lambrecht, Germany). Experiments were performed at 32 ± 1 °C. After break-in, I waited 5 min to stabilize neurons. The perfusion rate of bathing solution and the volume of the recording chamber for slices were 2.2 ml/min and 1.2 ml, respectively. Patch pipettes with a tip resistance of 3 - 4 M Ω were used. The series resistance (R_s) after establishing whole-cell configuration was between 10 and 15 M Ω . Cell were discarded and excluded from analysis if the R_s changed by >20 % of baseline value and/or exceeded 30 M Ω . The pipette solution contained (in mM): 143 K-gluconate, 7 KCl, 15 HEPES, 4 MgATP, 0.3 NaGTP, 4 Na-ascorbate, and 0.1 EGTA with the pH adjusted to 7.3 with KOH. For the antibody-blocking experiments, patch pipettes were dipped into an internal solution and then back-filled with the internal solution containing the antibody of Kv4.1 or Kv4.2 at a

concentration of 0.3 $\mu\text{g/ml}$. The bath solution (or aCSF) for the control experiments contained the followings (in mM): 125 NaCl, 25 NaHCO_3 , 2.5 KCl, 1.25 NaH_2PO_4 , 2 CaCl_2 , 1 MgCl_2 , 20 glucose, 1.2 pyruvate and 0.4 Na-ascorbate, pH 7.4 when saturated with carbogen (95% O_2 and 5% CO_2). In all bath solutions, 20 μM bicuculline and 10 μM CNQX were included to block the synaptic inputs. In current-clamp experiments to analyze neuronal excitability, the following parameters were measured: (1) the resting membrane potential (RMP), (2) the input resistance (R_{in} , membrane potential changes for given hyperpolarizing current input (-35 pA, 600 ms)), (3) F-I curve (firing frequencies (F) against the amplitude of injected currents (I), for DG-GCs; 100 pA to 600 pA with 100 pA increment, subset of experiments, 50 pA to 350 pA with 50 pA increment, 1 s duration, for CA1-PCs; 50 pA to 250 pA with 50 pA increment, subset of experiments, 25 pA to 200 pA with 25 pA increment, 1 s duration), (4) AP onset time (the delay from the start of depolarized current injection to the beginning of the upstroke phase of the 1st evoked AP), (5) Rheobase (current threshold for single action potential generation, 100 ms duration), (6) Overshoot (defined as the difference voltage

from 0 mV to peak voltage), (7) AP halfwidth (measured as the width at half-maximal spike amplitude, (8) AP threshold (change in membrane potential at a rate of 50 V/s). All chemicals were obtained from Sigma (St. Louis, MO, USA), except CNQX, bicuculline, and TTX from abcam Biochemicals (Cambridge, UK).

3. Outward K⁺ current recording

Whole-cell, voltage-gated K⁺ currents from DG-GCs and CA1-PCs were evoked in response to 1 s voltage steps to potentials between -60 mV to +50 mV from a holding potential of -70 mV. To measure K⁺ currents, I added TTX (0.5 μM), CdCl₂ (300 μM) and NiCl₂ (500 μM) to block Na⁺ and Ca²⁺ channels, respectively. 20 μM bicuculline and 10 μM CNQX in the bath solution were included to block the synaptic inputs. After recording the total outward K⁺ current, I changed the bath solution which contained 3 mM TEA (Tetrathylammonium chloride). 3 mM TEA blocked slow inactivated K⁺ currents. The difference between the control and 3 mM TEA called TEA-sensitive currents (I_{TEA}). To isolate the A-type K⁺ current, the bath solution was changed to contain 5 mM 4-AP (4-

Aminopyridine) to block the A-type K^+ channel. The difference between the 3 mM TEA and 5 mM 4-AP called 5 mM 4-AP-sensitive currents (I_{4-AP}). To isolate the D-type K^+ current, the bath solution was changed to contain 40 μ M 4-AP to block the D-type K^+ channel. The difference between the 3 mM TEA and 40 μ M 4-AP called D-type K^+ currents (I_D). To obtain the activation curve, value of conductance were calculated from the respective peak currents and reversal potential of -95 mV. Activation curve was fitted with functions based on the Boltzmann equation.

4. Immunohistochemistry

Control (C57BL/6) and CBKO mice were sacrificed at 2 months of age. Mice were anesthetized with isoflurane and perfused transcardially with a freshly prepared solution of 1X phosphate buffered saline (PBS) and 4% paraformaldehyde (PFA) for 10 – 15 min. After mice were decapitated, brains were dissected from the skull. Serial 40- μ m-thick transverse tissue sections were cut using a vibratome (VT1200S, Leica, Germany), and fixed overnight at 4 °C by submersion in 4% PFA. After washing several times in 1X PBS with 0.3% Triton X-100

(PBS-T) for 5 min, sections were incubated in blocking solution (2.5% donkey serum + 2.5% goat serum in 0.3% PBS-T) for 3 hr at room temperature (RT). Blocking solution was changed every 1 hr. Next, sections were incubated overnight in primary antibodies diluted in blocking solutions at 4 °C.

- rabbit anti-Kv4.1 antibody (1:200; APC-119, Alomone lab)
- rabbit anti-Kv4.2 antibody (1:800; APC-023, Alomone lab)
- mouse anti-microtubule-associated protein 2 (MAP-2) antibody (1:400; M9942, Sigma)
- goat anti-doublecortin (DCX) antibody (1:100; C-18, Santa cruz biothechnology)

After washing 5 times in 0.3% PBS-T for 5 min, sections were incubated with goat anti-rabbit Cy5 antibody (1:300; ab97077, Abcam), donkey anti-rabbit-Alexa488 (1:100; A21206, Invitrogen), donkey anti-goat Alexa633 (1:400; A21082, Invitrogen) and donkey anti-mouse Fluorescein(FITC) antibody (1:50; 715-095-150, Jackson ImmunoResearch) diluted in blocking solution for 1 hr at RT. Sections were washed 5 times in 0.3% PBS-T for 5 min, and mounted with

fluorescent mounting medium (DakoCytomation, Cambridge,UK). In Figure 15, nuclear staining by DAPI was performed to visualize cells. Before mounting, tissues were incubated with DAPI in PBS (1:1000; Sigma–Aldrich) for 5 min and washed with PBS, and then mounted. The immunostained sections were imaged with a confocal laser scanning microscope (FV300, Olympus, Japan) using a 40X oil–immersion objective or 60X water–immersion objective, and then processed using Flouview (Olympus, Japan).

5. HEK 293T cell transfection

HEK 293T cell were cultured in Dulbecco’ s modified Eagle’ s medium (DMEM) supplemented with 10% (v/v) FBS and 1% (v/v) penicillin/streptomycin in a humidified incubator supplied with 5% CO₂ at 37 ° C. HEK 293T cells were plated in a 12–well plate at a density of 1×10^5 or 0.5×10^5 cells per well for electrophysiology, and transfected with EGFP–tagged Kv4.1 or Kv4.2 cDNA (0.4 µg/µl) using Lipofectamine 2000 (Life Technologies) at a ratio of 1:6 (DNA/lipid). Transfected HEK 293T cells were maintained in an incubator at 5% CO₂ for 24–36h at 37 ° C. Kv4.1 (Cat# MG220056) and Kv4.2 (Cat#

MG209597) DNA were purchased from OriGene (Rockville, MD, USA).

6. K⁺ current measurement in HEK293T cells

HEK 293T cells stably expressing Kv4.1 or Kv4.2 1–2 days after transfection were used for experiments. Transfected HEK 293T cells were transferred to a recording chamber and perfused at 1 ml/min with bath solution (or normal Tyrode' s solution) containing (in mM, 300 ± 10 mOsm): 143 NaCl, 5.4 KCl, 5 HEPES, 1.8 CaCl₂, 0.5 MgCl₂, 5 glucose with pH adjusted to 7.4 with NaOH. K⁺ currents were recorded by whole-cell patch clamp using a pipette solution of the following composition (in mM, 300 ± 10 mOsm): 110 K-aspartate, 30 KCl, 10 HEPES, 5 MgATP, 1 MgCl₂, with the pH adjusted to 7.2 with KOH. Experiments were performed at room temperature (RT). For antibody-blocking experiments, patch pipettes were dipped into an internal solution and then back-filled with the internal solution containing the antibody of Kv4.1 or Kv4.2 at a concentration of 6 µg/ml. To measure K⁺ currents, I applied a 0.5 s depolarizing voltage of +40 mV from a holding potential of -80 mV. Patch pipettes had resistances of 3–4 MΩ. The R_s

after establishing whole-cell configuration was between 5 and 11 M Ω . Signals were sampled at 1 kHz. Voltage-clamp acquisition was performed using an EPC-10 amplifier and PULSE software (version 8.67; HEKA, Lambrecht, Germany).

7. Open field exploration behavior test

Open field exploration test was used to assess locomotor activity (Kim et al., 2012). Open field exploration was performed with male mice 16 weeks of age (6 control mice and 6 CBKO mice). Mice were handled before open field exploration behavior test (OFT). Mice were picked up by the tail and held and without restraint in the palm of the hand for 15 min/day for 4 days. Following a handling, they were placed in a holding cage until all mice were handled. They were then returned to their home cage. During the mice handling, handlers wore latex gloves and changed the glove between the mice. After handling day, I am executed OFT test. I modified the protocol of Kim et al (2012) to conduct the OFT test (Kim et al., 2012). The Open field box was made of white plastic (40 * 40 * 40 cm) under diffuse lighting and white noise and the open field was divided into a center zone (center, 20 * 20 cm) and an outer field.

Individual mice were placed in the center zone and the path the animal were recorded with a video camera. During a 20 min observation period, the total distance traveled for 20 min and time spent in the center zone for initial 5 min were analyzed using the program EthoVision XT (Noldus, Virginia, USA)

8. Contextual fear discrimination test

Fear conditioning was performed with male mice between 15 and 16 weeks of age (10 control mice and 8 CBKO mice). I modified the protocol of McHugh et al (2007) to conduct the contextual fear discrimination task (McHugh et al., 2007). Mice were trained to discriminate between two similar contexts, A and B, through repeated experience in each context. Context A (conditioning context) is a chamber (18 * 18 * 30 cm; H10-11M-TC; Coulbourn Instruments 5583, PA 18052, USA) consisting of a metal grid floor, aluminium side walls, and a clear Plexiglass front door and back wall. Context A was indirectly illuminated with a 12 W light bulb. The features of Context B (safe context) were the same as Context A, except for a unique scent (1% acetic acid), dimmer light (50% of A), and a sloped floor by 15° angle. Each context was cleaned with

70% ethanol before the animals were placed. On the first 3 days (contextual fear acquisition), the mice were placed in Context A for 3 min for exploring the environment, and then received a single foot shock (0.75 mA, for 2 s). The mice were returned to their home cage 1 min after the shock. On day 4 – 5, mice of each genotype were divided into two groups; one group visited Context A on Day 4 and Context B on Day 5, while the other group visited the Context B on Day 4 and Context A on Day 5. On day 4 – 5 (generalization), neither group received a shock in Context A and B, and freezing level was measured for 5 min only in Context A. I defined freezing behavior as behavioral immobility except for respiration movement (McNaughton and Nadel, 1990). I observed video image for 2 s bouts every 10 s (18 or 30 observation bouts for 3 min or 5 min recording time) and counted the number of 2 s bouts during which the mouse displayed freezing behavior (referred to as a freezing score). The percentage of freezing was calculated by dividing the freezing score with the total number of observation bouts (18 or 30). The mice were subsequently trained to discriminate these two contexts by visiting the two contexts daily for 8 days (from day 6 to 13, discrimination task). The mice always

received a footshock 3 min after being placed in Context A but not B (Fig. 7C). Discrimination ratios were calculated according to $F_A / (F_A + F_B)$, where F_A and F_B are freezing scores in Contexts A and B, respectively. All experiments and analyses were performed blind to the mice genotype.

9. One trial contextual fear conditioning

Experiment was performed with male mice between 14 and 19 weeks of age (8 control mice and 8 CBKO mice) in a pair of very distinct contexts (A and C). The aforementioned Context A was used as the conditioning context. The distinct context (Context C) is a white acrylic blind end cylinder (15 cm in diameter, 18 cm in height, and 0.5 cm in thickness) standing vertically on the metal grid floor of Context A, and the bottom inside the cylinder was covered with cage bedding, on which mice were placed. The chamber and cylinder were cleaned using 70% ethanol between runs. On day 1 (acclimation), mice were placed in Context A and then placed them in Context C an hour later. Mice were allowed to freely explore in both contexts for 5 min. On day 2 (conditioning), all group of mice were place in Context A and receive a single foot shock (0.75 mA, for 2 s)

3 min later. Mice were left in the Context A for 1 min after the shock. On day 3 (assessment), mice were separated into two groups; mice of each group were placed in Context A or C for 3 min without a foot shock, during which the freezing score was measured. All experiments were conducted and analyzed by scientists blind to the genotypes of the mice.

10. Data analysis

Data were analyzed with Igor Pro (Version 6; Wavemetrics, Lake Oswego, USA) and are presented as the mean \pm SEM with the number of cells or mice (n) used in each experiment. Membrane potentials are given without correction for liquid junction potentials. The statistical significances were evaluated using Student's t-test, and the level of significance was indicated by the number of marks (*, $P < 0.05$; **, $P < 0.01$; ***, $P < 0.001$). $P > 0.05$ was regarded as not significantly different (N.S.).

Data from behavioral studies were analyzed using Igor Pro and Origin (Version 8; Microcal, Northampton, USA). Comparison between multifactorial statistical data was made using two-way analysis of variance (ANOVA). The differences

in time-dependent changes of behavioral parameters between the two genotypes were evaluated using two-way repeated measures ANOVA.

RESULTS

Differential expression patterns of Kv4 subunits in hippocampus region

Among Kv4 family channels that mediate A-type K^+ currents (I_A), Kv4.2 subunit is known to be highly expressed in principal neurons throughout the hippocampus and play crucial roles for regulating intrinsic excitability and synaptic plasticity (Chen et al., 2006; Kim et al., 2007; Kim et al., 2005). However, little is known for distribution and function of Kv4.1 subunit. I investigated the distribution of the Kv4.1 subunit in comparison with Kv4.2 subunit in different regions of the hippocampus using confocal microscopy immunofluorescence analysis with anti-Kv4.1 and Kv4.2 antibodies. Confocal images showed that both Kv4.1 and Kv4.2 subunits were well expressed throughout the hippocampus, but there were a number of differences in the regional and subcellular localization between Kv4.1 and Kv4.2 (Figs. 1A and 1B). At low magnifications, it is clear that the distribution pattern of Kv4.1 is opposite to that of Kv4.2. Kv4.1 signals were localized in the cellular layer of the hippocampus,

with little signals in the dendritic region (Fig. 1A), whereas Kv4.2 signals were absent in the cellular layer, but highly expressed in dendritic regions and in the stratum oriens of CA1 region (Fig. 1B). To quantify differential expression patterns of Kv4.1 and Kv4.2 subunits, I draw regions of interests in the stratum pyramidale and the stratum radiatum of CA1, and granule cell layer and molecular layer of dentate gyrus (DG), and obtained average intensities for Kv4.1 and Kv4.2 in each region (Fig. 1C). In addition to distinct subcellular distribution, a regional difference in Kv4.1 expression was also noted; strong Kv4.1 immunolabelling was present in the dentate gyrus granule cells (DG-GCs), but there was weak fluorescence in CA1 pyramidal cells (CA1-PCs) (Fig. 1A). To further confirm differential expression patterns of Kv4.1 and Kv4.2 subunits, I performed Western blot analyses. Expression level of Kv4.1 proteins was significantly lower in CA1 (Fig. 1D). In contrast, Kv4.2 expression showed a similar level between CA1 and DG (Fig. 1D).

Functional expression of Kv4.1-mediated currents ($I_{Kv4.1}$)

is specific for mature DG–GCs

Kv4.1 currents studied in heterologous expression systems show similar electrophysiological characteristics with Kv4.2 or Kv4.3 currents (Nakamura et al., 2001), but functional significance of endogenous Kv4.1 currents in native neurons are poorly understood. To investigate whether high expression of Kv4.1 subunits in the hippocampus have functional significance, I examined the effects of immunological blockade of Kv4.1 channels using anti-Kv4.1 antibody-containing pipette solutions. Although immunological blockade using specific antibodies were used for investigating the role of various K⁺ channels including Kv4.2 and Kv4.3 (Sanchez et al., 2002), anti-Kv4.1 antibody has not been used for this purpose. So, I first examined whether anti-Kv4.1 antibody introduced to the patch pipettes functionally inhibited Kv4.1 currents using HEK 239T cells where Kv4.1 or Kv4.2 DNA was heterologously expressed. I found that anti-Kv4.1 antibody inhibited Kv4.1 currents, but did not affect Kv4.2 currents (Fig. 2), confirming the selectivity of anti-Kv4.1 antibody.

I then monitored the changes in outward K⁺ currents

during intracellular dialysis of DG-GCs or CA1-PCs with the anti-Kv4.1 antibody (0.3 $\mu\text{g/ml}$). Whole-cell K^+ currents were recorded in voltage-clamp mode by applying a depolarizing voltage step from a holding potential of -70 mV to $+30$ mV (1 s duration), while tetrodotoxin (TTX), $\text{Cd}^{2+}/\text{Ni}^{2+}$, bicuculline, and CNQX were added to the external solution to block Na^+ channels, Ca^{2+} channels, GABA_A receptors, and AMPA/kainate receptors, respectively. Current amplitudes measured at their peak (I_{peak}) and those at the end of depolarizing pulses (I_{sus}) were plotted against the time duration after patch break-in (Figs. 3A-E). In DG-GCs, both I_{peak} and I_{sus} decreased gradually, reaching a steady state within 10 – 15 min (Fig. 3A). Inhibition of total outward currents by anti-Kv4.1 antibody was $36.35 \pm 5.05\%$ and $19.27 \pm 4.06\%$ for I_{peak} and I_{sus} current, respectively ($n = 4$, Figs. 3A and 3F). On the contrary, anti-Kv4.1 antibody induced only a small decrease in I_{peak} ($7.42 \pm 1.86\%$, $n = 8$, Fig. 3B and 3F) without a significant change in I_{sus} in CA1-PCs. I confirmed that a similar degree of small decreases in I_{peak} was also observed in CA1-PCs, while cells are dialyzed with normal internal solutions without anti-Kv4.1 antibody ($6.89 \pm 0.86\%$, $n = 5$, Figs. 3D and 3F). I found that

perfusion of DG-GCs with normal internal solutions also induced small decreases in K^+ currents ($9.47 \pm 0.84\%$ for I_{peak} and $3.70 \pm 1.39\%$ for I_{sus} , $n = 4$, Figs. 3C and 3F). These data suggests a preferential effect of anti-Kv4.1 antibody on outward K^+ currents in DG-GCs is compatible with a preferential expression of Kv4.1 subunits in DG-GCs.

Kv4.1 expression is developmentally regulated during maturation of DG-GCs

In a high power image for Kv4.1 immunoreactivity in DG area of 8 weeks old mice, it is noted that there is a gradient in fluorescence intensity along the axis from deep to superficial layer with cells located at hilar border showing lower expression (Fig. 4Aa). Considering that newly generated DG-GCs are located in the deep layer and migrate to the superficial layer as they mature, this finding may suggest a possibility that the Kv4.1 expression is developmentally regulated and increases with maturation of DG-GCs. To test this possibility, I examined Kv4.1 expression in DG area in young mice (3-week-old, Fig. 4B), and found that fluorescent intensity for

Kv4.1 is much weaker compared to that in adult mice (8-week-old, Fig. 4A). To further confirm the maturation-dependent change in Kv4.1 expression, newly generated neurons were identified with the doublecortin (DCX) antibody, and examined expression of Kv4.1 subunit in DCX-positive (DCX⁺) cells. Confocal images showed that Kv4.1 signals were hardly identified in DCX⁺ cells located in deep layer both in 8-week-old and 3-week-old mice (Figs. 4Ab and 4Bb). Kv4.1 signals in superficial layer are stronger both in young and adult mice, but it is noted that the signals in young mouse are weaker than those in adult mouse, suggesting that 3 week is not enough for full expression of Kv4.1. To examine whether the maturation dependent changes in Kv4.1 expression are consistent with Kv4.1-mediated currents ($I_{Kv4.1}$), I tested effects of anti-Kv4.1 antibody on outward K⁺ currents in immature DG-GCs. Since a close correlation between the age of new-born DG-CGs and the decrease in input resistance (R_{in}) was well described (Dieni et al., 2013), I distinguished immature from mature DG-GCs according to R_{in} . Hyperpolarization of resting membrane potential (RMP) is another characteristic of maturation (Mongiati et al., 2009). I

confirmed that changes in RMP have a strong correlation with changes in R_{in} , reaching maximum negative RMP when R_{in} became lower than 200 M Ω (Fig. 5A). The mean value for R_{in} for mature DG-GCs used in the present study was 155.4 ± 6.04 (n = 25, Fig. 5B). I typically selected cells with R_{in} between 300 M Ω and 800 M Ω as immature DG-GCs (456.4 ± 34.7 , n = 18). According to the previous studies (Dieni et al., 2013; Mongiat et al., 2009), the R_{in} value used in the present study corresponds to that of adult-born neurons at age of 4 weeks to 6 weeks. In hippocampal slices obtained from adult mice aged older than 8 weeks, immature DG-GCs were usually found in deep layer. In these immature DG-GCs, outward K^+ currents showed little responses upon exposure to anti-Kv4.1 antibody (Fig. 4Ca, left). In hippocampal slices obtained from young mice aged less than 3 weeks, most DG-GCs have R_{in} larger than 300 M Ω , of which outward K^+ currents also exhibited little responses when anti-Kv4.1 antibody was applied (Fig. 4Ca, right). Figure 4Cb summarizes the effects of Kv4.1 antibody on outward K^+ currents in immature and mature DG-GCs, suggesting that Kv4.1 currents are functionally active only in fully mature DG-GCs.

Kv4.1 selectively regulate the firing frequency of mature DG-GCs

To investigate functional significance of selective expression of $I_{Kv4.1}$ in mature DG-GCs, I first compared intrinsic excitability between mature and immature DG-GCs. In spite of huge differences in R_{in} and RMP between mature and immature DG-GCs, there was no significant difference in threshold potential or overshoot or halfwidth of APs (Figs. 5D – 5F), suggesting that Na^+ channel density or properties may not be different between mature and immature DG-GCs. In contrast, there was a significant difference in the firing frequency of repetitive APs during a sustained depolarization between mature and immature DG-GCs (left and middle, Fig. 6Aa). Firing frequency of mature DG-GCs was much lower than that of immature DG-GCs, and this difference was not abolished when RMP of mature DG-GCs was depolarized by current injection to the level of immature DG-GCs (right, Fig. 6Aa). These results are summarized in F-I curve where firing frequency (F) is plotted against the intensity of injected current (I) (Fig. 6Ab), suggesting the

existence of unique ion channel mechanism for low frequency firing in mature DG-GCs.

Since I found preferential expression of Kv4.1 in mature DG-GCs, I hypothesized that Kv4.1 current may serve as outward K^+ currents that suppress repetitive firing in mature DG-GCs. In consistent with this idea, the firing frequency of repetitive APs in mature DG-GCs increased gradually with perfusion of anti-Kv4.1 antibody (closed circles, Fig. 6Ba), and this increase was associated with a decrease in 1st AP onset time (open circles, Fig. 6Ba). By contrast, passive electrical properties, such as R_{in} , and RMP, remained unchanged (Fig. 6D). Comparison of F-I curve obtained in control and that in the presence of anti-Kv4.1 antibody showed that firing frequency was increased significantly by Kv4.1 channel blockade over the whole range of stimulus intensities tested (Fig. 6Bb). To test whether such effect is specific to Kv4.1, I performed the same series of experiments using anti-Kv4.2 antibody. The specificity of anti-Kv4.2 antibody for inhibiting Kv4.2 current was confirmed in HEK 293T cells overexpressing Kv4.1 or Kv4.2 subunits (Figs. 2Ab and 2Bb). Perfusion of the anti-Kv4.2 antibody to mature DG-GCs did not significantly affect

the firing frequency or AP onset time (Fig. 7A – 7B). However, frequency-dependent AP broadening was significantly enhanced after anti-Kv4.2 antibody perfusion (Figs. 7Ac and 7B), which is consistent with the effect of Kv4.2 blockade reported in CA1-PCs (Kim et al., 2005). These results suggest that the Kv4.1 and Kv4.2 currents play distinctive roles in the regulation of intrinsic excitability. In particular, Kv4.1 is a selective regulator of firing frequency in mature DG-GCs. I also performed the same series of experiments in immature DG-GCs where Kv4.1 expression is low and anti-Kv4.1 antibody does not affect outward K^+ currents, and confirmed that any parameters for intrinsic excitability were not affected by anti-Kv4.1 antibody in immature DG-GCs (Figs. 6C and 6D). These results are consistent with little expression and activity of Kv4.1 channels in immature DG-GCs (Fig. 4).

Differences in outward K^+ currents between mature and immature DG-GCs

Sparse firing of DG-GCs is important for pattern separation (Jinde et al., 2012). To investigate whether other voltage-

dependent K^+ currents contribute to the differences in firing frequency between mature and immature DG-GCs, I analyzed difference in outward K^+ currents between two cell types. Whole-cell K^+ currents were recorded in voltage-clamp mode by applying a depolarizing voltage step from a holding potential of -70 mV to a membrane potential between -60 mV and $+50$ mV ($+10$ mV increments, 1 s duration). Using TEA and 4-AP, which are more selective to block delayed rectifier K^+ currents and A-type K^+ currents, respectively (Johnston et al., 2010), K^+ currents were dissected into TEA-sensitive K^+ current (I_{TEA}) and 4-AP-sensitive K^+ current (I_{4-AP}) (Fig. 8). The amplitude of I_{TEA} was larger in mature compared to immature DG-GCs (Figs. 9Aa and 9Ab), but there was no significant difference when the amplitude was normalized to the cell capacitance (25.63 ± 0.75 pF in mature; 15.45 ± 1.52 pF in immature), indicating that the density of I_{TEA} is not significantly changed with maturation (Fig. 9B).

In contrast, the amplitude of I_{4-AP} was much larger in mature compared to immature DG-GCs (Figs. 9Ca and 9Cb), and the difference was still significant when the amplitude was normalized to the cell capacitance (Fig. 9D). Furthermore, there

is a distinctive feature in I_{4-AP} between mature and immature DG-GCs (Fig. 9Ca). I_{4-AP} recorded in immature DG-GCs displayed rapid activation and inactivation kinetics (right, black, Fig. 9Ca), which are consistent with typical A-type K^+ currents (Birnbaum et al., 2004). By contrast, a considerable proportion of I_{4-AP} in mature DG-GCs was not inactivated even after 1 s (left, blue, Fig. 9Ca). The ratio of the amplitude of the I_{sus} to the I_{peak} measured at +30 mV was 0.237 ± 0.02 ($n = 12$) in mature DG-GCs. Selective expression of Kv4.1 currents in mature DG-GCs may underlie distinctive properties and higher density of I_{4AP} in mature DG-GCs.

Characterization of Kv4.1-mediated currents in DG-GCs

Kv4.1 currents studied in heterologous expression systems show similar electrophysiological characteristics with Kv4.2 or Kv4.3 currents (Nakamura et al., 2001). Since characteristics of endogenous Kv4.1 currents in native neurons have not been investigated, I characterized electrophysiological properties of $I_{Kv4.1}$. To obtain $I_{Kv4.1}$ from the difference currents obtained before and after cells were dialyzed with anti-Kv4.1 antibody

with little contamination of other current components, it is necessary to eliminate the current changes observed during perfusion of DG-GCs with control internal solutions (Fig. 3C). Since the control internal solutions contained 0.1 mM EGTA, I assumed that perfusion of the internal solution may induce a slight suppression of Ca^{2+} -activated K^+ currents. This possibility was supported by the observation that the decrease in outward K^+ currents after patch break-in was no longer observed when 3 mM TEA was included in the bath solution to block Ca^{2+} -activated K^+ currents (Figs. 3E and 3F). Therefore, I analyzed changes in outward K^+ currents during intracellular dialysis of DG-GCs with anti-Kv4.1 antibody in the presence of 3 mM TEA in the bath solution. Whole-cell K^+ current recorded 14 min later in the presence of the anti-Kv4.1 antibody in the internal solution (middle, Fig. 10Aa) was subtracted from the currents recorded immediately after patch break-in (left, Fig. 10Aa) to obtain $I_{\text{Kv4.1}}$ (right, Fig. 10Aa). $I_{\text{Kv4.1}}$ showed rapid voltage-dependent activation, but the inactivation kinetics were very slow so that a significant proportion of currents remained at the end of the 1 s depolarization ($I_{\text{sus}}/I_{\text{peak}} = 0.48 \pm 0.09$ at +30 mV, $n = 7$, Fig.

10D). These properties are strikingly different from typical A-type K^+ currents known to be encoded by Kv4.2.

I then obtained I_{4-AP} under the condition that $I_{Kv4.1}$ was completely inhibited by anti-Kv4.1 antibody (Fig. 10B). The results were typical A-type K^+ currents showing rapid voltage-dependent activation followed by rapid inactivation (right, blue, Fig. 10Ba). Therefore, I referred to these currents as transient outward currents, I_A . To demonstrate the difference between $I_{Kv4.1}$ and I_A more clearly, the mean current traces for $I_{Kv4.1}$ ($n = 7$) and I_A ($n = 10$) obtained at +30 mV from DG-GCs were superimposed (Fig. 10Ca). Time to peak was not significantly different (4.73 ± 0.76 ms for $I_{Kv4.1}$ and 5.31 ± 0.41 ms for I_A), but I_{peak} was significantly larger for I_A (1.5 ± 0.15 nA at +30 mV, $n = 10$) than $I_{Kv4.1}$ (0.70 ± 0.10 nA at +30 mV, $n = 7$). In contrast, I_{sus} was significantly larger for $I_{Kv4.1}$ (0.29 ± 0.04 nA at +30 mV, $n = 7$) than I_A (0.09 ± 0.03 nA at +30 mV, $n = 10$). Therefore, I obtained the ratio of I_{sus} to I_{peak} (I_{sus}/I_{peak}) to compare the difference in inactivation kinetics between $I_{Kv4.1}$ and I_A (Fig. 10D), showing that I_{sus}/I_{peak} for $I_{Kv4.1}$ was significantly larger than the ratio for I_A over the voltage range between -10 to +50 mV. Slow inactivation

kinetics of $I_{Kv4.1}$ and selective expression of $I_{Kv4.1}$ in mature DG-GCs explain distinctive feature of I_{4-AP} in mature DG-GCs shown in Figure 9. I_{4-AP} in mature DG-GCs is well explained by the sum of $I_{Kv4.1}$ and I_{to} . I also compared voltage-dependence of activation (Fig. 10E), and found that the voltage for half activation ($V_{1/2}$) for $I_{Kv4.1}$ was 7.6 ± 2.2 mV ($n = 5$), which was significantly more positive than the $V_{1/2}$ for I_A (-0.6 ± 2.6 mV, $n = 6$, $p < 0.05$).

$I_{Kv4.1}$ are distinctive from slowly inactivating D-type K^+ currents

D-type K^+ current (I_D), which is characterized by a rapidly activating but slowly inactivating outward K^+ currents, has been identified in CA1-PCs (Storm, 1988), CA3-PCs (Hyun et al., 2013; Luthi et al., 1996) and DG-GCs (Beck et al., 1997). I_D in central neurons is primarily mediated by Kv1.1 and Kv1.2 subunit, and known to be blocked by a low concentration of 4-AP (40 μ M, (Beck et al., 1997)). Since the inactivation kinetics of $I_{Kv4.1}$ in mature DG-GCs resembles that of I_D reported previously (Beck et al., 1997; Storm, 1988), it could be argued

that $I_{Kv4.1}$ is a component of I_D . Since I_D is blocked by a low concentration of 4-AP, I first characterized I_D in mature DG-GCs using 40 μ M 4-AP (Fig. 11Aa). Activation of I_D was apparent at -30 mV, and $V_{1/2}$ was -14.7 ± 2.9 mV ($n = 6$), which is significantly more negative than values for I_A or $I_{Kv4.1}$. These results confirm the presence of I_D as a low voltage-activated K^+ current in mature DG-GCs. Effects of blocking I_D using 40 μ M 4-AP on intrinsic excitability showed that AP onset time measured at 200 pA depolarization was decreased from 0.11 ± 0.01 to 0.09 ± 0.01 ms ($n = 8$, Fig. 11Bb), which is consistent with previous reports (Cudmore et al., 2010; Hyun et al., 2013). However, there was no change in RMP, R_{in} , and firing frequency (Fig. 11Bb), indicating that contribution of I_D to intrinsic excitability was very different from that of $I_{Kv4.1}$ in mature DG-GCs. To further investigate the distinction between I_D and $I_{Kv4.1}$, I examined the pharmacological properties of $I_{Kv4.1}$. I investigated the effect of anti-Kv4.1 antibody to inhibit outward K^+ currents in the presence of 40 μ M 4-AP in the bath solution where I_D was blocked. The effect of anti-Kv4.1 antibody to inhibit outward K^+ currents was unchanged in the presence of 40 μ M 4-AP in the bath solution where I_D was

blocked (Figs. 11C and 11D), indicating that $I_{Kv4.1}$ is not sensitive to 40 μ M 4-AP. In contrast, perfusion of anti-Kv4.1 antibody did not show significant inhibition on outward K^+ currents in the presence of 5 mM 4-AP in the bath solution (Figs. 11C and 11D), indicating that $I_{Kv4.1}$ is blocked by a high concentration of 4-AP. I also investigated the contribution of KCNQ/M channel in the excitability of mature DG-GCs. KCNQ/M are voltage dependent K^+ channels that partially open at the RMP. Inhibiting the KCNQ/M channel increases both R_{in} and neuronal excitability (Browne et al., 1994; Jentsch, 2000). Blocking the KCNQ channel using a specific blocker, XE991 (10 μ M), the firing frequency in DG-GCs significantly increased after application of XE991 (Fig. 12A). Moreover, application of XE991 increased R_{in} , decreased rheobase current and slightly depolarized RMP in DG-GCs (Fig. 12B). The change in firing frequency after application of XE991 was correlated with an increased R_{in} . These results indicate that although the slow inactivation kinetics of $I_{Kv4.1}$ resemble that of I_D , pharmacological characteristics of $I_{Kv4.1}$ are distinct from those of I_D and rather resemble A-type K^+ currents mediated by other Kv4 family channels.

Ca²⁺-sensitivity of DG excitability is attributable to Ca²⁺-sensitivity of I_{Kv4.1}

The slowly inactivating components of I_{4-AP} was described both in neurons and cardiac myocytes, and they were reported to be sensitive to intracellular Ca²⁺ (Hamon et al., 1995; Tessier et al., 1999). To investigate whether I_{Kv4.1} is Ca²⁺-dependent, I analyzed the effects of 10 mM BAPTA in the internal solution on I_{4-AP} in mature DG-GCs. I_{4-AP} in mature DG-GCs obtained in the presence of 10 mM BAPTA to chelate intracellular Ca²⁺ showed decreases in I_{sus} over a wide voltage range with no significant change in I_{peak} compared with those obtained in the presence of 0.1 mM EGTA (Figs. 13Aa and 13Ab). The amplitude of I_{sus} in the presence of BAPTA (0.15 ± 0.05 nA at +30 mV, n = 5, Fig. 13Ac) was similar to that obtained in the presence of anti-Kv4.1 antibody (0.09 ± 0.03 nA at +30 mV, n = 10, Fig. 10Cb), suggesting that I_{Kv4.1} are almost completely blocked by 10 mM BAPTA (Fig. 13A). To verify the functional significance of Ca²⁺-dependence of I_{sus}, I tested the effect of 10 mM BAPTA on the firing frequency of mature DG-GCs. The results showed that firing frequency in mature DG-GCs was

significantly increased by 10 mM BAPTA in the pipette solution (pink, Fig. 13B). Interestingly, an upward-shift of the F-I curve by BAPTA (Fig. 13Bb) is comparable to that by anti-Kv4.1 antibody. These results are consistent with the idea that slowly inactivating component of I_{4-AP} is a unique feature for $I_{Kv4.1}$ and that $I_{Kv4.1}$, which is responsible for limiting the firing frequency in mature DG-GCs, is sensitive to intracellular Ca^{2+} .

Characteristics of intrinsic excitability and I_{4-AP} of CA1 pyramidal cells

I showed that outward K^+ currents in CA1-PCs were not affected by anti-Kv4.1 antibody perfusion (Fig. 3B), suggesting the lack of $I_{Kv4.1}$. To understand how differential expression of $I_{Kv4.1}$ contributes to differences in electrical properties of CA1-PCs and DG-GCs, I first characterized outward K^+ currents in CA1-PCs and compared them with those of DG-GCs. I compared I_{TEA} , but there was no significant difference between CA1-PCs and DG-GCs (Fig. 14A; +30 mV; I_{peak} for CA1, 1.81 ± 0.21 , $n = 9$, I_{peak} for DG, 1.81 ± 0.15 nA, $n = 9$; $p > 0.1$; I_{sus} for CA1, 0.83 ± 1.23 nA, $n = 9$, I_{sus} for DG,

1.11 \pm 0.13 nA, n = 9). However, I_{4-AP} in CA1-PCs (Fig. 14B) displayed distinctive features compared to that of mature DG-GCs shown in Figure 9C. I_{4-AP} recorded in CA1-PCs displayed rapid activation and inactivation kinetics, and slowly inactivating component was not obvious. To directly compare the difference in I_{4-AP} between mature DG-GCs and CA1-PCs, mean current traces obtained at +30 mV in DG-GCs and CA1-PCs were overlaid (Fig. 14Ca, n = 12 for DG-GCs; n = 6 for CA1-PCs). The most apparent difference was the amplitude of I_{sus} without a noticeable difference in overall time course (Figs. 14Ca and 14Cb), and I_{sus}/I_{peak} ratio was significantly smaller in CA1-PCs (Fig. 14D). The midpoint potentials of half-maximum activation ($V_{1/2}$) for I_{4-AP} was slightly more negative in CA1-PCs (Fig. 14E; DG-GCs, 4.7 \pm 0.7 mV, n = 5; CA1-PC, -0.9 \pm 1.0 mV, n = 4; p < 0.05). Furthermore, I also performed the same series of experiments in CA1-PCs where Kv4.1 expression is low (Fig. 1) and anti-Kv4.1 antibody does not affect outward K^+ currents (Fig. 3), and confirmed that any parameters for intrinsic excitability were not affected by anti-Kv4.1 antibody in CA1-PCs (Fig. 14F). The properties of I_{4-AP} in CA1-PCs are consistent with the lack of $I_{Kv4.1}$ in CA1-PCs.

Downregulation of Kv4.1, reduced I_{sus} , and increased firing frequency in CBKO mice

The effects of BAPTA on $I_{\text{Kv4.1}}$ in mature DG-GCs suggest that Kv4.1 channels are regulated by intracellular Ca^{2+} concentrations. I therefore curious to know the effects of Ca^{2+} buffer deficits on $I_{\text{Kv4.1}}$. On the basis of the observation that calbindin- $\text{D}_{28\text{K}}$ (CB) is the major Ca^{2+} buffer in mature DG-GCs (Muller et al., 2005) and that Ca^{2+} overload often causes ion channel remodeling (Brundel et al., 2002; Ohashi et al., 2004), I used CB knockout (CBKO) mice to investigate this issue. When outward K^+ currents were dissected into I_{TEA} , I_{D} , and $I_{4\text{-AP}}$ by obtaining the difference in current between K^+ currents recorded in the absence and presence of the blockers (Fig. 16), it was readily noticeable that sustained component of $I_{4\text{-AP}}$, which is attributable to $I_{\text{Kv4.1}}$, was reduced in CBKO (Fig. 15Aa). I - V curves for $I_{4\text{-AP}}$ showed that both I_{peak} and I_{sus} were reduced in CBKO mice (Figs. 15Ab; $p < 0.05$, $n = 6$). The reduction of the $I_{\text{sus}}/I_{\text{peak}}$ in CBKO mice was similar to that observed in control mice in the presence of the anti-Kv4.1

antibody (Fig. 15B). I confirmed that I_{TEA} or I_D in DG-GCs of CBKO mice were not significantly different from those of control mice (Fig. 16; $p > 0.1$, $n = 5$). These findings suggest the selective suppression of $I_{Kv4.1}$ without changes in other K^+ currents in CBKO mice. Suppression of $I_{Kv4.1}$ may be attributable to the functional inhibition of Kv4.1 channels under the Ca^{2+} overload condition due to Ca^{2+} buffer deficits, but it may be unlikely that $I_{Kv4.1}$ is commonly inhibited by excess Ca^{2+} buffer as well as Ca^{2+} buffer deficits. I therefore tested whether Kv4.1 expression is altered in CBKO mice.

Confocal microscopy immunofluorescence analysis was performed in CBKO mice hippocampal slices with the same antibodies and the same fluorescence intensity used for control mouse. At low magnification, confocal microscopy image showed weak fluorescence of Kv4.1 subunit even in the DG area (upper, left panel, Fig. 15C). High magnification confocal microscopic images revealed that DG show low density of Kv4.1 in somato-dendritic region of DG-GCs (Fig. 15D, Kv4.1; GCL; Control, 20.29 ± 2.02 , $n = 10$, CBKO, 10.48 ± 0.41 , $n = 4$; $p < 0.01$). However, CA3- to CA1-PC did not show significant difference between control and CBKO mice. No significant change in the

expression of Kv4.2 subunit was observed in CBKO mice (Fig. 15C). I obtained the intensity of Kv4.1 and Kv4.2 subunits in control and CBKO mice. I examined the expression levels of transcripts for Kv4 family channels in the DG using quantitative real-time PCR (qRT-PCR) techniques, and confirmed that Kv4.1 mRNA expression was significantly reduced in the DG of CBKO mice, but that Kv4.2 and Kv4.3 mRNA expression were not different (Fig. 15E; Kv4.1, $p < 0.001$, $n = 16$; Kv4.2, $p > 0.5$, $n = 16$; Kv4.3, $p < 0.8$, $n = 8$). I also performed Western blot analyses. Expression level of Kv4.1 proteins was significantly lower in DG of CBKO mice (Fig. 15F; Kv4.1, $n = 6$, Control, 1.00 ± 0.1 , CBKO, 0.54 ± 0.15 ; $p < 0.05$). In contrast, Kv4.2 expression showed a similar level between control and CBKO mice (Fig. 15F; Kv4.2, $n = 4$, Control, 1.02 ± 0.03 , CBKO, 0.92 ± 0.03 ; $p > 0.06$).

Next, I examine the effect of reduced Kv4.1 channel expression on neuronal excitability. Fig 17A showed a significantly higher firing frequency in DG-GCs of CBKO mice compared to control mice (Fig. 17A; $p < 0.001$, $n = 8$). In parallel, the AP onset time was significantly shorter in DG-GCs of CBKO (Fig. 17Bb; $p < 0.01$, $n = 8$), although there were no

significant differences in other parameters, such as RMP, R_{in} , and rheobase, between control and CBKO mice (Figs. 17Bb and 17Cb). Moreover, the overshoot amplitude in CBKO were similar to control mice (Figs. 17Ca and 17Cb), suggesting that the properties of Na^+ channel activation are not different. By contrast, the firing frequency in CA1-PCs was not significantly different between control and CBKO mice (Fig. 18A; $p > 0.4$, control, $n = 10$, CBKO, $n = 5$). These findings in CBKO mice are markedly similar to the effects of the anti-Kv4.1 antibody in control mice, supporting the idea that reduced expression of Kv4.1 channels is responsible for the changes in intrinsic excitability of DG-GCs in CBKO mice. This idea was further confirmed by testing the effect of anti-Kv4.1 antibody perfusion on firing frequency of DG-GCs in CBKO mice (Fig. 17Da). Unlike control mice, firing frequency was not affected by anti-Kv4.1 antibody perfusion in CBKO DG-GCs (Fig. 17Db).

Impaired pattern separation in CBKO mice

Knockout technology is widely used to investigate the role of a

specific ion channel in vivo, but it is not always successful due to compensatory increases in other ion channels that have similar functions. In fact, Kv4.2 knockout mice show modest changes in intrinsic excitability compared to those observed with acute attenuation or elimination of I_A with pharmacological blockers or dominant negative strategies as a result of compensatory increases in delayed rectifier K^+ currents (Nerbonne et al., 2008). Since CBKO show selective abolishment of $I_{Kv4.1}$ in mature DG-GCs, I used CBKO mice to investigate the impact of Kv4.1 downregulation and DG-GCs hyperexcitability. The low excitability of the DG is thought to be important for pattern separation in the hippocampus (O'Reilly and McClelland, 1994). I investigated whether increased firing of mature DG-GCs in CBKO mice leads to impairments in discriminating similar contexts by using a contextual fear discrimination test. I first subjected the CBKO mice to contextual fear conditioning using a similar pair of contexts (A and B) that shared an identical metal grid floor, although context B had unique an odor (1% acetic acid), dimmer lighting (50% of A), and a sloped floor (15° angle). As shown in Figure 20A, mice learned to discriminate between the similar

contexts over several days. During the first 3 days, mice were placed only in context A, receiving a single foot shock after 180 s. On day 4 and 5, mice of each genotype were divided into two groups. One group visited context A on day 4 and context B on day 5, and the other group visited context B on day 4 and context A on day 5; no group received a foot shock in either context, and freezing was evaluated for 5 min. Both genotypes showed similar freezing levels during the 5 min test in context A (Fig. 20Ba) and equivalent generalization between contexts (Fig. 20Bb, two-way ANOVA, genotype: $F_{(1,32)} = 0.30$, $p = 0.58$, context: $F_{(1,32)} = 1.17$, $p = 0.29$, genotype \times context: $F_{(1,32)} = 0.03$, $p = 0.86$). The mice were subsequently trained to disambiguate these contexts by visiting both contexts daily for 8 days with a 2 hr interval between contexts (from day 6 to day 13), always receiving a foot shock 180 s after being placed in context A but not in context B. A daily discrimination ratio was calculated by determining the ratio of freezing during the 180 s in context A to total freezing during the two visits (A and B). On day 6, both genotypes could not distinguish differences between the contexts (Fig. 20Cb, genotype: $F_{(1,32)} = 0.005$, $p = 0.94$, context: $F_{(1,32)} = 0.001$, $p = 0.97$, genotype \times context:

$F_{(1,32)} = 0.32$, $p = 0.57$); thus, the discrimination ratio was approximately 0.5. As the experiment progressed, control mice began to discriminate context B from context A, and the discrimination ratio was increased. However, CBKO mice exhibited significant deficits in the acquisition of discrimination ability (Fig. 20Ca), and showed increased freezing in the shock-free context (Fig. 20Cb, t-test, Context B, $p < 0.0001$, Two-way ANOVA, genotype: $F_{(1,32)} = 6.71$, $p = 0.01$, context: $F_{(1,32)} = 52.99$, $p < 0.0001$, genotype \times context: $F_{(1,32)} = 25.60$, $p < 0.0001$). To examine whether impaired discrimination between similar contexts in CBKO mice was due to impaired general memory acquisition, I examined the context specificity of the conditioning by assessing freezing behavior using a distinct pair of contexts (A and C). This distinct context (context C) evoked significantly lower levels of freezing (similar in both genotypes) than context A (Fig. 20D, genotype: $F_{(1,11)} = 0.002$, $p = 0.96$, context: $F_{(1,11)} = 30.34$, $p < 0.0001$, genotype \times context: $F_{(1,11)} = 0.002$, $p = 0.96$). These data imply CBKO mice experienced no deficits in learning or discriminating between very distinct contexts, but showed impairments with similar contexts (pattern separation). CBKO

mice did not exhibit detectable abnormalities in anxiety and locomotor activity (Fig. 19). These results indicate that CBKO mice exhibited specific impairment in pattern separation between similar contexts without deficits in memory acquisition.

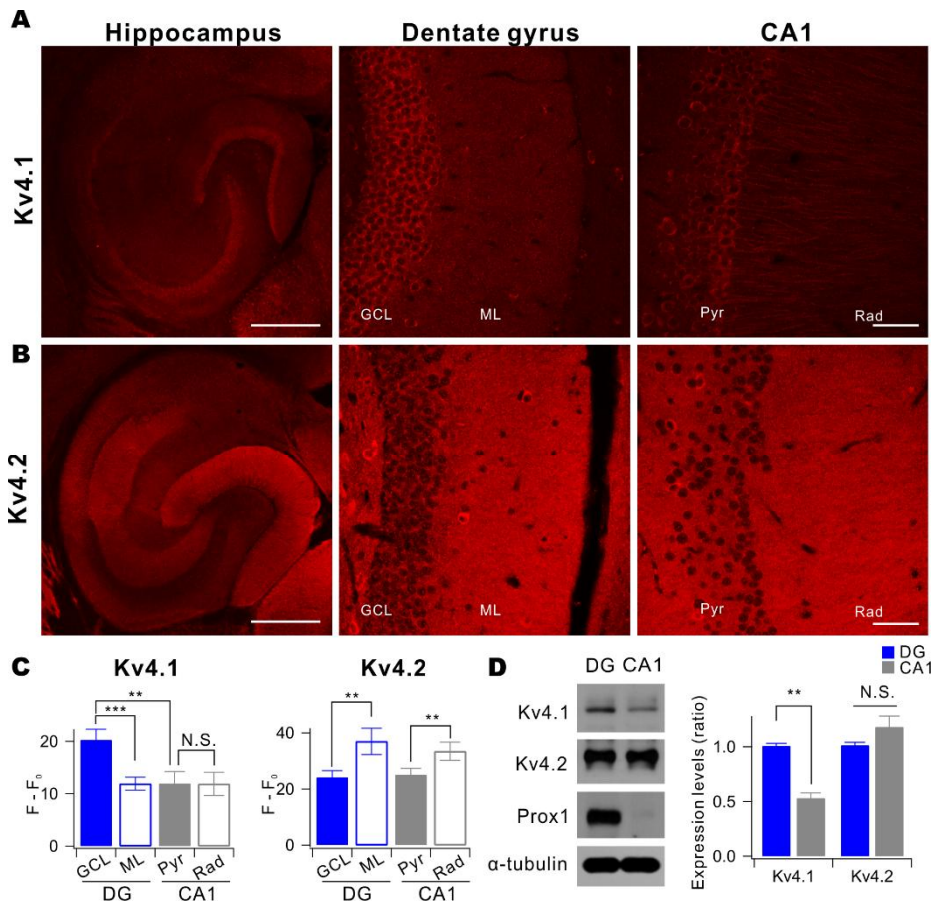


Figure 1. Immunofluorescent localization of the Kv4.1 and Kv4.2 subunit in hippocampus region

Immunohistochemical localization of Kv4.1 (A) and Kv4.2 subunits (B) in the hippocampus area of 2-month-old mice immunostained with antibodies against Kv4.1 and Kv4.2 subunits. (A–B) Left, 5x magnification view of the hippocampus are labelled for Kv4.1 (A) or Kv4.2 (B). Left white scale bars represent 500 μ m. Middle to right panel, 40x magnification view

of the dentate gyrus (middle) and CA1 region (right) in Kv4.1 (A) or Kv4.2 (B) antibody. Middle to right panel scale bar represent 50 μm . (C) Summary bar graph of F-F₀ shown in 5X magnification view of DG(blue) and CA1(gray) for Kv4.1 (n = 10) or Kv4.2 (n = 5). GCL, granule cell layer; ML, molecular layer; Pyr, pyramidal layer; Rad, striatum radiatum. (D) Acute hippocampal slices were isolated from DG (blue) and CA1 (gray) of C57BL/6 (control) mice, and solubilized as described in Material and Method. The endogenous protein expression levels were analyzed by Western blotting with the indicated antibodies. Prox1 expression defines DG neurons. Bar graph data represent the means of Kv4.1 or Kv4.2 expression \pm SEM (Kv4.1 in DG, 1.00 \pm 0.02; Kv4.1 in CA1, 0.53 \pm 0.05; Kv4.2 in DG, 1.00 \pm 0.02; Kv4.2 in CA1, 0.17 \pm 0.10; n = 8; p < 0.001, paired *t-test*). Values indicate mean \pm SEM. Error bars indicates SEM.

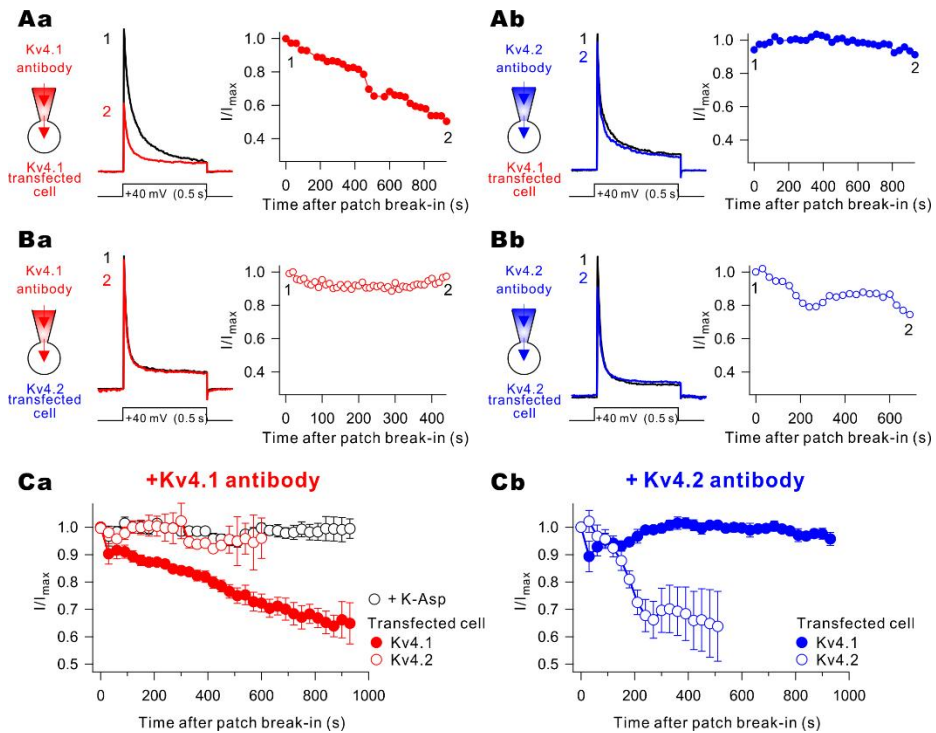


Figure 2. Inhibition of total K⁺ current in Kv4.1-expressing HEK 293T cells using anti-Kv4.1 or anti-Kv4.2 antibody

(A–B) Left, representative trace of total K⁺ current activated by 0.5 s voltage pulse from +40 mV from a holding potential of -80 mV were superimposed. Total K⁺ current in Kv4.1 (A) or Kv4.2 (B)-expressing HEK 293T cell measured after patch break in (1, black) or during an intracellular application of the anti-Kv4.1 antibody (2, red, a) or anti-Kv4.2 antibody (2, blue, b). Right, time course of anti-Kv4.1 (a, red) or anti-Kv4.2 (b, blue) antibody effects on normalized peak current (I/I_{max})

evoked by 0.5 s pulse to +40 mV in Kv4.1 (A) or Kv4.2 (B)–
expressing HEK 293T cells. (C) Summary graph of inhibition of
 I/I_{\max} by anti-Kv4.1 (red, Ca), or anti-Kv4.2 (blue, Cb)
antibody, or K-Asp internal (black, Ca). Values indicate mean
 \pm SEM. Error bars indicates SEM.

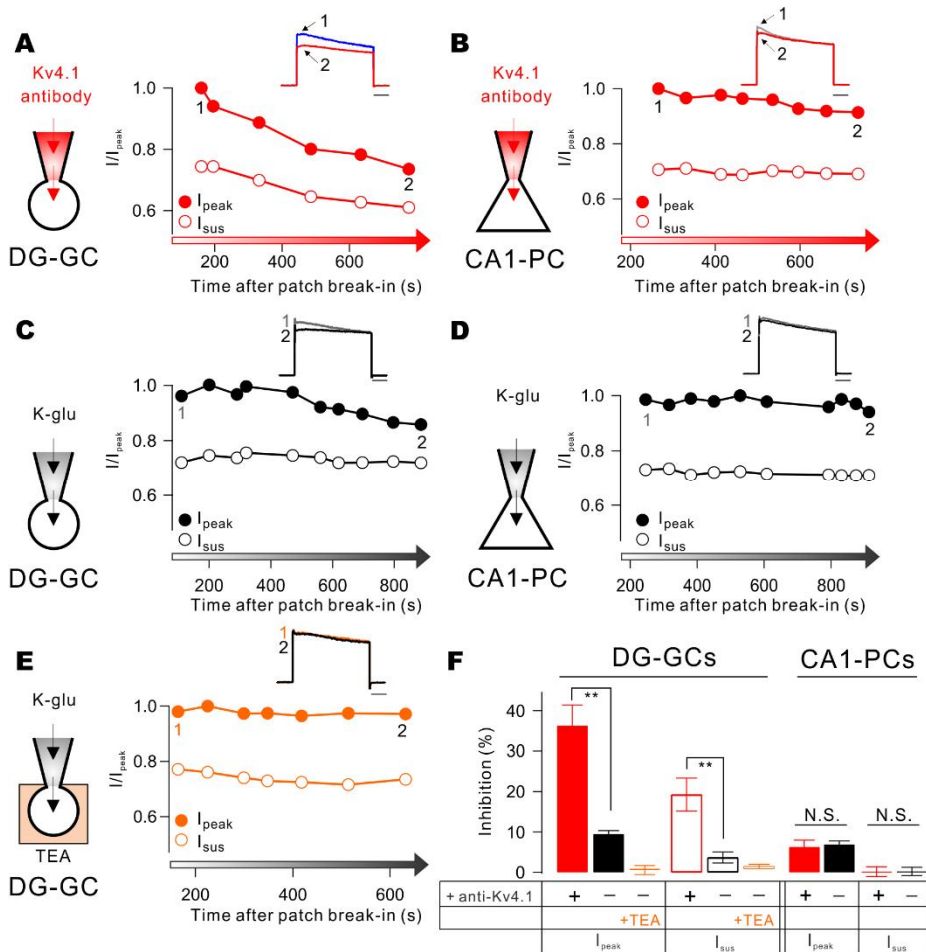


Figure 3. Inhibition of total outward K^+ current in hippocampal cell types using anti-Kv4.1 antibody

(A–B) Time course of anti-Kv4.1 antibody (red) effects (Scheme) on K^+ current evoked by 1 s pulse to +30 mV in DG (A) and CA1 (B). (C–D) Time course of K-gluconate internal effects on K^+ current in DG (C) and CA1 (D) evoked by 1 s pulse to +30 mV. (E) Time course of K-gluconate internal

effects on K^+ current in DG-GCs in presence of 3 mM TEA (orange) evoked by 1 s pulse to +30 mV. (A-E) Inset trace, example of normalized K^+ currents during intracellular dialysis with anti-Kv4.1 antibody or K-gluconate. Total K^+ current in hippocampal cell types measured after patch break in (1) or during an intracellular application or 3 mM TEA application (2). (F) Summary bar graph of inhibition of I_{peak} and I_{sus} by intracellular solution or bath application of 3 mM TEA. Values indicate mean \pm SEM. Error bars indicates SEM.

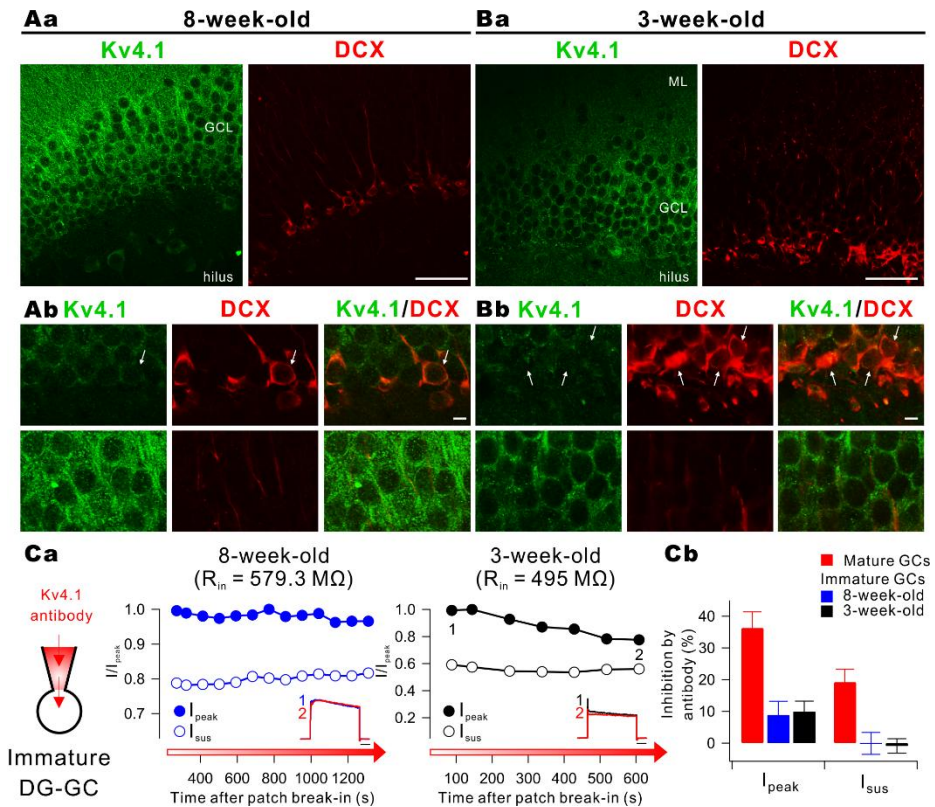


Figure 4. Expression of Kv4.1 channel during the maturation of DG-GCs

40x magnification view of the DG are labelled for Kv4.1 (green) and doublecortin (DCX, red) in 8-week-old (Aa) and 3-week-old mice (Ba). White scale bars represent 50 μm . 240x magnification view of the DG are labelled for Kv4.1 (green) and doublecortin (DCX, red) in 8-week-old (Ab) and 3-week-old mice (Bb). White scale bars represent 5 μm . (Ca) Time course of anti-Kv4.1 antibody effects on K^+ current evoked by 1 s

pulse to +30 mV in immature DG-GC of 8-week-old (left, blue) and 3-week-old (right, black) mice. (Cb) Summary bar graph of inhibition of I_{peak} and I_{sus} in mature DG-GCs (red, same result from Fig. 3F), immature DG-GCs of 3-week-old (black, $n = 9$) and 8-week-old (blue, $n = 8$) mice by intracellular application of anti-Kv4.1 antibody. Values indicate mean \pm SEM. Error bars indicates SEM.

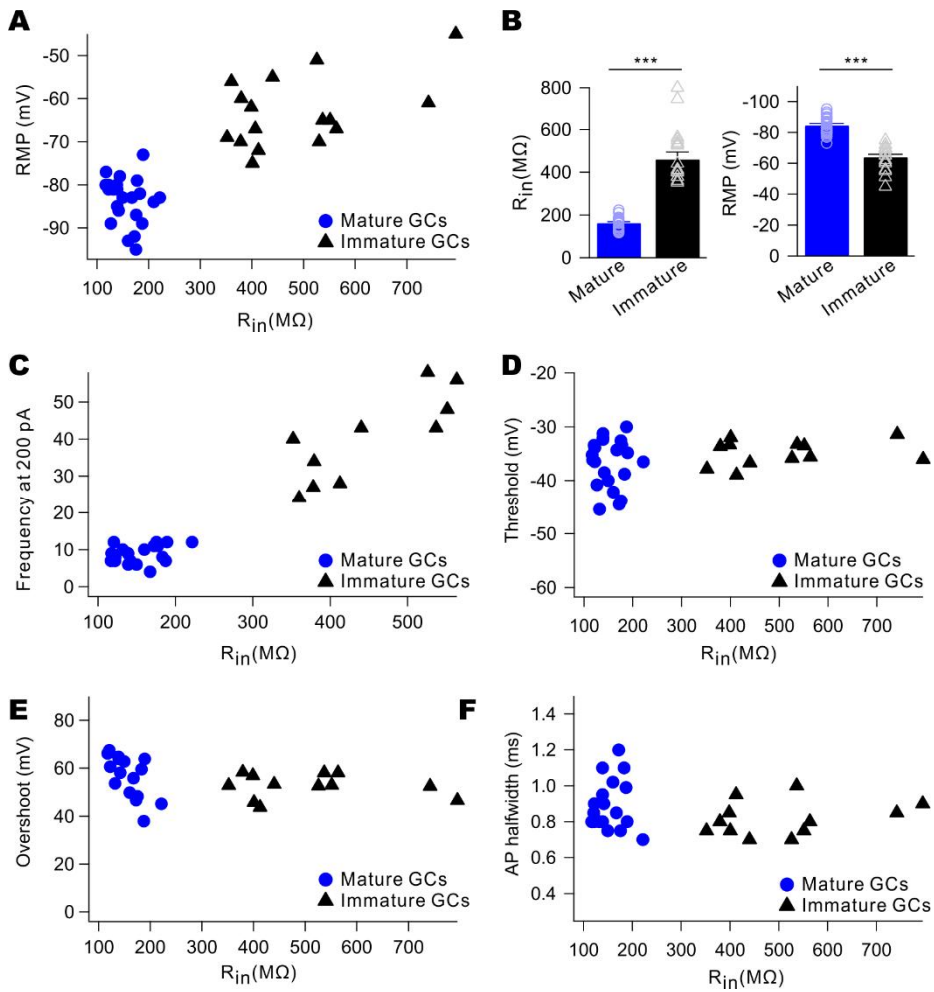


Figure 5. Comparison of intrinsic property between mature and immature GCs

(A, C–F) Resting membrane potential (RMP, A), firing frequency at 200 pA (C), voltage threshold (D), Overshoot (E), and action potential (AP) halfwidth (F) were plotted against input resistance (R_{in}) in DG-GCs. Black triangle represents immature DG-GCs and blue circle represents mature DG-GCs.

(B) Bar graph of R_{in} (left) and RMP (right) in immature ($n = 18$) and mature ($n = 25$) DG-GCs. Values indicate mean \pm SEM. Error bars indicates SEM.

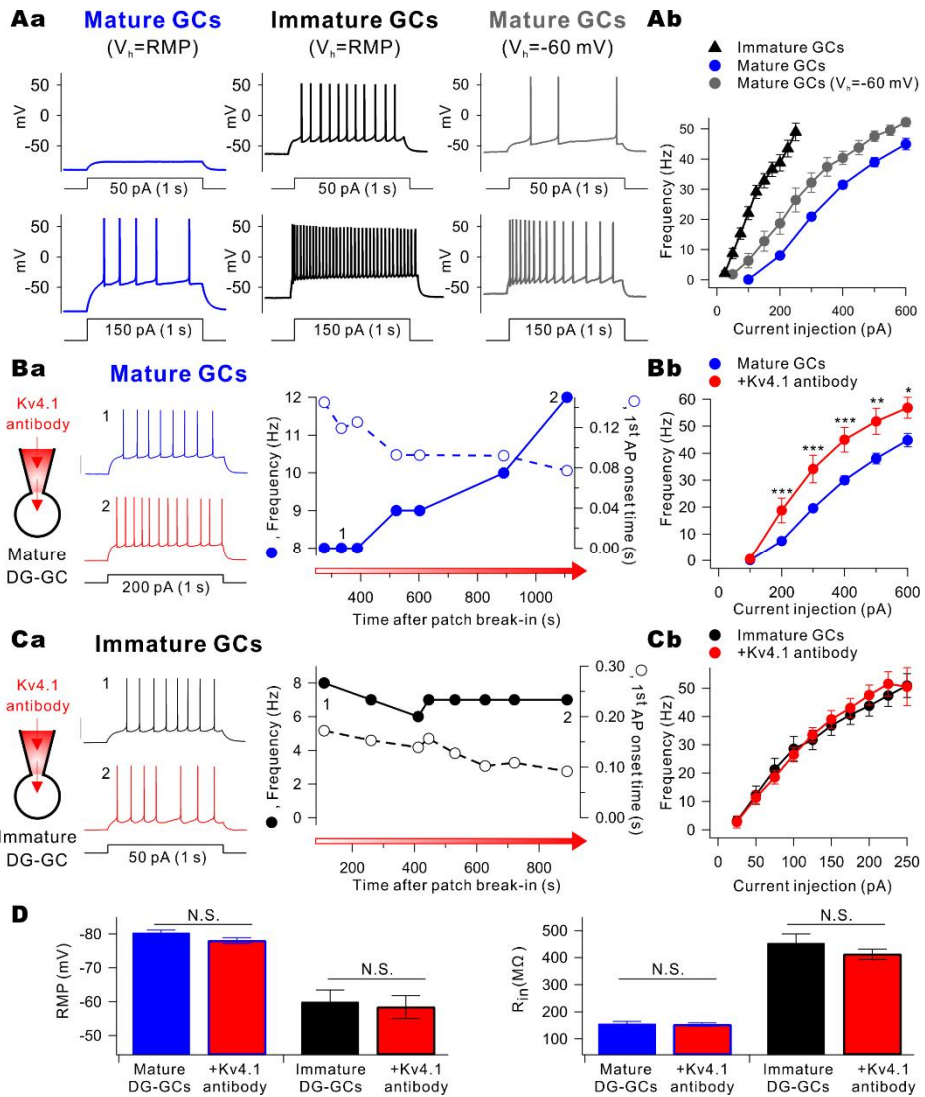


Figure 6. Comparison of electrical properties and contribution of anti-Kv4.1 antibody on firing frequency between mature and immature DG-GCs

(Aa) Voltage traces evoked in mature (left, blue, $n = 23$) and immature (middle, black, $n = 18$) DG-GCs by 1 s depolarizing

current pulse injection (Top, 50pA; Bottom, 150 pA) from the resting membrane potential (RMP). A subset of experiments in DG (right, gray, n = 6) was recorded from a holding potential of -60 mV to compare with the results in immature GCs. (Ab) Frequency (F) during 1 s current stimulation is plotted against the amplitude of injecting current (I, blue circle, mature GCs, n = 23; gray circle, mature GCs ($V_h = -60$ mV), n = 6; black triangle, immature GCs, n = 18). (B-C) Time course of the impact of the anti-Kv4.1 antibody on firing frequency in mature (Ba) and immature (Ca) GCs. Left traces, example train of APs measured after patch break in (1) or during an intracellular application of the anti-Kv4.1 antibody (2). Vertical scale bars indicate 40 mV. F-I curve in the absence and presence of the anti-Kv4.1 antibody (red) in mature (blue, Bb) and immature (black, Cb) DG-GCs. Mature GCs, n = 23, +anti-Kv4.1 antibody, n = 7; Immature GCs, n = 18, +anti-Kv4.1 antibody, n = 4. (D) Summary graph of RMP (left) and R_{in} (right) in the absence and presence of the anti-Kv4.1 antibody (red) in mature (blue) and immature (black). Error bars indicates SEM. Values indicate mean \pm SEM.

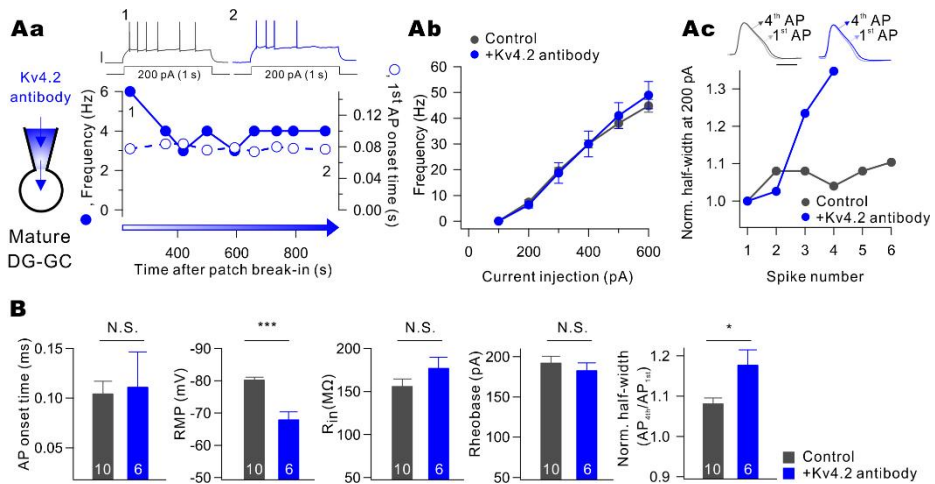


Figure 7. Contribution of anti-Kv4.2 antibody on firing frequency in mature DG-GCs

(Aa) Time course of the impact of the anti-Kv4.2 antibody on firing frequency (filled circle, left axis) and 1st AP onset time (open circle, right axis). Upper traces, example train of APs measured after patch break in (1) or during an intracellular application of the anti-Kv4.2 (blue) antibody (2). Vertical scale bar indicates 40 mV. (Ab) Number of spikes (F) during 1 s current stimulation were plotted against the amplitude of injecting currents (I). F-I curve in the absence (gray) and presence (blue) of the anti-Kv4.2 antibody (n = 6) in mature DG-GCs. (Ac) AP half-width are normalized to the 1st AP of the repetitive APs during 200 pA injection. Inset, superimposed

traces are the 1st and 4th AP of repetitive APs during 200 pA injection in the absence (left) and presence (right) of antibody. Scale bar indicates 1 ms. (B) Summary graph of AP onset time, RMP, R_{in} , and rheobase in the intracellular presence of K-glu+0.1 mM EGTA (control, gray, n = 10) and anti-Kv4.2 antibody (blue, n = 6). Error bars indicates SEM. Values indicate mean \pm SEM.

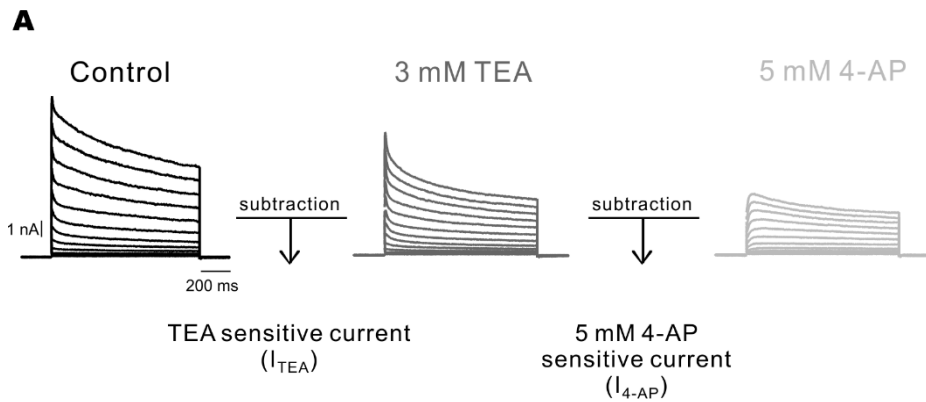


Figure 8. Scheme of K^+ current measurements in hippocampal cell

(A) Representative whole-cell, voltage-gated K^+ currents from Control DG-GCs. Currents were evoked in response to 1 s voltage steps to potentials between -60 mV to $+50$ mV from a holding potential of -70 mV. After recording the control (black), I changed the bath solution which contained 3 mM TEA (dark gray). 3 mM TEA blocked slow inactivated K^+ currents. The difference between the control and 3 mM TEA called TEA-sensitive currents (I_{TEA}). To isolate the A-type K^+ current, the bath solution was changed to contain 5 mM 4-AP (light gray) to block the A-type K^+ channel. The difference between the 3 mM TEA and 5 mM 4-AP called 5 mM 4-AP-sensitive currents (I_{4-AP}).

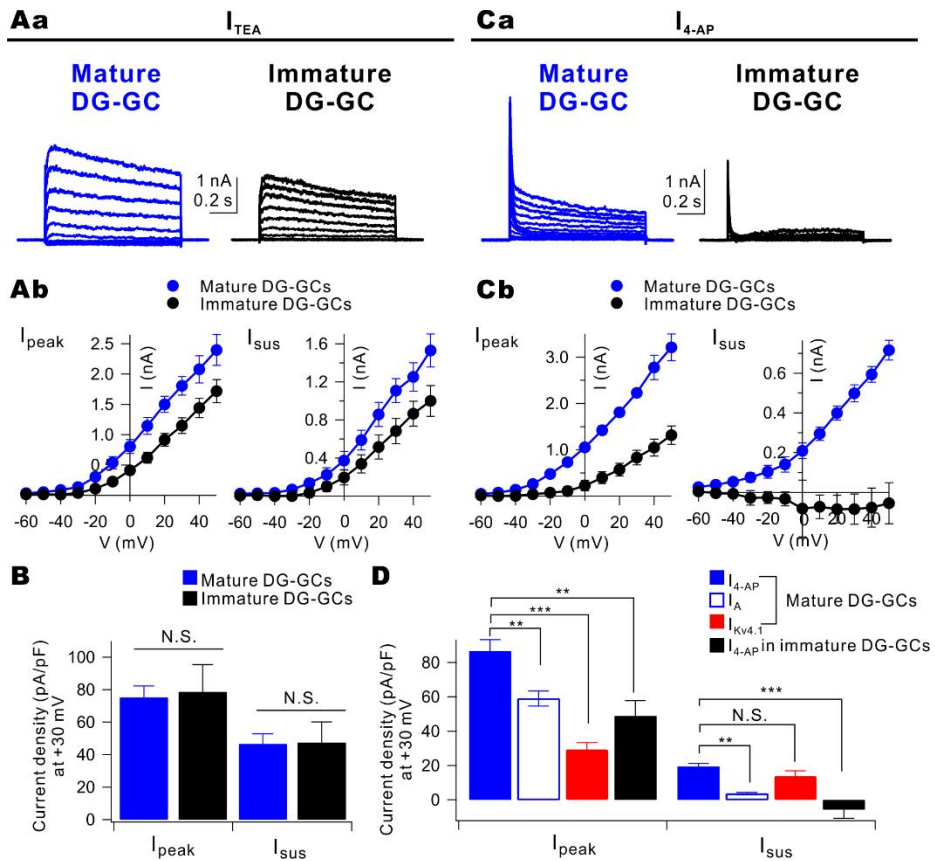


Figure 9. Comparison of K^+ current between mature and immature DG-GCs

Whole-cell, voltage-gated K^+ currents from DG-GCs were evoked in response to 1 s voltage steps to potentials between -60 mV to $+50$ mV from a holding potential of -70 mV. (Aa and Ca) Representative trace of TEA-sensitive current (I_{TEA} , Aa) and 4-AP-sensitive current (I_{4-AP} , Ca) from mature (blue) and immature (black) GCs. (Ab and Cb) Peak current (left, I_{peak})

and sustained current (right, I_{sus}) of I_{TEA} (Ab) and $I_{4\text{-AP}}$ (Cb) are plotted against the given voltage between mature (blue) and immature (black) GCs. (B) Summary graph of I_{TEA} current density at +30 mV in mature (blue) and immature (black) GCs. (D) Summary bar graph of $I_{4\text{-AP}}$ between mature (filled blue) and immature (filled black), and I_{A} (open blue bar) and $I_{\text{KV4.1}}$ (filled red) in mature DG-GCs. Capacitance, 25.63 ± 0.75 pF in mature ($n = 9$); 15.45 ± 1.52 pF in immature ($n = 4$). Error bars indicates SEM. Values indicate mean \pm SEM.

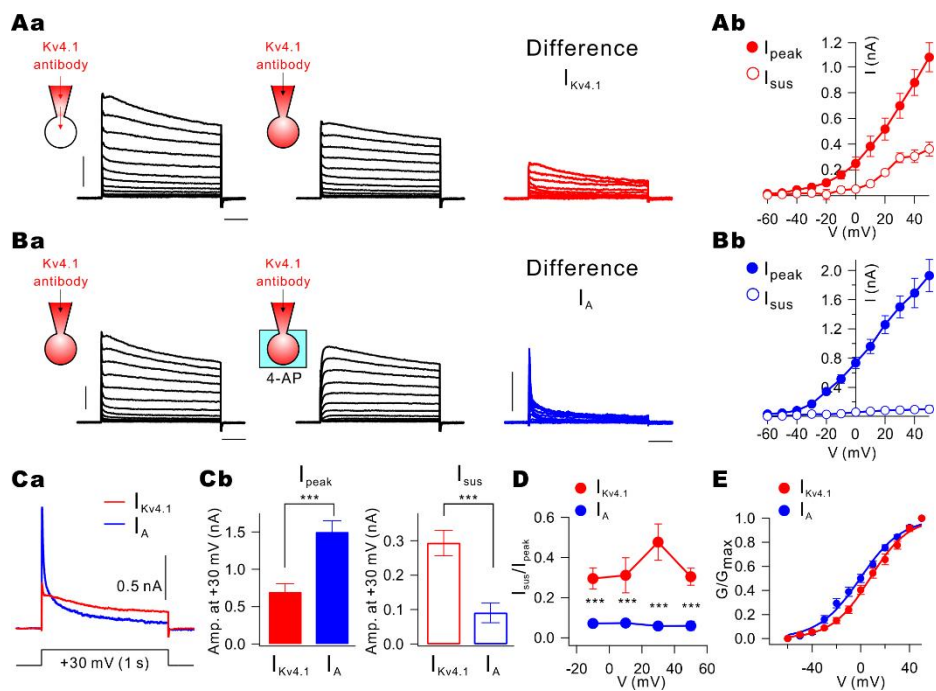


Figure 10. Characterization of Kv4.1-mediated currents using anti-Kv4.1 antibody

Whole-cell, voltage-gated K^+ currents from mature DG-GCs in the presence of 3 mM TEA. Currents were evoked in response to 1 s voltage steps to potentials between -60 mV to $+50$ mV from a holding potential of -70 mV. (Aa) K^+ currents were recorded in an intracellular application of the anti-Kv4.1 antibody after patch break-in (left) and 14 mins later (middle). Kv4.1 mediated currents ($I_{Kv4.1}$, red) were obtained by subtraction of the currents recorded after patch break-in from those recorded after 14 mins later. (Ba) I_A (right, blue) were

obtained by subtraction of the currents recorded in the presence of 5 mM 4-AP (middle) from those recorded in the absence of 4-AP (left). (Ab and Bb) I_{peak} (closed circle) and I_{sus} (open circle) for $I_{\text{KV4.1}}$ (red, Ab) and I_{A} (blue, Bb) are plotted against the given voltage. (Ca) $I_{\text{KV4.1}}$ (red, $n = 7$) and I_{A} (blue, $n = 10$) obtained at +30 mV was averaged and superimposed. (Cb) Bar graph showed the amplitude at +30 mV of I_{peak} (filled bar) and I_{sus} (open) for $I_{\text{KV4.1}}$ (red, $n = 7$) and I_{A} (blue, $n = 10$). (D) The $I_{\text{sus}}/I_{\text{peak}}$ for $I_{\text{KV4.1}}$ (red, $n = 7$) and I_{A} (blue, $n = 10$). (E) Activation curve for $I_{\text{KV4.1}}$ (red) and I_{A} (blue) in mature DG-GCs. The values of conductance were calculated from the respective peak currents and reversal potential of -95 mV. Each pair of traces was scaled to a normalized peak conductance. Data were fitted with a Boltzmann function. Error bars indicates SEM. Values indicate mean \pm SEM.

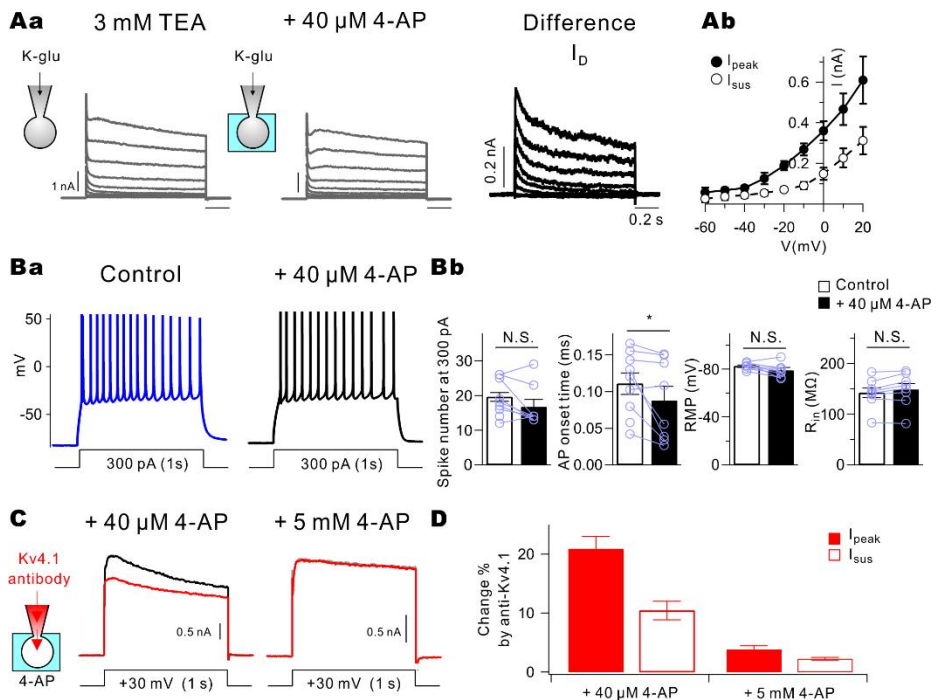


Figure 11. Contribution of D-type currents in DG-GCs

(Aa) Scheme of D-type K^+ Currents (I_D) measurement in DG-GCs. K^+ currents activated by 1 s voltage pulse from -60 to $+20$ mV ($+10$ mV step) from a holding potential of -70 mV. To measure the I_D , I applied $40 \mu\text{M}$ 4-AP to the bath solution to block the D-type K^+ channel. The difference between 3 mM TEA (left) and $40 \mu\text{M}$ 4-AP (middle) called $40 \mu\text{M}$ 4-AP-sensitive current (I_D , right, black). (Ab) I_{peak} (closed circle) and I_{sus} (open circle) for I_D are plotted as a function of the given potential (V). (Ba) APs evoked by 1 s depolarizing current

pulses (300 pA) in the absence (blue) and presence (black) of 40 μM 4-AP. (Bb) Bar graph summarizing the comparison of electrical properties (Number of spikes at 300 pA, AP onset time, RMP, R_{in}) of mature DG-GCs in the absence (open bar) and presence of (filled bar) 40 μM 4-AP. Lines are connected between data points from the same experiment. (C) The impact of the anti-Kv4.1 antibody internal on K^+ current during the bath application of 40 μM 4-AP (left) and 5 mM 4-AP (right). (D) Summary bar graph of inhibition of I_{peak} (filled) and I_{sus} (open) in the presence of anti-Kv4.1 antibody by the bath application of 40 μM 4-AP and 5 mM 4-AP. Error bars indicates SEM. Values indicate mean \pm SEM.

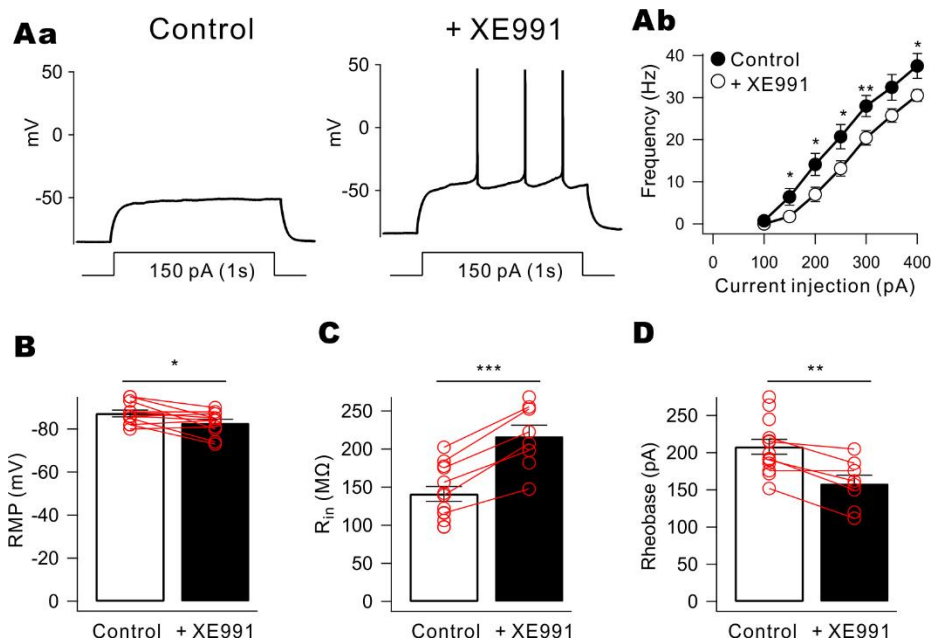


Figure 12. Contribution of KCNQ/M channels in mature DG-GCs

(Aa) APs evoked by 1 s depolarizing current pulses (150 pA) in the absence (left) and presence (right) of 10 μ M XE991. (Ab) F-I curve in the absence (closed circle, n = 13) and presence (open circle, n = 8) of XE991 in mature DG-GCs. (B-D) Bar graph summarizing the comparison of RMP (B), R_{in} (C), rheobase (D) of mature DG-GCs in the absence (open bar) and presence of (filled bar) XE991. Lines are connected between data points from the same experiment. Error bars indicates SEM. Values indicate mean \pm SEM.

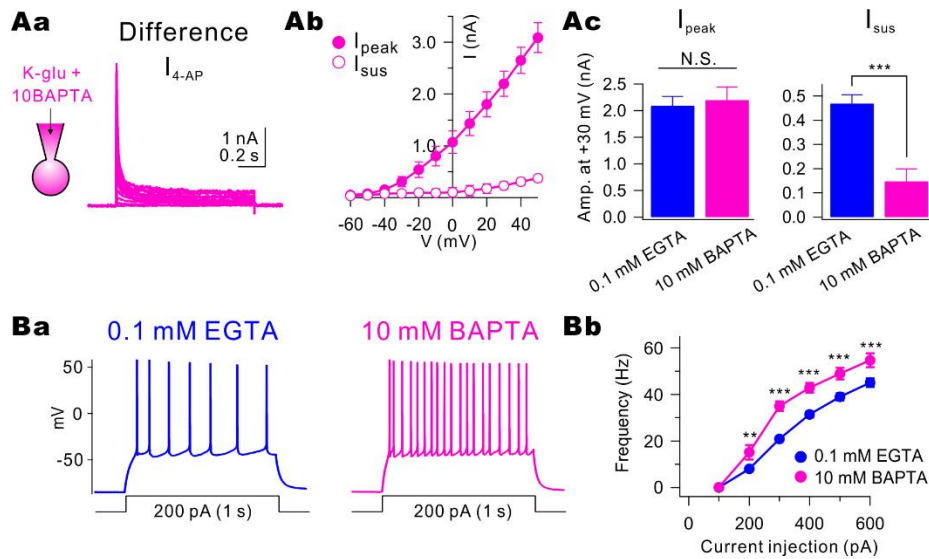


Figure 13. Ca^{2+} -sensitivity of Kv4.1 -mediated currents in mature DG-GCs

(Aa) I_{4-AP} were recorded in the presence of 10 mM BAPTA (I_{4-AP} , pink, $n = 5$) as described in the legend to Fig. 9A. (Ab) I_{peak} (closed circle) and I_{sus} (open circle) for I_{4-AP} in the presence of 10 mM BAPTA ($n = 5$). (Ac) Bar graph showed the amplitude at +30 mV of I_{peak} (left) and I_{sus} (right) for I_{4-AP} in the absence (blue, $n = 9$) or presence of 10 mM BAPTA (pink, $n = 5$) (Ba) Representative trace from mature DG-GCs response to 200 pA current injection (1 s duration) in an intracellular application of the 0.1 mM EGTA (blue) or 10 mM BAPTA (pink). (Bb) The F-I curve from mature DG-GCs

(from 100 pA to 600pA, +100 pA increment) in an intracellular application of the 0.1 mM EGTA (blue, n = 25) and 10 mM BAPTA (pink, n = 11). Error bars indicates SEM. Values indicate mean \pm SEM.

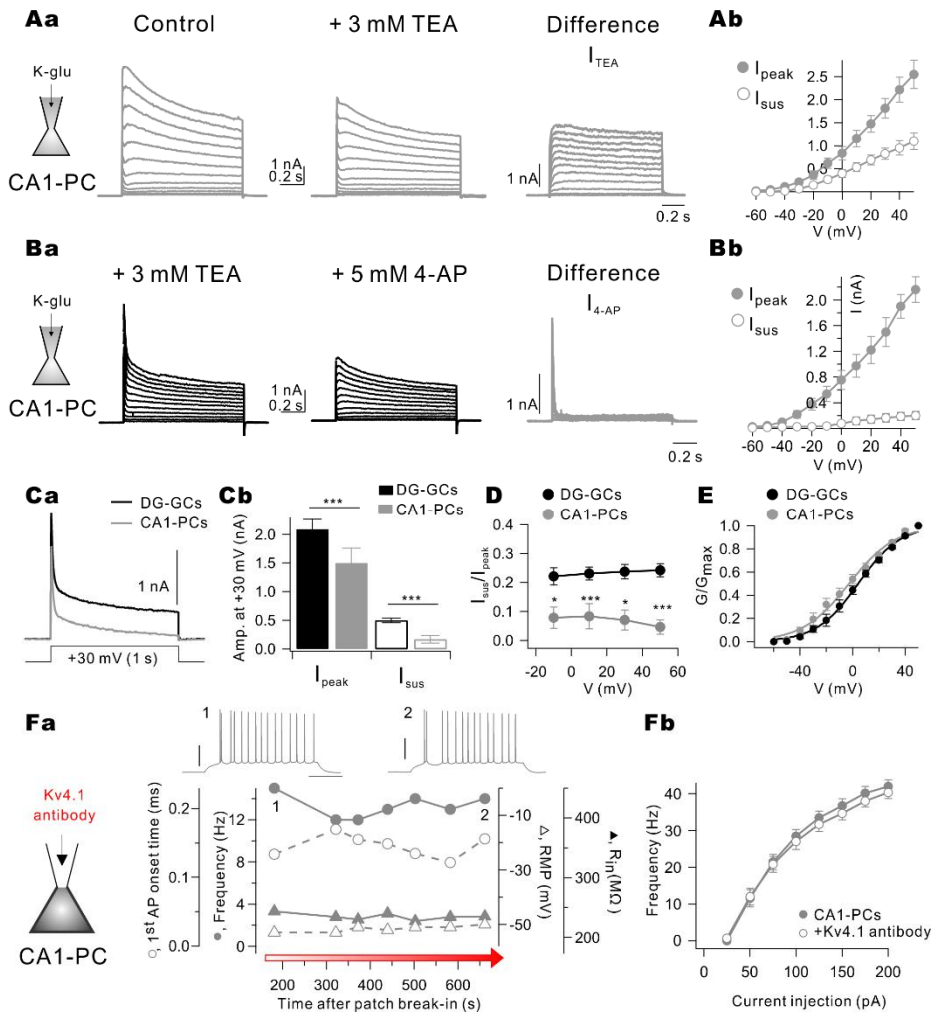
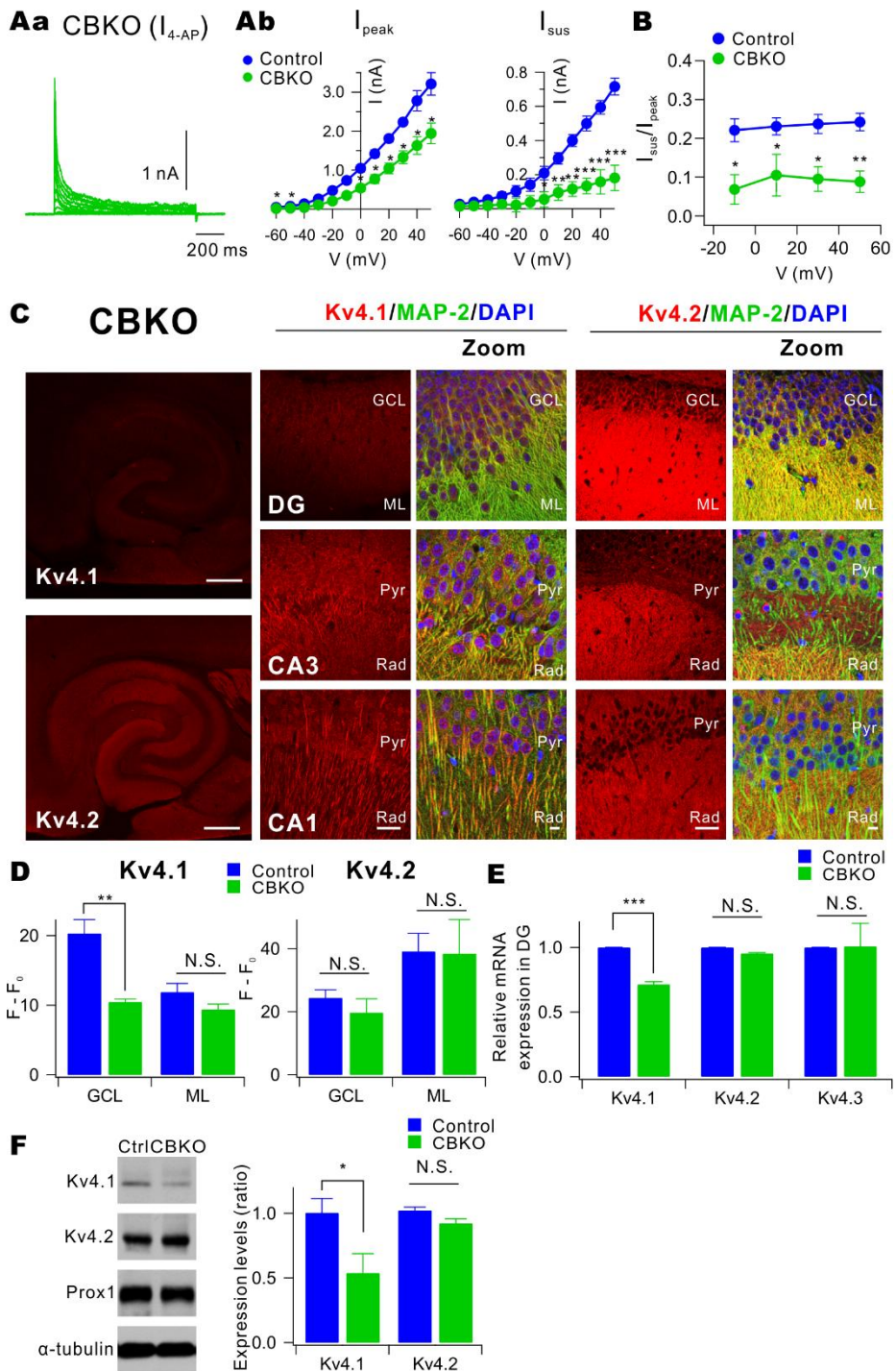


Figure 14. Contribution of Kv4.1 and comparison of outward K^+ current in CA1-PCs.

(Aa) K^+ currents were recorded in CA1-PCs before (left) and after (middle) bath application of 3 mM TEA. The I_{TEA} (right, gray) were obtained by subtraction of the currents recorded in the presence of 3 mM TEA from those recorded in the absence

of TEA. I_{TEA} in CA1-PCs activated by 1 s voltage pulse from -60 to +50 mV (+10 mV step) from a holding potential of -70 mV were averaged and superimposed (gray, n = 9). (Ab) I_{peak} (closed circle) and I_{sus} (open circle) of I_{TEA} for CA1-PCs (gray) are plotted against the given voltage. (Ba) K^+ currents were recorded in CA1-PCs before (left) and after (middle) bath application of 5 mM 4-AP. The I_{4-AP} (right, gray) were obtained by subtraction of the currents recorded in the presence of 5 mM 4-AP from those recorded in the absence of 4-AP. I_{4-AP} in CA1-PCs activated by 1 s voltage pulse from -60 to +50 mV (+10 mV step) from a holding potential of -70 mV were averaged and superimposed (gray, n = 6). (Bb) I_{peak} (closed circle) and I_{sus} (open circle) of I_{4-AP} for CA1-PCs (gray) are plotted against the given voltage. (Ca) I_{4-AP} in DG-GCs (black, n = 12) and CA1-PCs (gray, n = 6) obtained at +30 mV was averaged and superimposed. (Cb) Bar graph showed the amplitude at +30 mV of I_{peak} (filled) and I_{sus} (open) for I_{4-AP} in DG-GCs (black, n = 12) and CA1-PCs (gray, n = 6) (D) The I_{sus}/I_{peak} for DG-GCs (black, n = 12) and CA1-PCs (gray, n = 6). (E) Activation curve for I_{4-AP} in DG-GCs (black, n = 5) and CA1-PCs (gray, n = 4). The values of conductance were

calculated from the respective peak currents and reversal potential of -95 mV. Each pair of traces was scaled to a normalized peak conductance. Data were fitted with a Boltzmann function. (Fa) Time course of the impact of the anti-Kv4.1 antibody on firing frequency in CA1-PCs. Upper traces, example train of APs measured after patch break in (1) or during an intracellular application of the anti-Kv4.1 antibody (2). Vertical and horizontal scale bars indicate 40 mV and 300 ms, respectively. (Fb) The F-I curve from CA1-PCs (from 25 pA to 200pA, +25 pA increment) in an intracellular application of the 0.1 mM EGTA (closed circle, $n = 7$) and anti-Kv4.1 antibody (open circle, $n = 7$). Error bars indicates SEM. Values indicate mean \pm SEM.



$I_{Kv4.1}$ in DG of CBKO

(Aa) I_{4-AP} were recorded from CBKO DG-GCs (I_{4-AP} , green, $n = 8$) (Ab) I_{peak} (left) and I_{sus} (right) for I_{4-AP} in the Control (same results shown in Fig. 9Cb) and CBKO DG-GCs (green, $n = 8$). (B) The I_{sus}/I_{peak} for Control (blue, same results shown in Fig. 14D) and CBKO DG-GCs (green, $n = 8$). (C) Left, 5x magnification view of immunohistochemical localization of Kv4.1 (upper) and Kv4.2 (lower) subunits in the hippocampus area of 2-month-old CBKO mice immunostained with antibodies against Kv4.1 and Kv4.2 subunits. Scale bars represent 500 μm . 2nd panel and 4th panel, 40x magnification view of the hippocampus are Kv4.1 or Kv4.2. Scale bar represents 50 μm . Zoom panel, 80x magnification view of the hippocampus in triple-labelled for DAPI (blue), MAP-2 (green) and Kv4.1 (red), or Kv4.2 (red) antibody. Scale bar represent 10 μm . (D) Summary bar graph of $F-F_0$ shown in 5X magnification view of DG for Kv4.1 or Kv4.2 in Control (blue, $n = 10$) and CBKO (green, $n = 4$) mice. GCL, granule cell layer; ML, molecular layer; Pyr, pyramidal layer; Rad, striatum radiatum. (E) mRNA expression profile of 3 different Kv4 channel sub units in DG of control (blue) and CBKO (green) mice. Relative mRNA

expression levels normalized to GAPDH. (F) Acute hippocampal slices were isolated from DG of C57BL/6 (control) and CBKO mice, and solubilized as described in Material and Method. The endogenous protein expression levels were analyzed by Western blotting with the indicated antibodies. Prox1 expression defines DG neurons. Bar graph data represent the means of Kv4.1 or Kv4.2 expression \pm SEM (Kv4.1 in Control, 1.00 ± 0.1 ; Kv4.1 in CBKO, 0.53 ± 0.15 , $n = 6$; $p < 0.03$, paired *t*-test; Kv4.2 in Control, 1.02 ± 0.03 ; Kv4.2 in CBKO, 0.92 ± 0.03 ; $n = 4$). Error bars indicates SEM. Values indicate mean \pm SEM.

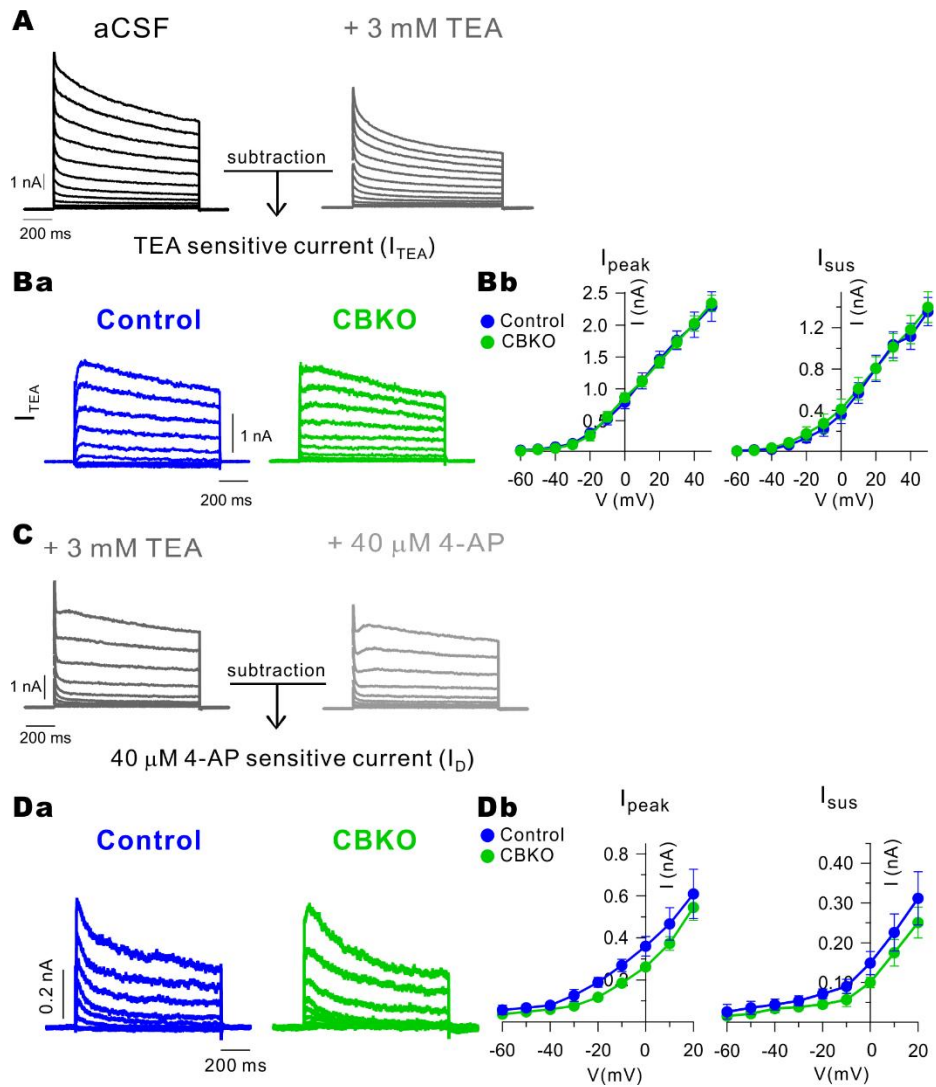


Figure 16. Contribution of I_{TEA} and I_D in CBKO DG-GCs

(A) Scheme of I_{TEA} from DG-GCs. K^+ currents were evoked in response to 1 s voltage steps to potentials between -60 mV to $+50$ mV from a holding potential of -70 mV. After recording the control (black), I changed the bath solution which contained 3 mM TEA (dark gray). 3 mM TEA blocked slow inactivated K^+

currents. The difference between the control and 3 mM TEA called I_{TEA} . (Ba) Example of isolated I_{TEA} in DG-GCs from control (blue, same results shown in Fig. 9Aa) and CBKO (green, $n = 9$) mice by 1 s voltage pulses from -60 to $+50$ mV. (Bb) Amplitudes of the I_{peak} (left) and I_{sus} (right) for I_{TEA} are plotted versus stimulation voltage. Blue symbol indicates the data from control mice (same results shown in Fig. 9Ab), whereas green symbols shows the one from CBKO mice ($n = 9$). (C) Scheme of I_{D} measurement in DG-GCs. K^+ currents activated by 1 s voltage pulse from -60 to $+20$ mV ($+10$ mV step) from a holding potential of -70 mV. To measure I_{D} , I applied $40 \mu\text{M}$ 4-AP to the bath solution to block the D-type K^+ channel. The difference between 3 mM TEA and $40 \mu\text{M}$ 4-AP called I_{D} . (Da) I_{D} were averaged and superimposed in control (blue, same results shown in Fig. 11Aa) and CBKO (green, $n = 4$). (Db) I_{peak} and I_{sus} for I_{D} are plotted as a function of the given potential (V). Blue symbol indicates the data from control mice (same results shown in Fig. 11Ab), whereas green symbols shows the one from CBKO mice ($n = 4$). Error bars indicates SEM. Values indicate mean \pm SEM.

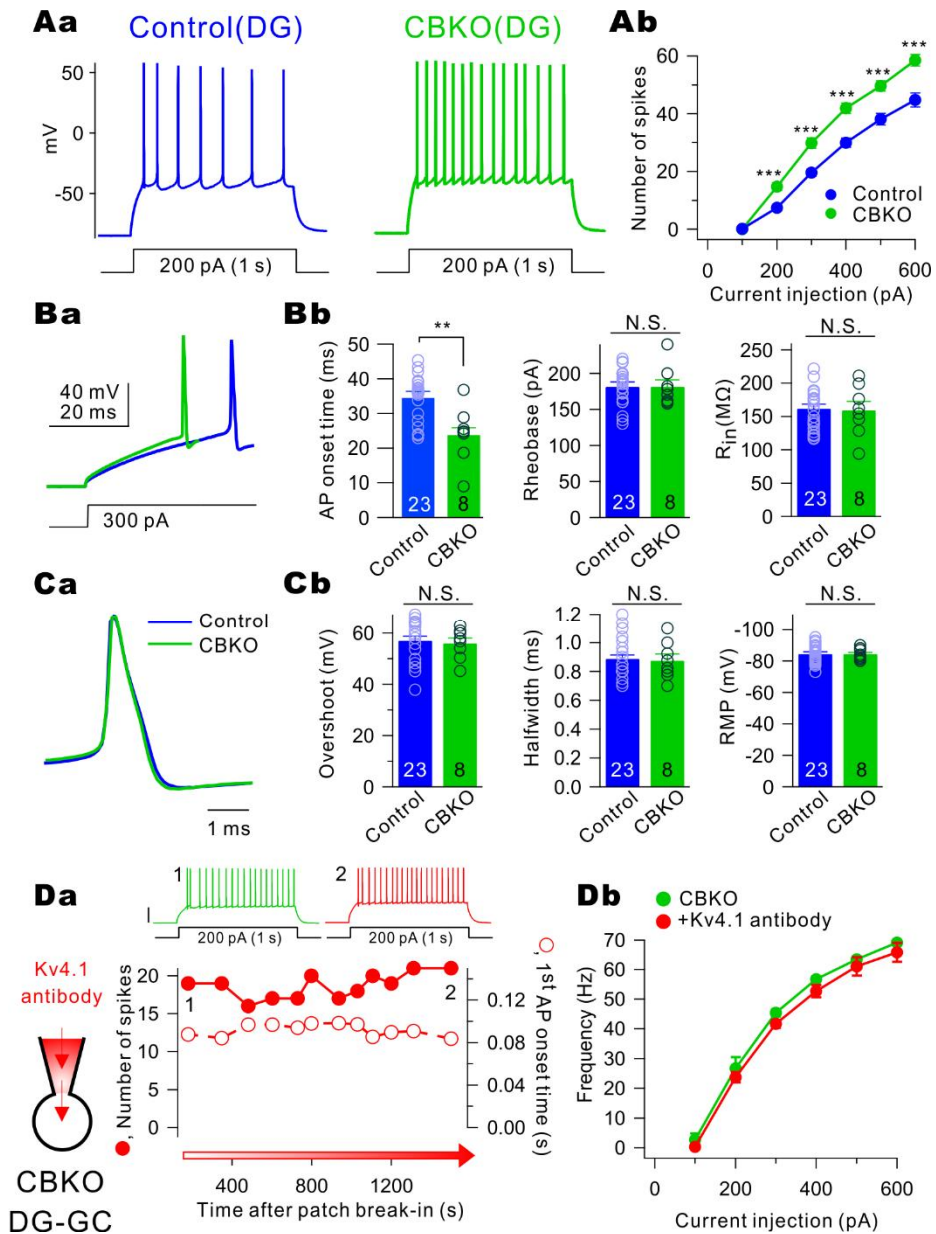


Figure 17. Increased firing frequency in DG-GCs of CBKO

(Aa) Train of APs induced in mature DG-GCs of control (blue) and CBKO (green) mice by 1 s depolarizing current injection.

(Ab) The F-I curves in control (blue, same results shown in

Fig. 6Ab) and CBKO (green, $n = 8$). (Ba) Expanded view of overlaid 1st APs evoked by current injection (300 pA). (Bb) The bar graph showing the 1st AP onset time at 300 pA current injection, rheobase, and R_{in} of DG-GCs in control (blue) and CBKO (green) mice. Circles represent data from individual experiments and bars indicate mean \pm SEM. (Ca) Expanded view of overlaid single APs evoked by current injection. (Cb) Bar graph summarizing the comparison of electrical properties (Left, overshoot; Middle, half-width; right, RMP) (Da) Time course of the impact of the anti-Kv4.1 (red) antibody on firing frequency (filled circle, left axis) and 1st AP onset time (open circle, right axis). Upper traces, example train of APs measured after patch break in (1, green) or during an intracellular application of the anti-Kv4.1 antibody (2, red). Vertical scale bar indicate 40 mV. (Db) Number of spikes (F) during 1 s current stimulation were plotted against the amplitude of injecting currents (I). F-I curve in the absence (green, $n = 3$) and presence of the anti-Kv4.1 antibody (red, $n = 3$) antibody in CBKO DG-GCs. Error bars indicates SEM. Values indicate mean \pm SEM.

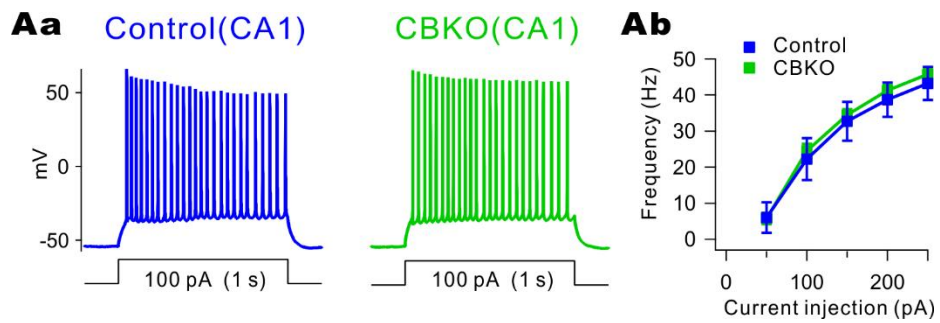


Figure 18. Firing frequency of CA1-PCs in Control and CBKO

(Aa) Representative traces of current-clamp recordings from CA1 of control (blue, left) and CBKO mice (green, right). A train of APs were evoked by 1 s depolarizing current pulse injection (100 pA). (Ab) The F-I curve for CA1 from control (n = 10) and CBKO (n = 12) mice. Error bars indicates SEM. Values indicate mean \pm SEM.

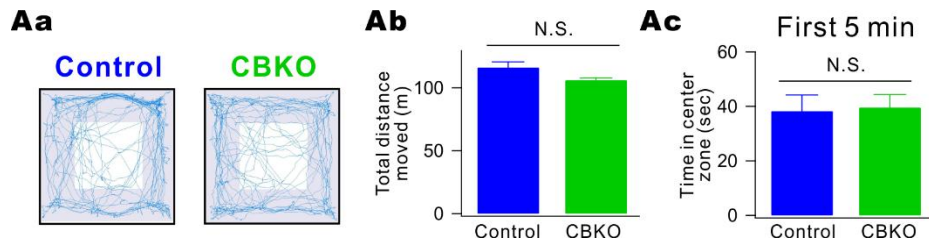
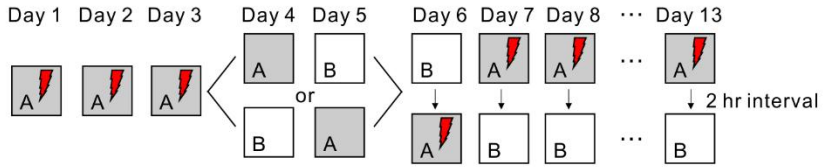


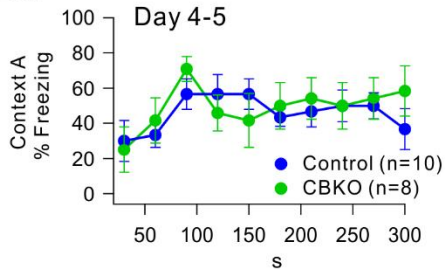
Figure 19. The level of anxiety and locomotor activity between Control and CBKO

(Aa) The trajectories traveled by the control (left, n = 6) and CBKO (right, n = 6) mice in the open field test showed how the mice traveled. (Ab–Ac) Summary bar graph of the total traveled distance (Ab) and time in center zone during first 5 min (Ac). Total distance moved (m), Control, 116.20 ± 4.45 , CBKO, 106.11 ± 1.79 , $p > 0.05$; Time in center zone (sec), Control, 11.81 ± 1.22 , CBKO, 13.91 ± 1.55 , $p > 0.3$. Error bars indicates SEM. Values indicate mean \pm SEM.

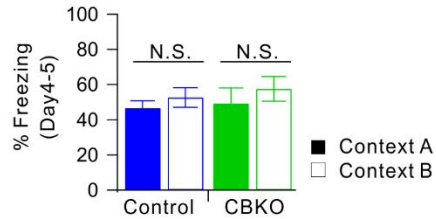
A Pattern separation



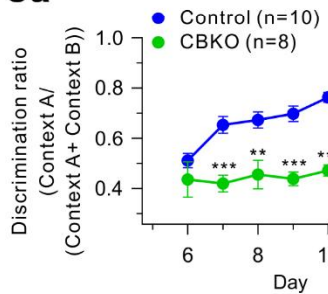
Ba



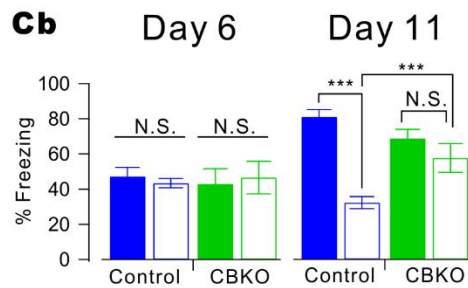
Bb



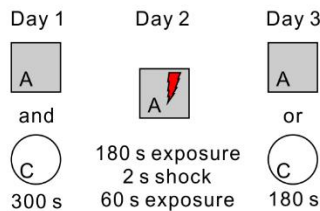
Ca



Cb



Da



Db

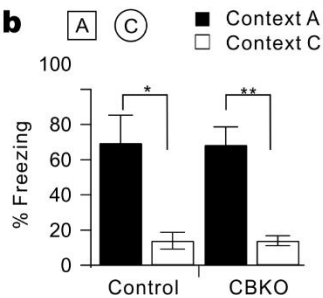


Figure 20. Impaired pattern separation in CBKO mice

(A) Experimental procedure for pattern separation in 15- to 19-week-old control (n = 10) and CBKO (n = 8) mice. (Ba) On day 4 to 5, the kinetics of freezing across the 5 min test in

context A. (Bb) The percentage of freezing in A (filled bar) and B (open bar) during day 4 to 5 in both contexts (A and B). Control (blue, n = 10) and CBKO (red, n = 8) mice displayed equal amounts of freezing in both contexts (A and B). (Ca) On day 6 to 13, time course of the discrimination ratio in control (blue, n = 10) and CBKO (red, n = 8) mice. (Cb) The percentage of freezing in context A (filled bar) and context B (open bar) for the control (blue, n = 10) and CBKO (red, n = 8) mice on day 6 (left) and day 11 (right). (Da) Experimental procedure for one-trial contextual fear conditioning between control (n = 8) and CBKO (n = 8) mice (Db) The percentage of freezing in context A (filled bar) and context C (open bar, distinct object) for the control (n = 8) and CBKO (n = 8) mice. Error bars indicates SEM. Values indicate mean \pm SEM.

	I_{4-AP} in DG-GCs (n = 12)	I_{TO} in DG-GCs (n = 10)	I_{4-AP} in CA1-PCs (n = 4)	I_{4-AP} in CBKO DG-GCs (n = 6)
A_{fast} (nA)	1.20 ± 0.15	1.25 ± 0.13	1.26 ± 0.40	1.03 ± 0.05
A_{slow} (nA)	0.80 ± 0.07	0.32 ± 0.03**	0.44 ± 0.07 ^{†††}	0.37 ± 0.11 ^{††}
τ_{fast} (ms)	22.71 ± 2.28	21.67 ± 5.19	15.61 ± 3.06	19.04 ± 2.63
τ_{slow} (ms)	1378.52 ± 224.46	1111.0 ± 213.90	891.19 ± 60.38	1001.68 ± 140.13

Table 1. Double exponential fitting data of I_{4-AP} at +30 mV

The statistical significances were evaluated using Student's t-test, and the level of significance was indicated by the number of marks (*, $P < 0.05$; **, $P < 0.01$; ***, $P < 0.001$). *, I_{4-AP} vs I_A in, †, I_{4-AP} in DG-GCs vs I_{4-AP} in CBKO DG-GCs, ††, I_{4-AP} in DG-GCs vs I_{4-AP} in CA1-PCs.

DISCUSSION

In the present study, I characterized the properties of $I_{Kv4.1}$ in mature DG-GCs using an anti-Kv4.1 antibody and found that the kinetics of $I_{Kv4.1}$ were markedly different from those of classical I_A . The data shows slow inactivation kinetics, thus contributing to sustained outward currents during long depolarization pulses (Fig. 10). I identified the conditions where $I_{Kv4.1}$ was suppressed (immature DG-GCs, application of an anti-Kv4.1 antibody in mature DG-GCs, and mature DG-GCs of CBKO), which equally increased firing frequency in mature DG-GCs, with little effect on resting membrane properties such as RMP or R_{in} (Fig. 6D). In contrast, the contribution of $I_{Kv4.1}$ was negligible in immature GCs and CA1-PCs (Figs. 6Ca and 14). Preferential expression of the Kv4.1 subunit in mature DG-GCs in the hippocampus was also confirmed by immunohistochemistry analysis (Figs. 1 and 4). Therefore, it can be concluded that $I_{Kv4.1}$ is a key mechanism for limiting firing frequency in mature DG-GCs and that reduced Kv4.1 expression results in increased firing frequency in mature DG-GCs. Furthermore, the functional contribution of Kv4.1 appears

to be specific for mature DG–GCs, implying that Kv4.1 may be a good target for selectively manipulating DG function.

In theoretical models, the DG was recognized as a potential source of pattern separation, and a series of electrophysiological studies in rodents, as well as high resolution fMRI studies in humans, supports the predictions of these models (Bakker et al., 2012; Leutgeb et al., 2007; Rolls and Kesner, 2006). Minimal changes in the shape of the environment can alter correlated activity patterns among place–modulated DG–GCs, while further changes recruit new cell populations in the CA3 subregion (Leutgeb et al., 2007). Furthermore, rats with localized DG lesions are unable to discriminate novel and familiar environments, which is an indication of impaired pattern separation (Hunsaker et al., 2008). Despite ample evidence that the DG is the center of pattern separation, the intrinsic properties of DG–GCs are not well understood. In the present study, I presented CBKO mice as a novel model exhibiting deficits in pattern separation. By using this model where DG–GCs show reduced Kv4.1 expression, I propose that maintenance of sparse firing in DG–GCs by Kv4.1 channels is crucial for normal pattern separation.

Characteristics and roles of Kv4.1 vs. other K⁺ channels

Among the Kv4 family, the characteristics and roles of Kv4.2 channels are the most widely studied. My study clearly showed that the characteristics and roles of Kv4.1 are distinct from those of Kv4.2. With respect to inactivation kinetics, it could be argued that $I_{Kv4.1}$ appear to resemble I_D that are known to be mediated by Kv1 family channels (Grissmer et al., 1994; Storm, 1988). I found that I_D are present in mature DG-GCs, but 40 μ M 4-AP does not significantly affect the electrical properties of DG-GCs, including firing frequency (Fig. 11B). By contrast, an anti-Kv4.1 antibody increased firing frequency of mature DG-GCs (Fig. 6B). These results suggest that $I_{Kv4.1}$ are not sensitive to 4-AP at a low concentration (40 μ M) and are distinct from I_D . I also showed that $I_{Kv4.1}$ are sensitive to 5 mM 4-AP, not to 40 μ M (Figs. 11C and 11D), but the kinetics of inactivation are distinct from typical I_A . Since $I_{Kv4.1}$ are slowly inactivating and sustained, contributing to the sparseness of AP firing in mature DG-GCs. However, I did not investigate the molecular mechanisms underlying slow inactivation of $I_{Kv4.1}$ in

mature DG-GCs. Inactivation of Kv4.1 currents expressed in oocytes was reported to be slower than that of Kv4.2 currents (median inactivation time, 80 vs. 26 ms, (Nakamura et al., 2001)), but it is still far faster than the $I_{Kv4.1}$ in mature DG-GCs shown in the present study. Possibly, other Kv4 accessory subunits may underlie the slow inactivation kinetics of Kv4.1 channels in mature DG-GCs. However, this possibility needs to be investigated in future studies.

I showed that characteristics of the rapidly inactivating component of I_{4-AP} are not significantly different between mature DG-GCs and CA1-PCs, and they are similar to those of A-type K^+ currents reported previously (Birnbaum et al., 2004). In CA1-PCs, I_A were shown to be mediated by Kv4.2, and Kv4.2-mediated currents mainly regulate action potential repolarization phase (Chen et al., 2006; Kim et al., 2007; Kim et al., 2005). In mature DG-GCs, however, I found that there was a significant effect on action potential duration (Fig. 7Ac) and RMP in DG-GCs (Fig. 7B). In spite that activation voltage for Kv4.2 was more negative than Kv4.1, such a large effect of Kv4.2 on RMP of DG-GCs was rather surprising considering that DG-GCs have highly negative RMP. Future studies are

required to verify that the effects of anti-Kv4.2 antibody were indeed attributable to Kv4.2 blockade.

Kv7 K^+ currents are well known to regulate the excitability of many peripheral and central neurons (Battfeld et al., 2014; Martinello et al., 2015; Shah et al., 2008). Pharmacological blockade of Kv7 currents induced a similar increase in firing frequency both in CA1-PCs and DG-GCs (Martinello et al., 2015; Shah et al., 2008). The increased firing frequency by Kv7 blockade was associated with a decrease in AP threshold and depolarization of RMP, which is distinct from the increased firing frequency by Kv4.1 blockade (Fig. 12). I investigate the role of KCNQ/M channel in the present study, the firing frequency was increased in application of XE991 (Fig. 12Ab), but the change in firing frequency after application of XE991 was correlated with a depolarization of RMP and an increased R_{in} (Figs. 12B and 12 C). Taken together, it can be concluded that both Kv7 and Kv4.1 suppress firing of DG-GCs, but with different mechanisms, and that only Kv4.1 is a selective regulator for DG-GCs.

Pathophysiological implications of calbindin deficits in DG-GCs

Cytosolic Ca^{2+} buffers are essential components for the maintenance of Ca^{2+} homeostasis and the shaping of Ca^{2+} signals (Schwaller, 2012). CB is a major Ca^{2+} buffer in mature DG-GCs of the hippocampus (Celio, 1990), where one half of the Ca^{2+} buffering capacity is attributable to CB (Lee et al., 2009). As CB is typically a mobile fast Ca^{2+} buffer, previous studies on the role of CB mostly focused on how it affects the shaping of the spatiotemporal extent of Ca^{2+} signals (Blatow et al., 2003). To the best of our knowledge, no evident behavioral phenotype was reported for CBKO mice, except impaired motor coordination (Airaksinen et al., 1997; Schwaller, 2012), and this impairment was understood to be a consequence of alterations in the time course or amplitude of synaptically evoked Ca^{2+} transients. My results show for the first time that Ca^{2+} dysregulation caused by the loss of the fast Ca^{2+} buffer CB can affect gene expression.

CBKO mice do not exhibit any specific disease but it can be useful for studying the pathophysiological significance of

reduced CB expression found in various diseases. Reduced CB expression in the DG is a well-known feature of temporal lobe epilepsy (Carter et al., 2008; Magloczky et al., 1997). Interestingly, CB expression in the DG is markedly reduced in neurological or psychiatric disorders that are accompanied by cognitive dysfunction, such as Alzheimer's disease (Palop et al., 2003; Stefanits et al., 2014), schizophrenia, and bipolar disorder (Altar et al., 2005; Miyakawa et al., 2003; Yamasaki et al., 2008). However, it is unclear whether reduced CB expression in the DG is merely an epi-phenomenon of these diseases or if it underlies DG dysfunction that leads to behavioral abnormalities. The behavioral phenotypes I observed in CBKO mice support the view that Ca^{2+} buffering deficits may be causally related to hyperexcitability of DG-GCs, which may lead to cognitive deficits.

Taken together, I propose that dysregulated Ca^{2+} homeostasis caused by Ca^{2+} buffering deficits in DG-GCs induces ion channel remodeling, which contributes to neuronal hyperexcitability, which may in turn contribute to impaired pattern separation. My study provides not only novel insights into the mechanisms and roles of the intrinsic excitability of

DG-GCs but also a new model for investigating pathophysiological mechanisms involving Ca^{2+} dysregulation.

CHAPTER 2

Links between reduced expression
of Kv4.1 and hyperexcitability of
dentate granule cell
in Alzheimer's disease model mice

INTRODUCTION

Alzheimer' s disease (AD) is a progressive neurodegenerative disorder and is the most common cause of dementia. Considerable evidence has indicated that AD patients exhibit cognitive deficits several years before clinical diagnosis (Backman et al., 2005; Chen et al., 2001; Elias et al., 2000). In particular, assessment of episodic memory is the most effective method to identify at-risk individuals (Elias et al., 2000; Small et al., 1997). The hippocampus is involved in the formation of episodic memory, and different subregions within the hippocampus (dentate gyrus (DG), CA3, and CA1) have been suggested to have distinct functions (Rolls and Kesner, 2006). To understand the underlying mechanisms involved in AD-related impairment of episodic memory, it will be critical to perform subregion-specific functional analyses in the early preclinical stage of the disease. I recently reported that the earliest functional disturbances in the AD model mice (Tg2576) were detected at the age of 1-2 months in granule cells (GCs) in the DG, which include impairment of mitochondrial Ca^{2+}

uptake and deficit in post-tetanic potentiation in mossy fiber-CA3 synapse (Lee et al., 2012). I further showed that oxidative stress associated with $A\beta_{1-42}$ underlies these alterations and that the $A\beta_{1-42}$ level in the DG region of the Tg2576 mouse brain at this age is higher than that in other areas (0.3 ng/mg vs 0.15 ng/mg). My results suggest that the DG is very susceptible to $A\beta$ -induced oxidative changes and its functional impairment leads to impaired information processing from the DG to area CA3.

AD is associated with an increased incidence of unprovoked seizures (Amatniek et al., 2006; Hauser et al., 1986). Seizure activity in AD has been interpreted as a secondary process resulting from advanced stages of neurodegeneration, but recent studies have raised the new possibility that aberrant excitatory neuronal activity represents a primary upstream mechanism which may contribute to the cognitive deficits in AD (Minkeviciene et al., 2009; Palop et al., 2007; Palop and Mucke, 2009). Importantly, seizure activity increases extracellular $A\beta$ levels (Cirrito et al., 2005), possibly initiating a vicious cycle that facilitates progressive pathology and memory impairment (Noebels, 2001). In this

respect, identification of targets that underlie seizure activity may be of great importance for understanding AD pathogenesis. Recently, the hyperexcitability of layer 2/3 (L2/3) pyramidal neurons (Minkeviciene et al., 2009) and the dysfunction of parvalbumin-positive interneurons in L2/3 parietal cortex (Verret et al., 2012) was proposed to be responsible for the abnormalities in oscillatory rhythms and network synchrony in AD model mice. Hyperexcitability of DG-GCs has long been known as one of epileptogenic mechanisms underlying temporal lobe epilepsy (TLE) (Sloviter, 1983; Sloviter et al., 2012). In addition, there are similarities between TLE and AD-associated seizures (Palop et al., 2007). However, it has never been investigated whether the excitability of DG-GCs is altered in AD mouse models.

In the present study, I found that reduced sustained component of 5 mM 4-AP sensitive currents (I_{4-AP}) in DG-GCs is profoundly reduced in 1-2 month-old Tg2576 mice to a level comparable to wild-type littermate (WT) mice. I not only identify the underlying mechanisms for the hyperexcitability in Tg2576 DG-GCs, but also provide evidence for the causal link between reduced Kv4.1 expression and neuronal

hyperexcitability that can be induce impairment of pattern separation.

MATERIALS AND METHODS

Preparation of brain slices, electrophysiological analysis of intrinsic properties and outward K^+ currents, RNA extraction and quantitative real-time PCR (qRT-PCR), and behavioral tests for fear discrimination were performed with the same methods described in Chapter 1. Data analysis methods were same as described in Chapter 1.

1. Cytosolic Ca^{2+} measurement from slices.

Cytosolic $[Ca^{2+}]$ was measured from fluorescence images of a hippocampal granule cells (GCs) in the slice loaded with fura-2 (pentapotassium salt) via a whole-cell patch pipette. For fluorescence excitation, I used a polychromatic light source (xenon-lamp based, Polychrome-urce (xenon-lamp baMartinsried, Germany), which was coupled into the epi-illumination port of an upright (for slices; BX51, Olympus, Japan) via a quartz light guide and an UV condenser. For slices, the imaging of GCs was performed with a 60X water immersion objective (NA 0.9, LUMPlanFl, Olympus) and an air-cooled slow-scan CCD camera (SensiCam, PCO, Kelheim, Germany).

The monochromator and the CCD camera were controlled by a

PC and ITC18, running a custom-made software programmed with Microsoft Visual C++ (version 6.0; CCDLabo1.0, www.cellphysiology.org).

Calibration parameters were determined using *in cell* calibration. The ratio $R = F_{\text{iso}} / F_{380}$ was converted to $[\text{Ca}^{2+}]$ values using equation

$$[\text{Ca}^{2+}] = K_{\text{eff}} \cdot (R - R_{\text{min}}) / (R_{\text{max}} - R). \quad (1)$$

The values for calibration ratio at intermediate $[\text{Ca}^{2+}]_i$ were measured using a pipette solution containing 10 mM BAPTA and 10 mM CaCl_2 ($[\text{Ca}^{2+}]_i \approx 231$ nM). The estimated R_{min} , R_{max} , and K_{eff} in somata measured using the upright microscope were typically 0.88, 5.72, and 1.03, respectively (in μM). The effective dissociation constant of fura-2 (K_{eff}) was calculated by measuring the fluorescence ratio at these intermediate $[\text{Ca}^{2+}]_i$ and by re-arranging Equation 1 for K_{eff} . The K_d of fura-2 was calculated as 158 nM from

$$K_d = K_{\text{eff}} \cdot (\alpha + R_{\text{min}}) / (\alpha + R_{\text{max}}) \quad (2)$$

, where α is an isocoefficient.

To increase the time resolution and minimizing the photobleaching effect, I adopted the single-wavelength protocol in the Ca^{2+} -imaging of the slices (Helmchen et al., 1996; Lee

et al., 2000). Images taken at 20 Hz with single wavelength excitation at 380 nm (F_{380}) were preceded and followed by images with excitation at isosbestic wavelengths (360 nm). F_{iso} (isosbestic fluorescence) values were linearly interpolated between points just before and after the period of excitation at 380 nm.

2. Estimation of calcium binding ratios in DG–GCs

To estimate the Endogenous Ca^{2+} binding ratio, I applied short depolarizing pulses (from -70 mV to 0 mV, 50 ms in duration) every $20 - 60$ s in order to evoke $[Ca^{2+}]$ transients in the mature DG–GCs. F_{380} images at 20 Hz were taken. Furthermore, these images were preceded and followed by double wavelength image pairs, so that the Ca^{2+} concentration could be calculated as described in the previous section. Because calcium transients were largely abolished by the addition of 1 μ M TTX to the bath solution (data not shown), these dendritic transients are most probably evoked by back–propagating action potentials, which may be generated by the mechanism of voltage escape.

During off–line analysis, F_{iso} was calculated, and the

time course of F_{iso} was regarded as the loading curve of fura-2. The concentration of fura-2 in dendrites was estimated assuming that the F_{iso} at the plateau of the loading curve represents full loading of fura-2. In cases where the F_{iso} measured in a region of interest (ROI) set at a large distance from the soma did not plateau, an exponential fit of the loading curve was extrapolated to infinity and regarded as the value of F_{iso} in the fully loaded state.

When two kinds of Ca^{2+} buffer, Ca^{2+} -indicator dye (B) and endogenous Ca^{2+} buffer (S), exist in the compartment, increments of total and free calcium have the following relationship:

$$\Delta[\text{Ca}^{2+}]_{\text{T}} = \Delta[\text{Ca}^{2+}]_{\text{i}} \cdot (1 + \kappa_{\text{B}} + \kappa_{\text{S}}) \quad (3)$$

, where κ_{B} and κ_{S} are calcium binding ratios of B and S, respectively. Calcium binding ratio of a buffer, X, is defined by

$$\kappa_{\text{X}} = \partial[\text{CaX}] / \partial[\text{Ca}^{2+}] = K_{\text{d}} \cdot X_{\text{T}} / ([\text{Ca}^{2+}] + K_{\text{d}})^2 \quad (4)$$

, where X_{T} and K_{d} are total concentration of X and the dissociation constant of X for Ca^{2+} , respectively (Neher and Augustine, 1992). When κ_{X} is not constant over the dynamic range of $[\text{Ca}^{2+}]$ in a Ca^{2+} transient, incremental Ca^{2+} -binding ratio, κ'_{X} , should be used, which is defined as

$$\kappa'_X = \Delta[\text{CaX}] / \Delta[\text{Ca}^{2+}] = K_d \cdot X_T / [([\text{Ca}^{2+}]_{i,\text{rest}} + K_d) \cdot ([\text{Ca}^{2+}]_{i,\text{peak}} + K_d)] \quad (5)$$

RESULTS

Endogenous calcium binding ratios (κ_E) is reduced in mature dentate granule cell of Alzheimer's disease model mice (Tg2576)

Previous reports demonstrated Alzheimer's disease (AD) lymphoblasts have a lower Ca^{2+} buffering capacity than normal cells, probably because of changes in availability or intrinsic functional properties of the intracellular Ca^{2+} -binding structures (Ibarreta et al., 1997). Palop groups reported calbindin- $\text{D}_{28\text{K}}$ (CB) levels were reduced in the dentate gyrus granule cell (DG-GCs) both in AD model mouse and human with AD (Palop et al., 2003). In most previous studies, changes in CB level were shown in protein or mRNA levels, but functional analysis for the changes in cellular buffer capacity has never been performed.

To quantify Ca^{2+} buffer capacity in DG-GCs from 1- to 2-month-old mice, I estimated κ_E (the sum of the Ca^{2+} binding ratio of mobile and static endogenous Ca^{2+} buffers) in mature DG-GCs using a method used in the previous papers

(Lee et al., 2009). I loaded the DG-GCs with fura-2 (250 μM) with whole-cell patch pipettes ($R_s = 20.5 \pm 1.0 \text{ M}\Omega$), and evoked Ca^{2+} transients (CaTs) by applying voltage pulses (from -70 mV to 0 mV , 40 ms duration) at different time points of the fura-2 loading. As the cytosolic fura-2 concentration increased gradually after patch break-in (upper panel, Fig. 1A), amplitudes of CaTs (A) decreased while time constants of CaTs (τ) increased (exemplary CaTs obtained at the time points indicated by number: lower panel, Fig. 1A). I plotted τ against the Ca^{2+} binding ratio of fura-2 (κ_B) which was calculated from the equation (5), and estimated the κ_E from the x -intercept from the extrapolation of the linear fit (Fig. 1B). The mean κ_E value estimated from the τ vs κ_B plots was 340.6 ± 12.4 ($n = 10$) in the WT DG-GCs, which is not different from the value obtained previously from mature DG-GCs in C57BL/6 mice (Lee et al., 2009), and it was significantly lower in the Tg2576 DG-GCs (206.7 ± 4.6 , $n = 7$, $p < 0.001$). The κ_E values could also be estimated from the A^{-1} vs κ_B plots, and the results (open bars, Fig. 1C) were not significantly different from the values estimated from the τ vs κ_B plots (filled bars, Fig. 1C). Notably, the κ_E value estimated in the

Tg2576 DG-GCs is comparable to that in CBKO DG-GCs reported previously (210.9 ± 4.8), where CB is completely abolished (Lee et al., 2009).

A β is believed to be the most important pathogenic factor in AD. Among various species of A β , A β_{1-40} is most abundant and A β_{1-42} is most toxic (Mucke et al., 2000; Walsh and Selkoe, 2007). Previous study reported that the level of A β_{1-42} in the DG from Tg2576 was higher compared with that in other regions of the hippocampus [Hippo(-DG)] (DG; 0.3 ± 0.001 ng/ml, DG(-), 0.1 ± 0.01 ng/ml, (Lee et al., 2012)). I tested the possibility that A β may underlie the impaired Ca²⁺ buffering in Tg2576 DG-GCs by investigating the effect of exogenous applications of A β_{1-42} . When hippocampal slices obtained from WT mice were incubated for 1 hr with oligomeric A β_{1-42} (1 μ M), one of the most toxic species among amyloid β proteins (Mucke et al., 2000), the κ_E in DG-GCs was significantly reduced to a value (black, 212.8 ± 31.5 , n = 3) comparable to the κ_E estimated in Tg2576 DG-GCs (red, Fig. 1C). This result supports the idea that overproduced A β_{1-42} in Tg2576 DG-GCs could induce CB dysfunction.

Increased excitability in DG–GCs of Tg2576

Reduced Ca^{2+} buffering should affect Ca^{2+} homeostasis of the cell, which in turn may cause various cellular changes. In spite, it has never been shown whether reduced Ca^{2+} buffering is causally related with any specific change. It is well known in cardiac myocytes that Ca^{2+} overload causes ion channel remodeling and abnormal action potentials (APs) (Brundel et al., 2001; Ohashi et al., 2004). I tested the possibility that Ca^{2+} dysregulation caused by reduced Ca^{2+} buffering could alter neuronal excitability. Interestingly, I found that the firing frequency in response to long depolarizing pulses was significantly higher in the Tg2576 DG–GCs (red, Fig. 2A) compared to the WT DG–GCs (blue, Fig. 2A). I conducted experiments using only mature DG–GCs which exhibit typical electrophysiological properties, such as low input resistance (R_{in}), hyperpolarized resting membrane potential and high threshold current for an action potential (Lee et al., 2009; Schmidt–Hieber et al., 2004). As a measure of neuronal excitability, I plotted firing frequencies (F) against the amplitude of injected currents (I), and found that F–I curve shifted upward in Tg2576 (red, Fig. 2Ab) compared with WT

(blue, Fig. 2Ab). Hyperexcitability phenotype in Tg2576 mice appeared to be specific to DG-GCs, because F-I curves obtained from CA1 pyramidal cells (CA1-PCs) did not show significant difference between WT and Tg2576 mice (at 100 pA, WT, 22.25 ± 5.793 , $n = 4$; Tg2576, 25.25 ± 3.944 , $n = 4$, $p > 0.05$, Fig. 2D). These results may indicate that abnormal Ca^{2+} homeostasis caused by reduced Ca^{2+} buffering results in electrical remodeling in DG-GCs that induces hyperexcitability. Since passive electrical properties, such as resting membrane potential (RMP), input resistance, rheobase, were not significantly different between WT and Tg2576 (Fig. 2C), it was suggested that not the ion channels active at subthreshold range but those activated during action potentials are subject to be altered in DG-GCs of Tg2576.

Sustained component in 4-AP sensitive currents is reduced in Tg2576 DG-GCs.

To investigate the ion channel mechanism responsible for hyperexcitability in DG-GCs of Tg2576 mice, I tested a possibility of suppression of voltage-dependent K^+ currents. I recorded whole-cell K^+ currents in the voltage clamp mode by

depolarization ranging from -60 mV to $+30$ mV (in $+10$ mV increments, 1 s duration) from a holding potential of -70 mV. The TTX, $\text{Cd}^{2+}/\text{Ni}^{2+}$, bicuculline, and CNQX were added to the external solution to block Na^+ channels, Ca^{2+} channels, GABA_A receptors, and AMPA/Kainate receptors, respectively. Under these conditions, there was no significant difference in total K^+ currents between the WT and Tg2576 DG-GCs (Fig. 3B). Thus, I dissected them into TEA-sensitive K^+ currents (I_{TEA}) and 4-AP sensitive K^+ currents by subtracting the currents in the presence of blocker from the control (Fig. 3A). Although TEA and 4-AP are not considered as specific blockers, it is generally believed that TEA is more sensitive to delayed rectifiers, while low ($40 \mu\text{M}$) and high (5 mM) concentrations of 4-AP selectively block D-type (I_{D}) and A-type (I_{A}) K^+ currents, respectively (Beck et al., 1997; Riazanski et al., 2001; Storm, 1988) The results showed that I_{TEA} (Fig. 4A) I_{D} (Fig. 4B) were indistinguishable between WT and Tg2576 DG-GCs (I_{TEA} , peak current (I_{peak}) at $+30$ mV WT; 2.2 ± 0.19 nA, $n = 4$, Tg2576; 2.23 ± 0.31 nA, $n = 3$; I_{D} , I_{peak} at $+20$ mV, WT; 0.609 ± 0.117 nA, $n = 5$, Tg2576; 0.688 ± 0.086 nA, $n = 6$, $P > 0.05$), whereas 5 mM 4-AP sensitive K^+ currents ($I_{4\text{-AP}}$) in

Tg2576 DG-GCs were significantly reduced compared to those in WT DG-GCs (Fig. 5). I_A are usually characterized by rapid inactivation kinetics, but in WT DG-GCs, a significant proportion of I_{4-AP} did not inactivate even after 1 s, showing the sustained current (I_{sus}) in I_{4-AP} ($I_{sus}/I_{peak} = 32.24\%$ at +30 mV). The amplitude of the sustained I_{4-AP} measured at +30 mV was 470 ± 40 pA ($n = 12$) in the WT, which is about 22.4% of the I_{peak} . In Tg2576 DG-GCs, I_{sus} was reduced significantly in Tg2576 DG-GCs (0.192 ± 0.035 nA, $n = 8$, at +30 mV) compared with WT DG-GCs (Fig. 5Ab). I_{peak} was also reduced in Tg2576 (at +30 mV; WT, 2.45 ± 0.142 nA, $n = 8$; Tg2576, 1.62 ± 0.196 nA, $n = 8$; Fig. 5Ab).

For better demonstration of the difference between WT and Tg2576, I superimposed the current traces obtained at +30 mV (Fig. 5Ba). I found that the current traces obtained at +30 mV fit well with the two-exponential decay function: $I(t) = A_{fast} \exp(-t/\tau_{fast}) + A_{slow} \exp(-t/\tau_{slow})$. The values for each parameter obtained from the WT and Tg2576 (Fig. 5Bb). The amplitude of the slow component (A_{slow}) was selectively reduced in the Tg2576 DG-GCs compared to the WT DG-GCs, whereas the other parameters (A_{fast} , τ_{fast} , and τ_{slow}) did not

show significant differences among the three groups. These findings suggest that a large proportion of sustained component is a characteristic feature of I_A in DG-GCs and that this component is preferentially suppressed in Tg2576 DG-GCs.

I showed in the first chapter that sustained component of I_{4-AP} in DG-GCs is mediated by Kv4.1 subunits, and that expression of Kv4.1 subunits are reduced in CBKO mice. I therefore hypothesized as a mechanism for the reduction of sustained I_{4-AP} in Tg2576 DG-GCs that dysregulated Ca^{2+} homeostasis caused by reduced Ca^{2+} buffering induces downregulation of Kv4.1 expression. To examine this idea, I performed a quantitative Real-Time PCR (qRT-PCR) technique to examine expression of Kv4 family channels in DG of WT and Tg2576 (Fig. 5C). The result shows that Kv4.1 mRNA expression is significantly decreased in Tg2576 DG, whereas Kv4.2 and Kv4.3 mRNA expression is not altered. These results strongly suggest that selective downregulation of Kv4.1 expression in DG of Tg2576, without being compensated by other Kv4 family channels, may underlie reduced sustained I_{4-AP} in Tg2576 DG-GCs.

Impaired Ca^{2+} buffering and hyperexcitability of Tg2576 DG-GCs are restored by antioxidant treatment

The next question is the mechanism to induce the impairment of Ca^{2+} buffering in Tg2576 DG-GCs. CB has two N-terminal cysteine residues that undergo redox-driven structural changes, and it was shown that oxidized CB has a lower Ca^{2+} binding affinity than that of reduced CB (Cedervall et al., 2005). I showed previously that mitochondrial reactive oxygen species (ROS) production is increased in the DG-GCs of 1- to 2-month-old Tg2576 mice (Lee et al., 2012). Thus, it is likely that oxidative stress may induce oxidation of CB to compromise the Ca^{2+} buffering capacity. To test this possibility, I examined if the reduced κ_E in the Tg2576 DG-GCs is restored by antioxidant treatment. When hippocampal slices obtained from Tg2576 mice were incubated in Trolox (500 μM) for 1 hr, the κ_E value was 322.9 ± 30.2 (Figs. 6Aa and 6Ad), which was comparable to the κ_E value of WT DG-GCs. To ensure whether the effect of Trolox on κ_E in the Tg2576 DG-GCs is indeed attributable to protection of CB from oxidation, I further evaluated the effect of Trolox on κ_E in the CB knockout (CBKO) DG-GCs. When hippocampal slices obtained from the

CBKO mice were incubated with Trolox for 1 hr, the κ_E in DG-GCs was 216.8 ± 1.1 (black, Fig. 6Ab and 6Ad), which was not significantly different from the κ_E value reported previously for CBKO DG-GCs under control conditions (210.9 ± 4.8) (Lee et al., 2009). This result further supports the idea that the effect of Trolox on restoring Ca^{2+} buffering in the Tg2576 DG-GCs is mediated by protection of CB from oxidation.

To provide further evidence that the hyperexcitability phenotype in the Tg2576 DG-GCs is a consequence of reduced Ca^{2+} buffering, I estimated whether the hyperexcitability phenotype in the Tg2576 GCs is restored by Trolox. When the brain slices of Tg2576 mice were treated with Trolox for 1 hr, hyperexcitability of the Tg2576 GCs was not restored (black, Fig. 6B). However, hyperexcitability of the Tg2576 GCs was completely restored to the normal level when Tg2576 mice received intraperitoneal (i.p.) injections of Trolox (20 mg/Kg) once a day for one week (skyblue, Fig. 6B). The Trolox treatment of Tg2576 mice did not affect the passive electrical properties of the DG-GCs, such as the RMP, rheobase, and input resistance (Table. 1). These results are consistent with

the idea that ion channel remodeling responsible for the increased excitability in Tg2576 DG-GCs is not an immediate consequence of Ca^{2+} overload, but that the expression levels of ion channels are slowly altered under the Ca^{2+} dysregulated conditions. I also analyzed the $I_{4\text{-AP}}$ currents and confirmed that the reduction of sustained $I_{4\text{-AP}}$ in the Tg2576 DG-GCs was also completely restored by the Trolox treatment for 1 week (Fig. 6C). These results suggest a causal relationship between impairment of CB functions by $A\beta$ -induced oxidative stress, Kv4.1 reduction, and the hyperexcitability of DG-GCs.

Impaired pattern separation in Tg2576 mice are restored by Trolox

Considering that the excitability of DG is specifically important for pattern separation (Jinde et al., 2012), the pathophysiological significance of the hyperexcitability of Tg2576 DG-GCs with respect to cognitive deficits has not been investigated. The low excitability of the DG is thought to be important for pattern separation in the hippocampus (O'Reilly and McClelland, 1994). Recently, Tonegawa group reported an early stage of AD model mice, before amyloid plaque deposition,

showed impairment in the memory retrieval by activating DG engram cells (Roy et al., 2016). I investigated whether increased firing frequency of DG-GCs in Tg2576 mice leads to impairments in discriminating similar contexts by using a contextual fear discrimination test. I subjected the Tg2576 mice to contextual fear conditioning using a similar pair of contexts (A and B) that shared an identical metal grid floor, although context B had unique an odor (1% acetic acid), dimmer lighting (50% of A), and a sloped floor (15° angle). As shown in Fig. 7A, mice learned to discriminate between the similar contexts over several days. WT and Tg2576 group showed similar freezing levels during the 5 min test in context A (Fig. 7Ba) and equivalent generalization between contexts (Fig. 7Bb, WT, Tg2576, two-way ANOVA, genotype: $F_{(1,30)} = 0.24$, $p = 0.62$, context: $F_{(1,30)} = 0.15$, $p = 0.70$, genotype \times context: $F_{(1,30)} = 0.39$, $p = 0.54$). The mice were subsequently trained to disambiguate these contexts by visiting both contexts daily for 8 days with a 2 hr interval between contexts (from day 6 to day 13), always receiving a foot shock 180 s after being placed in context A but not in context B. A daily discrimination ratio was calculated by determining the ratio of freezing during the

180 s in context A to total freezing during the two visits (A and B). On day 6, both genotypes could not distinguish differences between the contexts (Fig. 7Cb, genotype: $F_{(1,24)} = 3.67$, $p = 0.06$, context: $F_{(1,24)} = 0.73$, $p = 0.40$, genotype \times context: $F_{(1,24)} = 0.31$, $p = 0.58$); thus, the discrimination ratio was approximately 0.5. As the experiment progressed, WT mice began to discriminate context B from context A, and the discrimination ratio was increased. However, Tg2576 mice exhibited significant deficits in the acquisition of discrimination ability (Fig. 7Ca), and showed increased freezing in the shock-free context (Fig. 7Cb, t-test, Context B, $p < 0.0001$, Two-way ANOVA, genotype: $F_{(1,25)} = 0.25$, $p = 0.62$, context: $F_{(1,25)} = 19.19$, $p < 0.0001$, genotype \times context: $F_{(1,25)} = 34.63$, $p < 0.000004$). To examine whether impaired discrimination between similar contexts in Tg2576 mice was due to impaired general memory acquisition, I examined the context specificity of the conditioning by assessing freezing behavior using a distinct pair of contexts (A and C). This distinct context (context C) evoked significantly lower levels of freezing (similar in both genotypes) than context A (Fig. 7D, genotype: $F_{(1,14)} = 0.16$, $p = 0.70$, context: $F_{(1,14)} = 43.78$, $p < 0.000012$,

genotype \times context: $F_{(1,11)} = 0.06$, $p = 0.80$). These data imply Tg2576 mice experienced no deficits in learning or discriminating between very distinct contexts, but showed impairments with similar contexts (pattern separation). These results indicate that Tg2576 mice exhibited specific impairment in pattern separation between similar contexts without deficits in memory acquisition. I showed in Fig. 6 that the reduced Ca^{2+} buffering and hyperexcitability in the Tg2576 DG-GCs is restored by antioxidant treatment. If the hyperexcitability phenotype in the Tg2576 DG-GCs is restored by treatment with antioxidants, deficit of pattern separation in Tg2576 mice should also be restored. Tg2576 mice received i.p. injections of Trolox (20 mg/Kg) once a day for one week. Then I did a same experiment using Trolox treatment of Tg2576 mice. Interestingly, Trolox treatment of Tg2576 mice exhibited significantly increased in the acquisition of discrimination ability (Fig. 7Ca, skyblue), and showed increased freezing in the shock context (Fig. 7Cb, t-test, Tg2576, Tg2576 + Trolox (i.p.), Context A, $p < 0.02$, Two-way ANOVA, Treatment: $F_{(1,29)} = 0.20$, $p = 0.65$, context: $F_{(1,29)} = 1.14$, Treatment \times context: $F_{(1,29)} = 9.76$, $p = 0.004$). The acquisition of discrimination

ability were comparable to those observed in WT mice. These results support the pattern separation in hippocampus depends on the excitability of DG-GCs and is impaired in the early preclinical stage of AD.

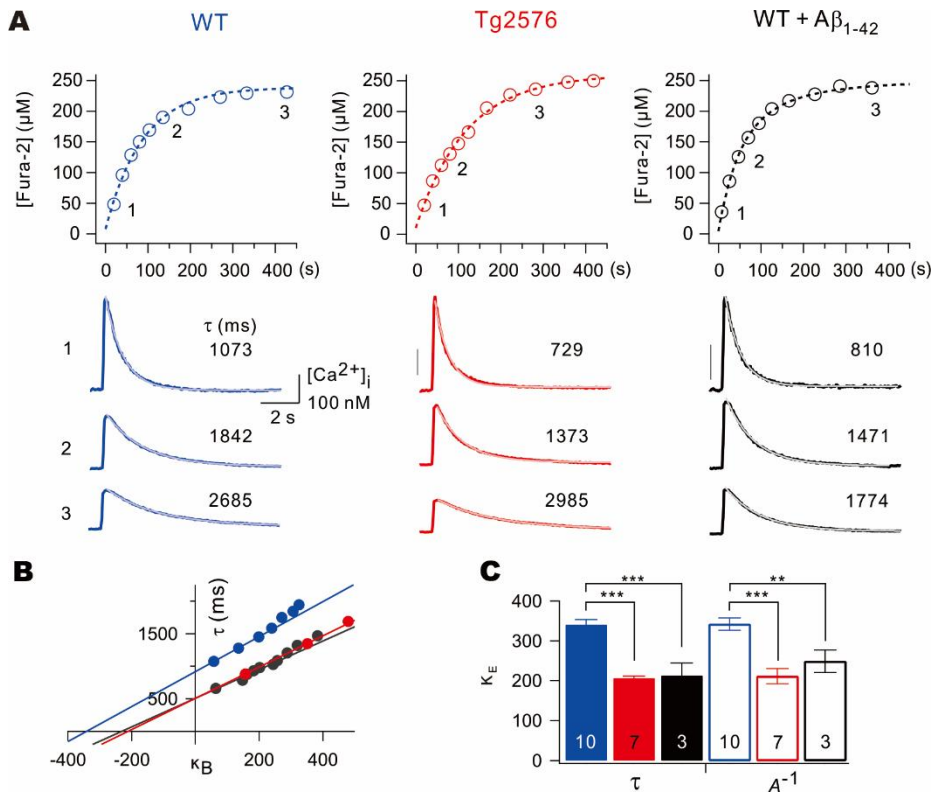


Figure 1. Estimation of endogenous Ca $^{2+}$ binding ratios (κ_E) in WT and Tg2576 DG-GCs

Ca $^{2+}$ transients (CaTs) were evoked by depolarizing pulse (from -70 mV to 0 mV, 50 ms in duration) with 250 μM fura-2 internal in the soma of granule cell (GC) of the hippocampal dentate gyrus (DG) from Wild-type (WT, blue), Tg2576 (red) and exogenous application of A β_{1-42} in WT DG-GCs (black). (A) Fura-2 loading curve was obtained from the plot of isosbestic fluorescence as a function of whole-cell recording

time. WT inset, representative CaTs after break-in (20 s, 135 s, and 427 s). Tg2576 inset, representative CaTs after break-in (40 s, 124 s, and 282 s). WT + $A\beta_{1-42}$ inset, representative CaTs after break-in (7 s, 95 s, and 361 s). (B) Time constants (τ) estimated from mono-exponential fits to the decay phases of CaTs are plotted as a function of Ca^{2+} binding ratios of fura-2 (κ_B). An x -axis intercept of the linear fit to this plot was considered as endogenous Ca^{2+} binding ratios (κ_E). (C) Mean values for κ_E from WT, Tg2576 and WT + $A\beta_{1-42}$ DG-GCs estimated from the plots of τ (solid bars) and A^{-1} (open bars) as a function of κ_B . Numbers on the bar graph indicate the number of cells used in the experiments. Error bars indicates SEM. Values indicate mean \pm SEM.

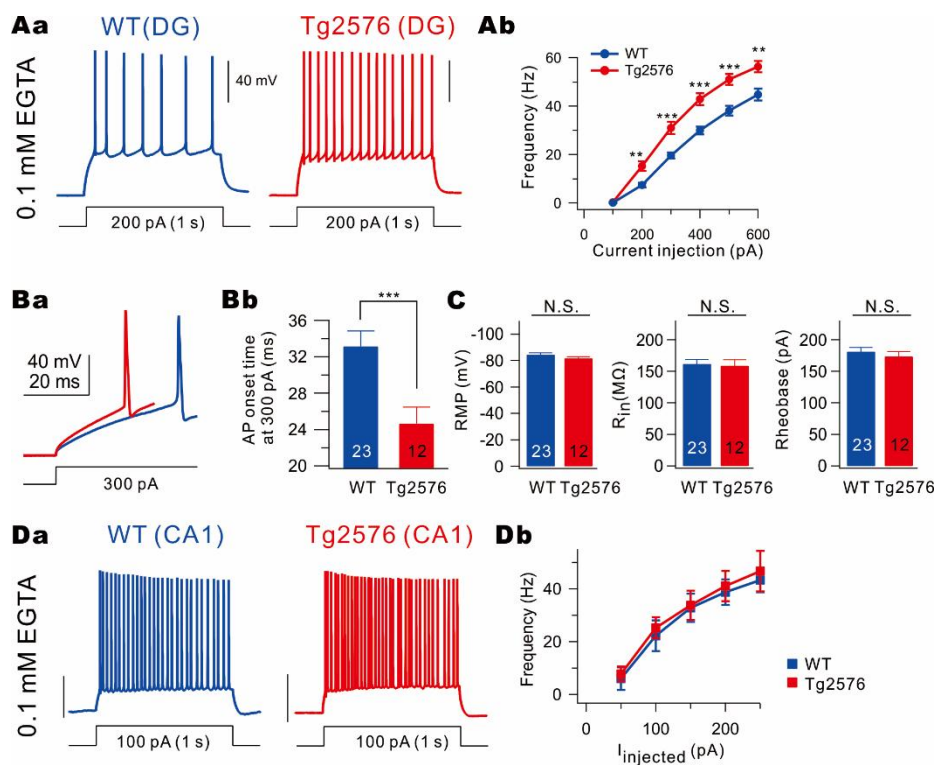


Figure 2. Hyperexcitability of DG-GCs in Tg2576

(Aa) Representative trace in the current-clamp recording from WT (blue) and Tg2576 (red) DG-GCs in response to prolonged (1 s) depolarizing current injection (200 pA). (Ab) Number of spikes (F) evoked during 1 s current injections (I) is plotted as a function of varying amplitudes (from 100 pA to 600pA, +100 pA increment) of the current injection. At all amplitudes, the Mean \pm SEM. Number of spikes is significantly higher in Tg2576 (n = 14, green closed circle) than WT DG-GCs (n = 15, black closed circle), *, (Ba) superimposed and

expanded view of the 1st AP traces obtained at 300 pA current injection. Inset scale bars indicate 40 mV and 20 ms. (Bb) The mean values of 1st AP onset time from WT (blue) and Tg2576 (red) DG-GCs. (C) The mean values of RMP, input resistance (R_{in}), rheobase from WT (blue) and Tg2576 (red) DG-GCs. (Da) Representative trace in the current-clamp recording from WT (blue) and Tg2576 (red) CA1-PCs in response to prolonged (1 s) depolarizing current injection (100 pA). (Db) the F-I curve in WT (n = 4, red closed square) and Tg2576 (n = 4, green closed square) CA1-PCs. Scale bar indicate 40 mV and 300 ms. Error bars indicates SEM. Values indicate mean \pm SEM. n, the number of cell tested. N.S., not significantly different, $P > 0.05$.

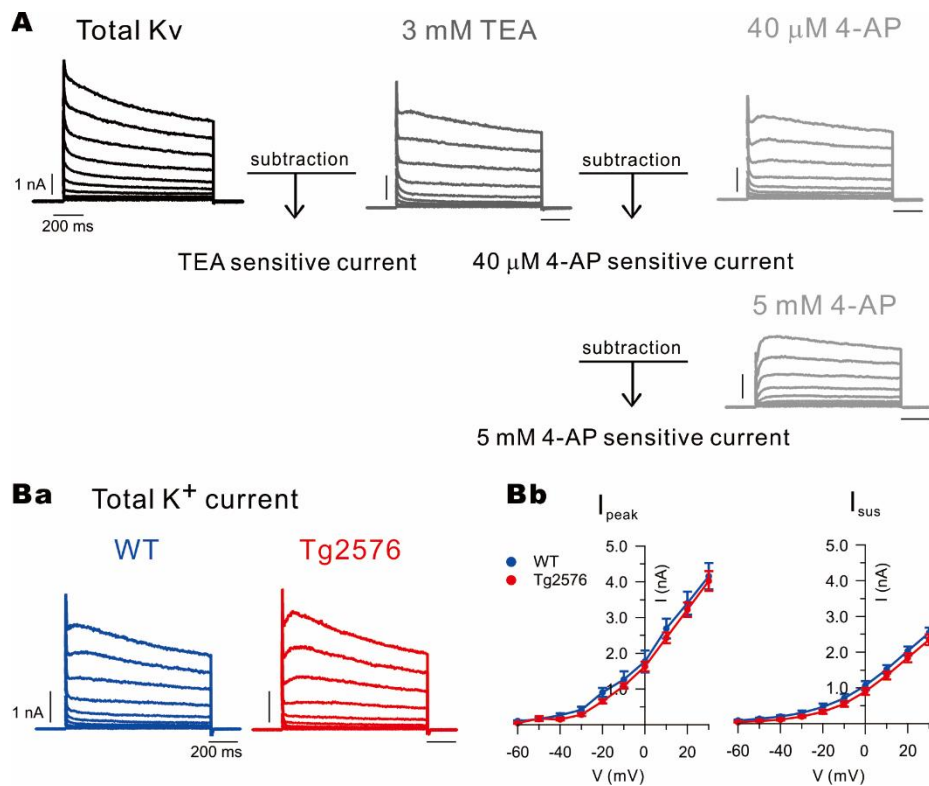


Figure 3. K^+ current measurements in DG-GCs

(A) Representative whole-cell, voltage-gated K^+ currents from WT DG-GCs. Currents were evoked in response to 1 s voltage steps to potentials between -60 mV to $+30$ mV from a holding potential of -70 mV. After recording the control (black), I changed the bath solution which contained 3 mM TEA (dark gray). 3 mM TEA blocked slow inactivated K^+ currents. The difference between the control and 3 mM TEA called TEA-sensitive currents (I_{TEA}). To measure the D-type and A-type

K⁺ currents, I applied 40 μM 4-AP to the bath solution to block the D-type K⁺ channel. To isolate the A-type K⁺ current, the bath solution was changed to contain 5 mM 4-AP to block the A-type K⁺ channel. (Ba) Representative whole-cell, voltage-gated total K⁺ currents recorded from WT (blue) and Tg2576 (red) DG-GCs. (Bb) Total I-V curve, current amplitude of peak (I_{peak}) and sustained (I_{sus}) are plotted as a function of given potential (V), WT (n = 9, black closed circle) and Tg2576 (n = 9, green closed circle). Error bars indicates SEM. Values indicate mean ± SEM.

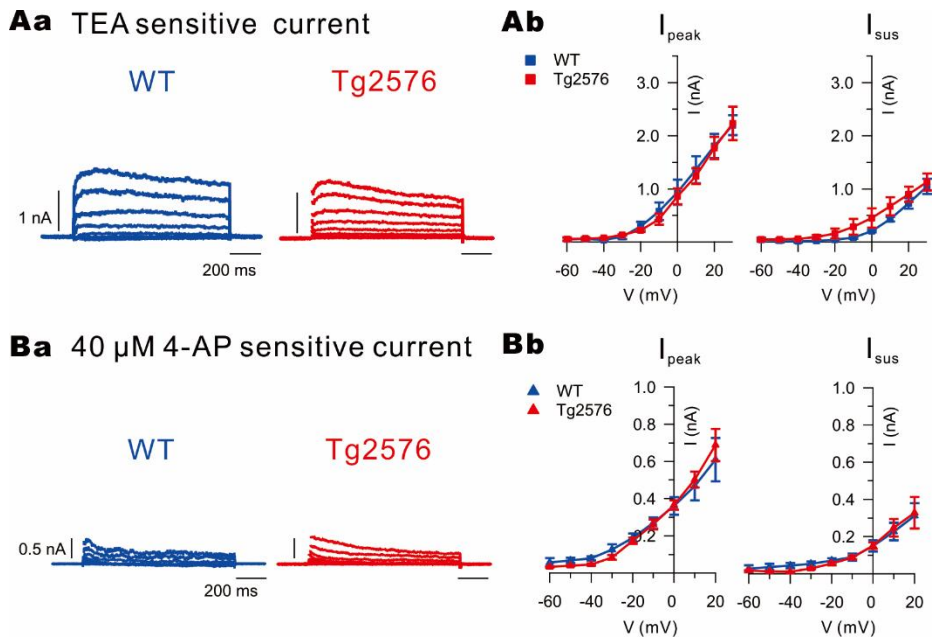


Figure 4. TEA and 40 μ M 4-AP sensitive K^+ current in WT and Tg2576 DG-GCs

(Aa) Representative I_{TEA} of WT (blue) and Tg2576 (red) DG-GCs. Scale bar indicate 1 nA and 200 ms. (Ab) TEA-sensitive I-V curve, I_{peak} and I_{sus} are plotted as a function of given potential (V), WT (n = 4, blue square) and Tg2576 (n = 3, red square). (Ba) Representative 40 μ M 4-AP sensitive K^+ current of WT (blue) and Tg2576 (red) DG-GCs. Scale bar indicate 0.5 nA and 200 ms. (Bb) 40 μ M 4-AP sensitive I-V curve, I_{peak} and I_{sus} are plotted as a function of given potential (V), WT (n = 5, blue triangle), Tg2576 (n = 6, red triangle). Scale bar

indicate 0.5 nA and 200 ms. n, the number of cell tested. Error bars indicates SEM. Values indicate mean \pm SEM.

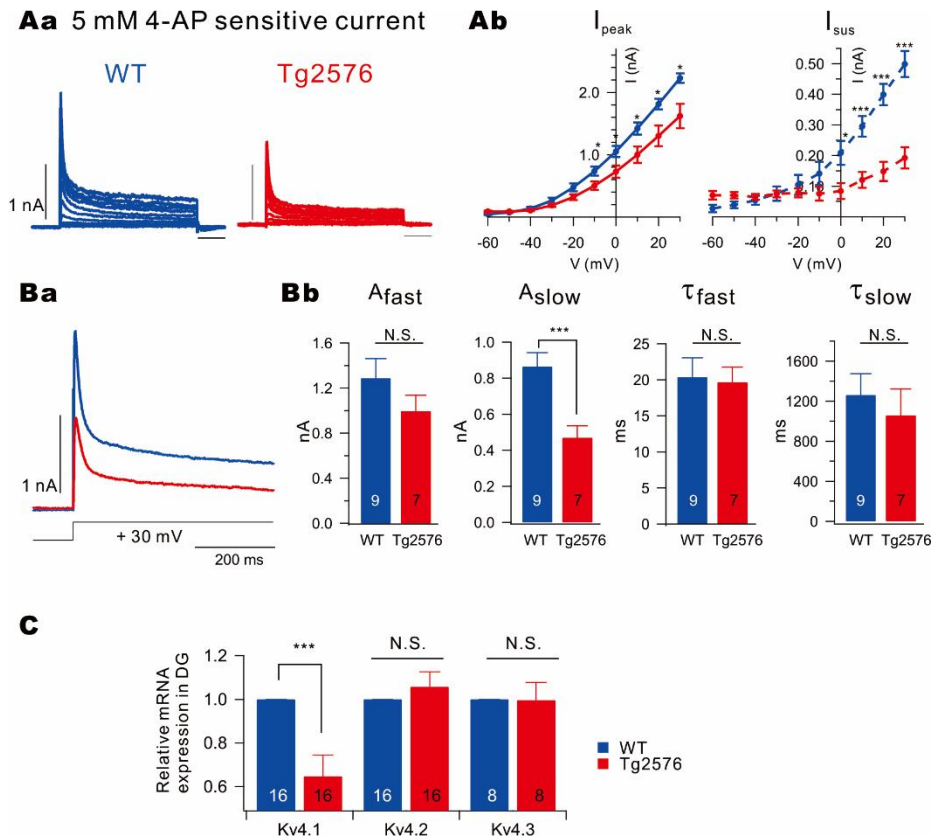


Figure 5. Reduced sustained component of 5 mM 4-AP sensitive current in Tg2576 DG-GCs

(Aa) Representative trace of 5 mM 4-AP sensitive current (I_{4-AP}) from WT (blue) and Tg2576 (red) DG-GCs. (Ab) 5 mM 4-AP sensitive peak current amplitude (I_{peak} , left) and sustained current amplitude (I_{sus} , right) in WT ($n = 8$, black closed circle) and Tg2576 ($n = 8$, green closed circle) are plotted as a function of given potential. Bar indicate 1 nA and 200 ms. (Ba) Superimposed and expanded view of the I_{4-AP} obtained at +30

mV depolarization. (Bb) 5 mM 4-AP-sensitive currents recorded at +30 mV were fitted to double-exponential functions. Amplitude and time constant for the fast component (A_{fast} , τ_{fast}) and the slow component (A_{slow} , τ_{slow}). (C) Relative mRNA levels for 3 different Kv4 channel family normalized to GAPDH, comparing WT (blue) and Tg2576 (green). Numbers on the bar graph indicate the number of cells used in the experiments. Error bars indicates SEM. Values indicate mean \pm SEM.

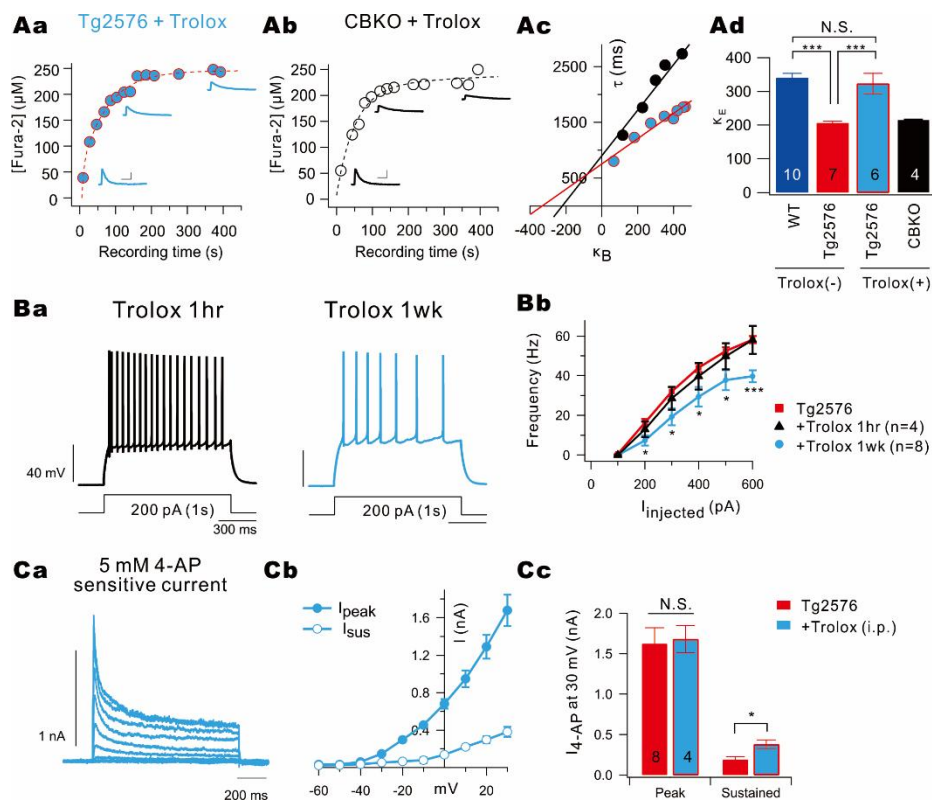
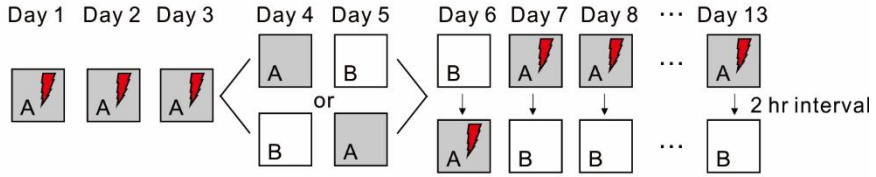


Figure 6. Effects of pre-treatment with Trolox in the Tg2576 and CBKO mice

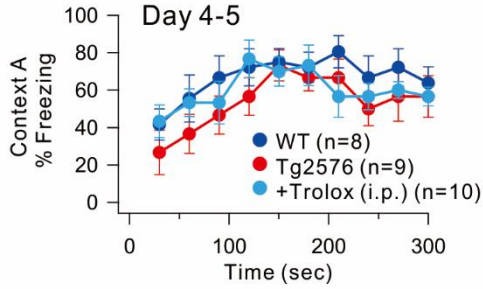
Brain slices from Tg2576 (red, Aa) and CBKO (black, Ab) were treated with Trolox (500 μM) for 1 hr before recordings at 34°C. Fura-2 loading curves (Aa and Ab) and plots of τ (Ac) against κ_B were obtained as described in Figure 1. Inset scale bars indicate 100 nM [Ca²⁺]_i and 2 s. (Ad) The mean values of κ_E estimated from the plots of τ as a function of κ_B . Data for WT, Tg2576 (same results shown in Fig. 1) are presented for

comparison. (B) Representative trace in the current-clamp recording of Tg2576 DG-GCs in response to depolarizing current (200 pA, 1 s) injection (Ba) and F-I curves (Bb). Trolox was treated to the brain slices for 1 hr (left, black) or injected intraperitoneally (i.p.) once a day for one week (right, skyblue). (Ca) Superimposed current traces for I_{4-AP} obtained from -60 mV to +30 mV (Tg2576 + Trolox (i.p.), skyblue). (Cb) 5 mM 4-AP sensitive I_{peak} (filled) and I_{sus} (open) in Tg2576 + Trolox (i.p.) (skyblue, n = 4) are plotted as a function of given potential. (Cc) The summary bar graph of I_{4-AP} at +30 mV. Numbers on the bar graph indicate the number of cells used in the experiments. Error bars indicates SEM. Values indicate mean \pm SEM.

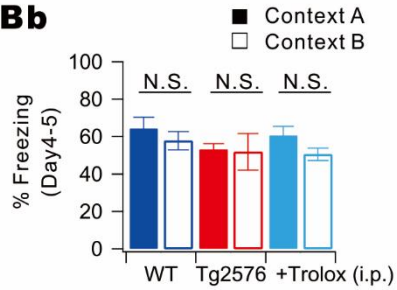
A Pattern separation



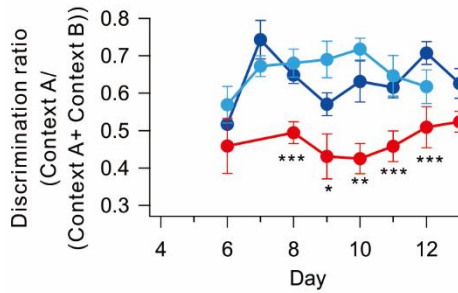
Ba



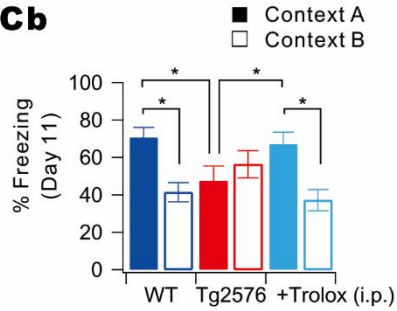
Bb



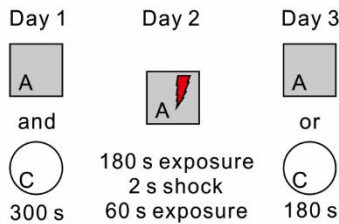
Ca



Cb



Da



Db

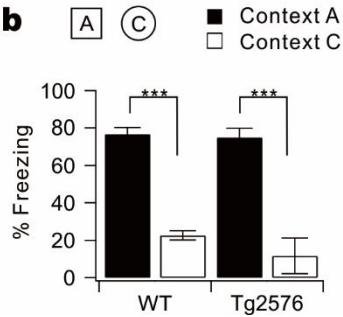


Figure 7. Impaired pattern separation in Tg2576 mice restored by Trolox.

(A) Experimental procedure for pattern separation in 14- to 16-week-old WT (n = 8), Tg2576 (n = 9) and Trolox treatment of Tg2576 (i.p.) (n = 10) mice. (Ba) On day 4 to 5, the kinetics of freezing across the 5 min test in context A. (Bb) The percentage of freezing in A (filled bar) and B (open bar) during day 4 to 5 in both contexts (A and B). WT (blue, n = 8), Tg2576 (red, n = 9), and Tg2576 + Trolox (i.p.) (n = 10) mice displayed equal amounts of freezing in both contexts (A and B). (Ca) On day 6 to 13, time course of the discrimination ratio in WT (blue, n = 8), Tg2576 (red, n = 9), and Tg2576 + Trolox (i.p.) (n = 10) mice. (Cb) The percentage of freezing in context A (filled bar) and context B (open bar) for the WT (blue, n = 8), Tg2576 (red, n = 9), and Tg2576 + Trolox (i.p.) (n = 10) mice on day 11. (Da) Experimental procedure for one-trial contextual fear conditioning between 24 and 28 weeks of age in WT (n = 8) and Tg2576 (n = 8) mice (Db) The percentage of freezing in context A (filled bar) and context C (open bar, distinct object) for the WT (n = 8) and Tg2576 (n = 8) mice. Error bars indicates SEM. Values indicate mean \pm SEM.

Resting Membrane Potential (mV)			Input resistance (M Ω)			Rheobase (pA)		
WT	Tg2576	Tg2576+ Trolox (i.p)	WT	Tg2576	Tg2576+ Trolox (i.p)	WT	Tg2576	Tg2576+ Trolox (i.p)
-84.5 \pm 1.3	-81.8 \pm 1.0	-80.4 \pm 1.5	161.6 \pm 7.0	158.8 \pm 9.5	149.7 \pm 7.7	181.1 \pm 6.7	173.5 \pm 7.7	193.8 \pm 12.0

Table 1. The threshold current for AP generation and passive electrical properties of DG-GCs

There was no significant difference among the WT, Tg2576, and Tg2576 + Trolox (i.p.) DG-GCs.

DISCUSSION

Co–relation between deficits of Ca²⁺ buffering and Kv4.1 downregulation

As the CB is typically a mobile fast Ca²⁺ buffer, previous studies on the role of CB mostly focused on how it affects the shaping of the spatiotemporal extent of Ca²⁺ signals. Selective genetic deletion of CB in cerebellar Purkinje neuron results in deficits in motor coordination (Barski et al., 2003), while CB antisense transgenic mice with reduced CB expression in the hippocampus showed selective impairments in spatial learning (Molinari et al., 1996). Both phenotypes were understood by the alteration of the time course or amplitude of synaptically evoked Ca²⁺ transients, which in turn causes dysregulation of long–term depression or potentiation which is critical for behavioral control. In presynaptic terminals containing CB, Ca²⁺ buffer saturation mechanism, for which CB is responsible, was shown to contribute to paired pulse facilitation (Blatow et al., 2003). My results show for the first time that Ca²⁺ dysregulation caused by the loss of fast Ca²⁺ buffer CB can

affect gene expression. Since CB also acts as an activity-dependent Ca^{2+} sensor (Schmidt et al., 2005), it is also possible that the consequence of CBKO is attributable to the failure of CB actions as a Ca^{2+} sensor, not related with the dysregulation of Ca^{2+} homeostasis. Such possibility can be ruled out by the results obtained from Tg2576 mice. The phenotype in DG-GCs in 1–2 months old Tg2576 mice correlates with the reduction in Ca^{2+} buffer capacity, supporting the idea that dysregulation of Ca^{2+} signals caused by reduced Ca^{2+} buffering is responsible for these alterations. Another important finding obtained from Tg2576 mice is that $A\beta$ -induced impairment of Ca^{2+} buffering is restored by short-term treatment (1 hr) with antioxidant, but excitability and I_{4-AP} in DG-GCs were normalized only after long-term treatment with antioxidant (1 wk). These results imply that ion channel remodeling is not an immediate consequence of dysregulated Ca^{2+} signals, but requires long-term dysregulation that lasts at least more than an hour, possibly a week.

Kv4 families, consisting of Kv4.1, Kv4.2, and Kv4.3, are highly expressed in the hippocampus (Serodio and Rudy, 1998). Kv4.2 and Kv4.3 are known to encode A-type K^+ current, one

of the key determinants of neuronal excitability (Norris and Nerbonne, 2010). In particular, roles of Kv4.2 are well studied in CA1-PCs (Chen et al., 2006; Kim et al., 2005), where activity-dependent trafficking of Kv4.2 regulates dendritic excitability (Kim et al., 2007). In experimental temporal epilepsy models, transcriptional and posttranslational modulation of Kv4.2 was shown to underlie reduction of I_A and increase in dendritic excitability (Bernard et al., 2004; Lugo et al., 2008). Pathophysiological relevance of Kv4.2 was further suggested by the identification of Kv4.2 mutation in a patient with TLE (Singh et al., 2006). But, the information about the role of Kv4.1 in neuronal excitability is very limited and the involvement of Kv4.1 in pathogenesis of any brain disease has never been reported for either human patients or animal models (D'Adamo et al., 2013). My study demonstrates the physiological significance of Kv4.1 in DG-GCs and its relevance to hyperexcitability. Furthermore, I found that dysregulation of Ca^{2+} signals caused by CB dysfunction induces selective downregulation of Kv4.1 mRNA expression, without affecting Kv4.2 or Kv4.3 mRNA expression, revealing that transcriptional regulation of Kv4.1 is distinctive from other Kv4

genes.

Reduction of sustained I_{4-AP} , hyperexcitability of DG-GCs and epileptogenesis

I showed that Kv4.1-mediated currents are a key mechanism for limiting the firing frequency of mature DG-GCs, and that the reduction of Kv4.1 expression in Tg2576 mice results in hyperexcitability of DG-GCs. I showed that Tg2576 mice showed impaired pattern separation, and this impairment was restored by restoring hyperexcitability of DG-GCs. From these results together with the results shown in Chapter 1, I proposed that hyperexcitability of DG-GCs underlies impaired pattern separation. In addition, hyperexcitability of DG-GCs may have implication in a high risk of seizure in AD model mice and patients.

Normally, DG is resistant to the development of epileptogenic burst discharges following disinhibition (Fricke and Prince, 1984), but during epileptogenesis, the DG undergoes multiple changes that favor seizure generation (Williams et al., 2002). Inhibitory role of hilar mossy cells to DG-GCs is regarded to be important for the DG network

(Scharfman and Myers, 2012), and a line of evidence shows that hilar mossy cells are key players in hippocampal epileptogenesis (Santhakumar et al., 2000; Toader et al., 2013). However, the role of intrinsic excitability of DG-GCs in seizure generation has not been well studied. A recent study using optogenetic control of granule cell excitability showed that activation of granule cells can induce seizure or worsen spontaneous seizure while selective inhibition of granule cells is sufficient to inhibit spontaneous seizures in a mouse model of temporal lobe epilepsy (Krook-Magnuson et al., 2015), strongly support the idea that low excitability of DG-GCs is crucial for their role as a “gate” to inhibit overexcitation in the hippocampal circuitry. A possibility that downregulation of Kv4.1 in DG-GCs as a mechanisms of increased seizure in AD needs to be investigated in future studies.

The involvement of an altered expression of a specific ion channel in $A\beta$ -associated seizure was recently proposed. It was shown that the levels of interneuron specific and parvalbumin cell-predominant voltage-gated sodium channel subunit Nav1.1 are reduced in L2/3 of the parietal cortex in 4 to

7 months old hAPP mice (Verret et al., 2012). Because restoring the Nav1.1 levels increased the inhibitory synaptic activity and gamma oscillations, they concluded that the parvalbumin cell dysfunction caused by the reduced Nav1.1 contributes to abnormalities in oscillatory rhythms in hAPP mice and possibly in AD (Verret et al., 2012). Furthermore, the depolarized RMP in layer 2/3 PCs (Minkeviciene et al., 2009) have been suggested as mechanisms for $A\beta$ -induced seizure. However, there are other alterations in AD mice that are likely to serve to counteract $A\beta$ -induced neuronal hyperexcitability, such as the enhancement of GABAergic inhibitory function (Palop et al., 2007) and inhibitory effects of $A\beta$ on synaptic transmission (Walsh et al., 2002). These alterations may contribute to reducing the threshold for seizure generation, while hyperexcitability of DG-GCs may contribute more directly to seizure generation.

DG-GCs are early targets for AD pathogenesis

In spite that DG withstands the formation of plaques, tangles and neuronal death until late stages of AD, DG is suggested as an early target of amyloid pathology (Ohm, 2007; Palmer and

Good, 2011). These studies together with my previous study are in support with this idea, providing a mechanistic understanding of the pathogenesis of AD at an early stage. I found dysregulation of Ca^{2+} signaling in DG-GCs in 1–2 months old Tg2576 mice, where mitochondrial Ca^{2+} uptake is selectively impaired (Lee et al., 2012) and endogenous Ca^{2+} buffer capacity is significantly reduced (Fig. 1). I further investigated underlying mechanisms and provided evidence suggesting that oxidative stress associated with $\text{A}\beta_{1-42}$ commonly underlies the impairment of mitochondrial Ca^{2+} uptake and reduction in Ca^{2+} buffering: 1) Exogenous application of oligomeric $\text{A}\beta_{1-42}$ induces the same symptoms, 2) both impairments in Tg2576 are restored by anti-oxidant treatment, 3) $\text{A}\beta_{1-42}$ level in the DG region of the Tg2576 mouse brain is higher than that in other areas (0.3 ng/mg vs 0.15 ng/mg). Finally, I explored the pathophysiological significance of the impairment of Ca^{2+} signaling mechanisms in Tg2576 DG-GCs, and found that impairment of each mechanism causes a specific symptom. Impairment of mitochondrial Ca^{2+} uptake leads to the impairment of post-tetanic potentiation in mossy fiber-CA3 synapse (Lee et al.,

2012), while impaired Ca^{2+} buffering leads to neuronal hyperexcitability (Figs. 1 and 2). These results imply that DG is most susceptible to $\text{A}\beta$ -induced oxidative changes and plays key roles in pathogenesis from the early stage of AD.

Loss of CB in DG was recognized early in AD patients (Iacopino and Christakos, 1990) and its reduction was shown to be tightly linked to AD-related cognitive deficits (Palop et al., 2003). I showed that functional impairment of Ca^{2+} buffering in DG-GCs occurs much earlier and more severe than the reduction of CB expression. Based on the report that oxidized CB has low Ca^{2+} affinity (Cedervall et al., 2005) and that Ca^{2+} buffering capacity in Tg2576 DG-GCs is restored by antioxidant (Fig. 6), I proposed $\text{A}\beta$ -induced oxidative stress as a principal mechanism for the reduced Ca^{2+} buffering, but it remains to be investigated whether CB is indeed oxidized in the Tg2576 DG-GCs. Considering that oxidative stress is also known to be involved in other neurodegenerative diseases, it will be also important to investigate whether CB dysfunction occurs under the oxidative stress associated with other diseases.

REFERENCES

- Airaksinen, M.S., Eilers, J., Garaschuk, O., Thoenen, H., Konnerth, A., and Meyer, M. (1997). Ataxia and altered dendritic calcium signaling in mice carrying a targeted null mutation of the calbindin-D_{28k} gene. *Proceedings of the National Academy of Sciences of the United States of America* 94, 1488–1493.
- Altar, C.A., Jurata, L.W., Charles, V., Lemire, A., Liu, P., Bukhman, Y., Young, T.A., Bullard, J., Yokoe, H., Webster, M.J., *et al.* (2005). Deficient hippocampal neuron expression of proteasome, ubiquitin, and mitochondrial genes in multiple schizophrenia cohorts. *Biological psychiatry* 58, 85–96.
- Amatniek, J.C., Hauser, W.A., DelCastillo–Castaneda, C., Jacobs, D.M., Marder, K., Bell, K., Albert, M., Brandt, J., and Stern, Y. (2006). Incidence and predictors of seizures in patients with Alzheimer's disease. *Epilepsia* 47, 867–872.
- Backman, L., Jones, S., Berger, A.K., Laukka, E.J., and Small, B.J. (2005). Cognitive impairment in preclinical Alzheimer's disease: a meta–analysis. *Neuropsychology* 19, 520–531.
- Bakker, A., Krauss, G.L., Albert, M.S., Speck, C.L., Jones, L.R.,

Stark, C.E., Yassa, M.A., Bassett, S.S., Shelton, A.L., and Gallagher, M. (2012). Reduction of hippocampal hyperactivity improves cognition in amnesic mild cognitive impairment. *Neuron* 74, 467–474.

Baldwin, T.J., Tsaur, M.L., Lopez, G.A., Jan, Y.N., and Jan, L.Y. (1991). Characterization of a mammalian cDNA for an inactivating voltage-sensitive K⁺ channel. *Neuron* 7, 471–483.

Barski, J.J., Hartmann, J., Rose, C.R., Hoebeek, F., Morl, K., Noll-Hussong, M., De Zeeuw, C.I., Konnerth, A., and Meyer, M. (2003). Calbindin in cerebellar Purkinje cells is a critical determinant of the precision of motor coordination. *The Journal of neuroscience : the official journal of the Society for Neuroscience* 23, 3469–3477.

Battefeld, A., Tran, B.T., Gavrilis, J., Cooper, E.C., and Kole, M.H. (2014). Heteromeric Kv7.2/7.3 channels differentially regulate action potential initiation and conduction in neocortical myelinated axons. *The Journal of neuroscience : the official journal of the Society for Neuroscience* 34, 3719–3732.

Beck, H., Clusmann, H., Kral, T., Schramm, J., Heinemann, U., and Elger, C.E. (1997). Potassium currents in acutely isolated human hippocampal dentate granule cells. *The Journal of*

physiology 498 (Pt 1), 73–85.

Bernard, C., Anderson, A., Becker, A., Poolos, N.P., Beck, H., and Johnston, D. (2004). Acquired dendritic channelopathy in temporal lobe epilepsy. *Science* 305, 532–535.

Birnbaum, S.G., Varga, A.W., Yuan, L.L., Anderson, A.E., Sweatt, J.D., and Schrader, L.A. (2004). Structure and function of Kv4–family transient potassium channels. *Physiological reviews* 84, 803–833.

Blatow, M., Caputi, A., Burnashev, N., Monyer, H., and Rozov, A. (2003). Ca^{2+} buffer saturation underlies paired pulse facilitation in calbindin–D_{28k}–containing terminals. *Neuron* 38, 79–88.

Bourdeau, M.L., Morin, F., Laurent, C.E., Azzi, M., and Lacaille, J.C. (2007). Kv4.3–mediated A–type K^+ currents underlie rhythmic activity in hippocampal interneurons. *The Journal of neuroscience : the official journal of the Society for Neuroscience* 27, 1942–1953.

Browne, D.L., Gancher, S.T., Nutt, J.G., Brunt, E.R., Smith, E.A., Kramer, P., and Litt, M. (1994). Episodic ataxia/myokymia syndrome is associated with point mutations in the human potassium channel gene, KCNA1. *Nat Genet* 8, 136–140.

Brundel, B.J., Henning, R.H., Kampinga, H.H., Van Gelder, I.C.,

and Crijns, H.J. (2002). Molecular mechanisms of remodeling in human atrial fibrillation. *Cardiovascular research* 54, 315–324.

Brundel, B.J.J.M., Van Gelder, I.C., Henning, R.H., Tieleman, R.G., Tuinenburg, A.E., Wietses, M., Grandjean, J.G., Van Gilst, W.H., and Crijns, H.J.G.M. (2001). Ion Channel Remodeling Is Related to Intraoperative Atrial Effective Refractory Periods in Patients With Paroxysmal and Persistent Atrial Fibrillation. *Circulation* 103, 684–690.

Carter, D.S., Harrison, A.J., Falenski, K.W., Blair, R.E., and DeLorenzo, R.J. (2008). Long-term decrease in calbindin-D_{28K} expression in the hippocampus of epileptic rats following pilocarpine-induced status epilepticus. *Epilepsy research* 79, 213–223.

Cedervall, T., Berggard, T., Borek, V., Thulin, E., Linse, S., and Akerfeldt, K.S. (2005). Redox sensitive cysteine residues in calbindin-D_{28k} are structurally and functionally important. *Biochemistry* 44, 684–693.

Celio, M.R. (1990). Calbindin-D_{28k} and parvalbumin in the rat nervous system. *Neuroscience* 35, 375–475.

Chen, P., Ratcliff, G., Belle, S.H., Cauley, J.A., DeKosky, S.T., and Ganguli, M. (2001). Patterns of cognitive decline in

presymptomatic Alzheimer disease: a prospective community study. *Archives of general psychiatry* 58, 853–858.

Chen, X., Yuan, L.L., Zhao, C., Birnbaum, S.G., Frick, A., Jung, W.E., Schwarz, T.L., Sweatt, J.D., and Johnston, D. (2006). Deletion of Kv4.2 gene eliminates dendritic A-type K⁺ current and enhances induction of long-term potentiation in hippocampal CA1 pyramidal neurons. *The Journal of neuroscience : the official journal of the Society for Neuroscience* 26, 12143–12151.

Cirrito, J.R., Yamada, K.A., Finn, M.B., Sloviter, R.S., Bales, K.R., May, P.C., Schoepp, D.D., Paul, S.M., Mennerick, S., and Holtzman, D.M. (2005). Synaptic activity regulates interstitial fluid amyloid-beta levels in vivo. *Neuron* 48, 913–922.

Cudmore, R.H., Fronzaroli-Molinieres, L., Giraud, P., and Debanne, D. (2010). Spike-time precision and network synchrony are controlled by the homeostatic regulation of the D-type potassium current. *The Journal of neuroscience : the official journal of the Society for Neuroscience* 30, 12885–12895.

D'Adamo, M.C., Catacuzzeno, L., Di Giovanni, G., Franciolini, F., and Pessia, M. (2013). K channelopathy: progress in the

neurobiology of potassium channels and epilepsy. *Frontiers in cellular neuroscience* 7, 134.

Dieni, C.V., Nietz, A.K., Panichi, R., Wadiche, J.I., and Overstreet-Wadiche, L. (2013). Distinct determinants of sparse activation during granule cell maturation. *The Journal of neuroscience : the official journal of the Society for Neuroscience* 33, 19131–19142.

Elias, M.F., Beiser, A., Wolf, P.A., Au, R., White, R.F., and D'Agostino, R.B. (2000). The preclinical phase of alzheimer disease: A 22-year prospective study of the Framingham Cohort. *Archives of neurology* 57, 808–813.

Fricke, R.A., and Prince, D.A. (1984). Electrophysiology of dentate gyrus granule cells. *Journal of neurophysiology* 51, 195–209.

Grissmer, S., Nguyen, A.N., Aiyar, J., Hanson, D.C., Mather, R.J., Gutman, G.A., Karmilowicz, M.J., Auperin, D.D., and Chandy, K.G. (1994). Pharmacological characterization of five cloned voltage-gated K⁺ channels, types Kv1.1, 1.2, 1.3, 1.5, and 3.1, stably expressed in mammalian cell lines. *Molecular pharmacology* 45, 1227–1234.

Hamon, B., Audinat, E., Gibelin, N., and Crepel, F. (1995).

Calcium-dependent, slowly inactivating potassium currents in cultured neurons of rat neocortex. *Experimental brain research* 107, 197–204.

Hauser, W.A., Morris, M.L., Heston, L.L., and Anderson, V.E. (1986). Seizures and myoclonus in patients with Alzheimer's disease. *Neurology* 36, 1226–1230.

Helmchen, F., Imoto, K., and Sakmann, B. (1996). Ca^{2+} buffering and action potential-evoked Ca^{2+} signaling in dendrites of pyramidal neurons. *Biophysical journal* 70, 1069–1081.

Hoffman, D.A., Magee, J.C., Colbert, C.M., and Johnston, D. (1997). K^+ channel regulation of signal propagation in dendrites of hippocampal pyramidal neurons. *Nature* 387, 869–875.

Hunsaker, M.R., Rosenberg, J.S., and Kesner, R.P. (2008). The role of the dentate gyrus, CA3a,b, and CA3c for detecting spatial and environmental novelty. *Hippocampus* 18, 1064–1073.

Hyun, J.H., Eom, K., Lee, K.H., Ho, W.K., and Lee, S.H. (2013). Activity-dependent downregulation of D-type K^+ channel subunit Kv1.2 in rat hippocampal CA3 pyramidal neurons. *The Journal of physiology* 591, 5525–5540.

Iacopino, A.M., and Christakos, S. (1990). Specific reduction of calcium-binding protein (28-kilodalton calbindin-D) gene expression in aging and neurodegenerative diseases. *Proceedings of the National Academy of Sciences of the United States of America* 87, 4078–4082.

Ibarreta, D., Parrilla, R., and Ayuso, M.S. (1997). Altered Ca^{2+} homeostasis in lymphoblasts from patients with late-onset Alzheimer disease. *Alzheimer disease and associated disorders* 11, 220–227.

Jentsch, T.J. (2000). Neuronal KCNQ potassium channels: physiology and role in disease. *Nat Rev Neurosci* 1, 21–30.

Jinde, S., Zsiros, V., Jiang, Z., Nakao, K., Pickel, J., Kohno, K., Belforte, J.E., and Nakazawa, K. (2012). Hilar mossy cell degeneration causes transient dentate granule cell hyperexcitability and impaired pattern separation. *Neuron* 76, 1189–1200.

Johnston, J., Forsythe, I.D., and Kopp-Scheinpflug, C. (2010). Going native: voltage-gated potassium channels controlling neuronal excitability. *The Journal of physiology* 588, 3187–3200.

Kim, J., Jung, S.C., Clemens, A.M., Petralia, R.S., and Hoffman,

D.A. (2007). Regulation of dendritic excitability by activity-dependent trafficking of the A-type K^+ channel subunit Kv4.2 in hippocampal neurons. *Neuron* 54, 933–947.

Kim, J., Wei, D.S., and Hoffman, D.A. (2005). Kv4 potassium channel subunits control action potential repolarization and frequency-dependent broadening in rat hippocampal CA1 pyramidal neurones. *The Journal of physiology* 569, 41–57.

Kim, S., Matyas, F., Lee, S., Acsady, L., and Shin, H.S. (2012). Lateralization of observational fear learning at the cortical but not thalamic level in mice. *Proceedings of the National Academy of Sciences of the United States of America* 109, 15497–15501.

Krook-Magnuson, E., Armstrong, C., Bui, A., Lew, S., Oijala, M., and Soltesz, I. (2015). In vivo evaluation of the dentate gate theory in epilepsy. *The Journal of physiology* 593, 2379–2388.

Lee, S.H., Ho, W.K., and Lee, S.H. (2009). Characterization of somatic Ca^{2+} clearance mechanisms in young and mature hippocampal granule cells. *Cell calcium* 45, 465–473.

Lee, S.H., Rosenmund, C., Schwaller, B., and Neher, E. (2000). Differences in Ca^{2+} buffering properties between excitatory and inhibitory hippocampal neurons from the rat. *Journal of Physiology* 525, 405–418.

Lee, S.H.K., K. R., Ryu, S.Y., Son, S., Hong, H.S., Mook-Jung, I., and Ho, W.K. (2012). Impaired short-term plasticity in mossy fiber synapses caused by mitochondrial dysfunction of dentate granule cells is the earliest synaptic deficit in a mouse model of Alzheimer's disease. *The Journal of neuroscience : the official journal of the Society for Neuroscience* 32, 5953–5963.

Leutgeb, J.K., Leutgeb, S., Moser, M.B., and Moser, E.I. (2007). Pattern separation in the dentate gyrus and CA3 of the hippocampus. *Science* 315, 961–966.

Locke, R.E., and Nerbonne, J.M. (1997). Role of voltage-gated K^+ currents in mediating the regular-spiking phenotype of callosal-projecting rat visual cortical neurons. *Journal of neurophysiology* 78, 2321–2335.

Lugo, J.N., Barnwell, L.F., Ren, Y., Lee, W.L., Johnston, L.D., Kim, R., Hrachovy, R.A., Sweatt, J.D., and Anderson, A.E. (2008). Altered phosphorylation and localization of the A-type channel, Kv4.2 in status epilepticus. *J Neurochem* 106, 1929–1940.

Luthi, A., Gahwiler, B.H., and Gerber, U. (1996). A slowly inactivating potassium current in CA3 pyramidal cells of rat hippocampus in vitro. *The Journal of neuroscience : the official*

journal of the Society for Neuroscience 16, 586–594.

Magloczky, Z., Halasz, P., Vajda, J., Czirjak, S., and Freund, T.F. (1997). Loss of Calbindin-D_{28K} immunoreactivity from dentate granule cells in human temporal lobe epilepsy. *Neuroscience* 76, 377–385.

Marin–Burgin, A., Mongiat, L.A., Pardi, M.B., and Schinder, A.F. (2012). Unique processing during a period of high excitation/inhibition balance in adult–born neurons. *Science* 335, 1238–1242.

Marr, D. (1971). Simple memory: a theory for archicortex. *Philosophical transactions of the Royal Society of London Series B, Biological sciences* 262, 23–81.

Martina, M., Schultz, J.H., Ehmke, H., Monyer, H., and Jonas, P. (1998). Functional and molecular differences between voltage–gated K⁺ channels of fast–spiking interneurons and pyramidal neurons of rat hippocampus. *The Journal of neuroscience : the official journal of the Society for Neuroscience* 18, 8111–8125.

Martinello, K., Huang, Z., Lujan, R., Tran, B., Watanabe, M., Cooper, E.C., Brown, D.A., and Shah, M.M. (2015). Cholinergic afferent stimulation induces axonal function plasticity in adult hippocampal granule cells. *Neuron* 85, 346–363.

McHugh, T.J., Jones, M.W., Quinn, J.J., Balthasar, N., Coppari, R., Elmquist, J.K., Lowell, B.B., Fanselow, M.S., Wilson, M.A., and Tonegawa, S. (2007). Dentate gyrus NMDA receptors mediate rapid pattern separation in the hippocampal network. *Science* 317, 94–99.

McNaughton, B., and Nadel, L. (1990). Hebb–Marr networks and the neurobiological representation of action in space. In *Neuroscience and Connectionist Theory*, M. Gluck, and D. Rumelhart, eds. (Lawrence Erlbaum Associates), pp. 1–63.

McNaughton, N., and Morris, R.G. (1987). Chlordiazepoxide, an anxiolytic benzodiazepine, impairs place navigation in rats. *Behavioural brain research* 24, 39–46.

Minkeviciene, R., Rheims, S., Dobszay, M.B., Zilberter, M., Hartikainen, J., Fulop, L., Penke, B., Zilberter, Y., Harkany, T., Pitkanen, A., and Tanila, H. (2009). Amyloid beta–induced neuronal hyperexcitability triggers progressive epilepsy. *The Journal of neuroscience : the official journal of the Society for Neuroscience* 29, 3453–3462.

Miyakawa, T., Leiter, L.M., Gerber, D.J., Gainetdinov, R.R., Sotnikova, T.D., Zeng, H., Caron, M.G., and Tonegawa, S. (2003). Conditional calcineurin knockout mice exhibit multiple

abnormal behaviors related to schizophrenia. Proceedings of the National Academy of Sciences of the United States of America 100, 8987–8992.

Molinari, S., Battini, R., Ferrari, S., Pozzi, L., Killcross, A.S., Robbins, T.W., Jouvenceau, A., Billard, J.M., Dutar, P., Lamour, Y., *et al.* (1996). Deficits in memory and hippocampal long-term potentiation in mice with reduced calbindin-D_{28K} expression. Proceedings of the National Academy of Sciences of the United States of America 93, 8028–8033.

Mongiati, L.A., Esposito, M.S., Lombardi, G., and Schinder, A.F. (2009). Reliable activation of immature neurons in the adult hippocampus. PloS one 4, e5320.

Mucke, L., Masliah, E., Yu, G.Q., Mallory, M., Rockenstein, E.M., Tatsuno, G., Hu, K., Kholodenko, D., Johnson–Wood, K., and McConlogue, L. (2000). High-level neuronal expression of abeta 1–42 in wild-type human amyloid protein precursor transgenic mice: synaptotoxicity without plaque formation. The Journal of neuroscience : the official journal of the Society for Neuroscience 20, 4050–4058.

Muller, A., Kukley, M., Stausberg, P., Beck, H., Muller, W., and Dietrich, D. (2005). Endogenous Ca²⁺ buffer concentration and

Ca²⁺ microdomains in hippocampal neurons. *The Journal of neuroscience : the official journal of the Society for Neuroscience* 25, 558–565.

Nakamura, T.Y., Nandi, S., Pountney, D.J., Artman, M., Rudy, B., and Coetzee, W.A. (2001). Different effects of the Ca²⁺-binding protein, KChIP1, on two Kv4 subfamily members, Kv4.1 and Kv4.2. *FEBS letters* 499, 205–209.

Neher, E., and Augustine, G.J. (1992). Calcium gradients and buffers in bovine chromaffin cells. *The Journal of physiology* 450, 273–301.

Nerbonne, J.M., Gerber, B.R., Norris, A., and Burkhalter, A. (2008). Electrical remodelling maintains firing properties in cortical pyramidal neurons lacking KCND2-encoded A-type K⁺ currents. *The Journal of physiology* 586, 1565–1579.

Noebels, J.L. (2001). Modeling human epilepsies in mice. *Epilepsia* 42 Suppl 5, 11–15.

Norris, A.J., and Nerbonne, J.M. (2010). Molecular dissection of I_A in cortical pyramidal neurons reveals three distinct components encoded by Kv4.2, Kv4.3, and Kv1.4 alpha-subunits. *The Journal of neuroscience : the official journal of the Society for Neuroscience* 30, 5092–5101.

O'Reilly, R.C., and McClelland, J.L. (1994). Hippocampal conjunctive encoding, storage, and recall: avoiding a trade-off. *Hippocampus* 4, 661–682.

Ohashi, N., Mitamura, H., Tanimoto, K., Fukuda, Y., Kinebuchi, O., Kurita, Y., Shiroshita-Takeshita, A., Miyoshi, S., Hara, M., Takatsuki, S., and Ogawa, S. (2004). A Comparison between Calcium Channel Blocking Drugs with Different Potencies for T- and L-Type Channels in Preventing Atrial Electrical Remodeling. *Journal of Cardiovascular Pharmacology* 44, 386–392.

Ohm, T.G. (2007). The dentate gyrus in Alzheimer's disease. *Progress in brain research* 163, 723–740.

Pak, M.D., Baker, K., Covarrubias, M., Butler, A., Ratcliffe, A., and Salkoff, L. (1991). mShal, a subfamily of A-type K⁺ channel cloned from mammalian brain. *Proceedings of the National Academy of Sciences of the United States of America* 88, 4386–4390.

Palmer, A., and Good, M. (2011). Hippocampal synaptic activity, pattern separation and episodic-like memory: implications for mouse models of Alzheimer's disease pathology. *Biochemical Society transactions* 39, 902–909.

Palop, J.J., Chin, J., Roberson, E.D., Wang, J., Thwin, M.T., Bien-Ly, N., Yoo, J., Ho, K.O., Yu, G.Q., Kreitzer, A., *et al.* (2007). Aberrant excitatory neuronal activity and compensatory remodeling of inhibitory hippocampal circuits in mouse models of Alzheimer's disease. *Neuron* 55, 697–711.

Palop, J.J., Jones, B., Kekonius, L., Chin, J., Yu, G.Q., Raber, J., Masliah, E., and Mucke, L. (2003). Neuronal depletion of calcium-dependent proteins in the dentate gyrus is tightly linked to Alzheimer's disease-related cognitive deficits. *Proceedings of the National Academy of Sciences of the United States of America* 100, 9572–9577.

Palop, J.J., and Mucke, L. (2009). Epilepsy and cognitive impairments in Alzheimer disease. *Archives of neurology* 66, 435–440.

Ramakers, G.M., and Storm, J.F. (2002). A postsynaptic transient K⁺ current modulated by arachidonic acid regulates synaptic integration and threshold for LTP induction in hippocampal pyramidal cells. *Proceedings of the National Academy of Sciences of the United States of America* 99, 10144–10149.

Riazanski, V., Becker, A., Chen, J., Sochivko, D., Lie, A.,

Wiestler, O.D., Elger, C.E., and Beck, H. (2001). Functional and molecular analysis of transient voltage-dependent K^+ currents in rat hippocampal granule cells. *The Journal of physiology* 537, 391–406.

Rolls, E.T. (2013). The mechanisms for pattern completion and pattern separation in the hippocampus. *Frontiers in systems neuroscience* 7, 74.

Rolls, E.T., and Kesner, R.P. (2006). A computational theory of hippocampal function, and empirical tests of the theory. *Progress in neurobiology* 79, 1–48.

Roy, D.S., Arons, A., Mitchell, T.I., Pignatelli, M., Ryan, T.J., and Tonegawa, S. (2016). Memory retrieval by activating engram cells in mouse models of early Alzheimer's disease. *Nature* 531, 508–512.

Sanchez, D., López-López, J.R., Pérez-García, M.T., Sanz-Alfayate, G., Obeso, A., Ganfornina, M.D., and Gonzalez, C. (2002). Molecular identification of $Kv\alpha$ subunits that contribute to the oxygen-sensitive K^+ current of chemoreceptor cells of the rabbit carotid body. *The Journal of physiology* 542, 369–382.

Santhakumar, V., Bender, R., Frotscher, M., Ross, S.T., Hollrigel,

G.S., Toth, Z., and Soltesz, I. (2000). Granule cell hyperexcitability in the early post-traumatic rat dentate gyrus: the 'irritable mossy cell' hypothesis. *The Journal of physiology* 524 Pt 1, 117–134.

Scharfman, H.E., and Myers, C.E. (2012). Hilar mossy cells of the dentate gyrus: a historical perspective. *Frontiers in neural circuits* 6, 106.

Schmidt-Hieber, C., Jonas, P., and Bischofberger, J. (2004). Enhanced synaptic plasticity in newly generated granule cells of the adult hippocampus. *Nature* 429, 184–187.

Schmidt, H., Schwaller, B., and Eilers, J. (2005). Calbindin-D_{28k} targets myo-inositol monophosphatase in spines and dendrites of cerebellar Purkinje neurons. *Proceedings of the National Academy of Sciences of the United States of America* 102, 5850–5855.

Schwaller, B. (2012). The use of transgenic mouse models to reveal the functions of Ca²⁺ buffer proteins in excitable cells. *Biochimica et biophysica acta* 1820, 1294–1303.

Serodio, P., and Rudy, B. (1998). Differential expression of Kv4 K⁺ channel subunits mediating subthreshold transient K⁺ (A-type) currents in rat brain. *Journal of neurophysiology* 79,

1081–1091.

Serodio, P., Vega–Saenz de Miera, E., and Rudy, B. (1996). Cloning of a novel component of A–type K^+ channels operating at subthreshold potentials with unique expression in heart and brain. *Journal of neurophysiology* 75, 2174–2179.

Shah, M.M., Migliore, M., Valencia, I., Cooper, E.C., and Brown, D.A. (2008). Functional significance of axonal Kv7 channels in hippocampal pyramidal neurons. *Proceedings of the National Academy of Sciences of the United States of America* 105, 7869–7874.

Shibata, R., Nakahira, K., Shibasaki, K., Wakazono, Y., Imoto, K., and Ikenaka, K. (2000). A–type K^+ current mediated by the Kv4 channel regulates the generation of action potential in developing cerebellar granule cells. *The Journal of neuroscience : the official journal of the Society for Neuroscience* 20, 4145–4155.

Singh, B., Ogiwara, I., Kaneda, M., Tokonami, N., Mazaki, E., Baba, K., Matsuda, K., Inoue, Y., and Yamakawa, K. (2006). A Kv4.2 truncation mutation in a patient with temporal lobe epilepsy. *Neurobiology of disease* 24, 245–253.

Sloviter, R.S. (1983). "Epileptic" brain damage in rats induced

by sustained electrical stimulation of the perforant path. I. Acute electrophysiological and light microscopic studies. *Brain research bulletin* 10, 675–697.

Sloviter, R.S., Bumanglag, A.V., Schwarcz, R., and Frotscher, M. (2012). Abnormal dentate gyrus network circuitry in temporal lobe epilepsy. In *Jasper's Basic Mechanisms of the Epilepsies*, J.L. Noebels, M. Avoli, M.A. Rogawski, R.W. Olsen, and A.V. Delgado–Escueta, eds. (Bethesda (MD)).

Small, B.J., Herlitz, A., Fratiglioni, L., Almkvist, O., and Backman, L. (1997). Cognitive predictors of incident Alzheimer's disease: a prospective longitudinal study. *Neuropsychology* 11, 413–420.

Stefanits, H., Ebetsberger–Dachs, G., Weis, S., and Haberler, C. (2014). Medulloblastoma with multi–lineage differentiation including myogenic and melanotic elements: a case report with molecular data. *Clinical neuropathology* 33, 122–127.

Storm, J.F. (1988). Temporal integration by a slowly inactivating K^+ current in hippocampal neurons. *Nature* 336, 379–381.

Tessier, S., Karczewski, P., Krause, E.G., Pansard, Y., Acar, C., Lang–Lazdunski, M., Mercadier, J.J., and Hatem, S.N. (1999).

Regulation of the transient outward K(+) current by Ca(2+)/calmodulin-dependent protein kinases II in human atrial myocytes. *Circulation research* 85, 810–819.

Toader, O., Forte, N., Orlando, M., Ferrea, E., Raimondi, A., Baldelli, P., Benfenati, F., and Medrihan, L. (2013). Dentate gyrus network dysfunctions precede the symptomatic phase in a genetic mouse model of seizures. *Frontiers in cellular neuroscience* 7, 138.

Treves, A., and Rolls, E.T. (1994). Computational analysis of the role of the hippocampus in memory. *Hippocampus* 4, 374–391.

van Praag, H., Schinder, A.F., Christie, B.R., Toni, N., Palmer, T.D., and Gage, F.H. (2002). Functional neurogenesis in the adult hippocampus. *Nature* 415, 1030–1034.

Vazdarjanova, A., and Guzowski, J.F. (2004). Differences in hippocampal neuronal population responses to modifications of an environmental context: evidence for distinct, yet complementary, functions of CA3 and CA1 ensembles. *The Journal of neuroscience : the official journal of the Society for Neuroscience* 24, 6489–6496.

Verret, L., Mann, E.O., Hang, G.B., Barth, A.M., Cobos, I., Ho, K.,

Devidze, N., Masliah, E., Kreitzer, A.C., Mody, I., *et al.* (2012). Inhibitory interneuron deficit links altered network activity and cognitive dysfunction in Alzheimer model. *Cell* 149, 708–721.

Walsh, D.M., Klyubin, I., Fadeeva, J.V., Cullen, W.K., Anwyl, R., Wolfe, M.S., Rowan, M.J., and Selkoe, D.J. (2002). Naturally secreted oligomers of amyloid beta protein potently inhibit hippocampal long-term potentiation in vivo. *Nature* 416, 535–539.

Walsh, D.M., and Selkoe, D.J. (2007). A beta oligomers – a decade of discovery. *J Neurochem* 101, 1172–1184.

Williams, P.A., Wuarin, J.P., Dou, P., Ferraro, D.J., and Dudek, F.E. (2002). Reassessment of the effects of cycloheximide on mossy fiber sprouting and epileptogenesis in the pilocarpine model of temporal lobe epilepsy. *Journal of neurophysiology* 88, 2075–2087.

Yamasaki, N., Maekawa, M., Kobayashi, K., Kajii, Y., Maeda, J., Soma, M., Takao, K., Tanda, K., Ohira, K., Toyama, K., *et al.* (2008). Alpha-CaMKII deficiency causes immature dentate gyrus, a novel candidate endophenotype of psychiatric disorders. *Molecular brain* 1, 1–6.

Yassa, M.A., and Stark, C.E. (2011). Pattern separation in the

hippocampus. Trends in neurosciences 34, 515–525.

국문 초록

치상회 영역은 내후각피질에서부터 오는 정보를 해마 전체에 전달해주는 주요 게이트웨이와 같은 역할을 하는 기관으로 신경조직발생이 끊임없이 일어나는 곳이다. 낮은 활동 전압의 빈도수를 가진 치상회 과립세포는 해마 의존적 기억 중 비슷한 기억들이 서로 다른 기억임을 상세히 구분하고 기억해 내는 능력인 패턴 분리력에 중요한 역할을 한다. 지금까지 흥분성 입력과 억제성 입력간의 균형이 치상회 과립세포의 낮은 흥분성을 결정하는데 중요하다고 보고되어 왔지만 치상회 과립세포의 낮은 활동전압 활동에 대해서는 연구된 바 없다. 치상회 과립세포는 성숙화 과정을 거치는 곳이며, 미성숙한 과립세포와 성숙한 과립세포는 전기생리학적으로 구분이 된다. 또한 성숙한 과립세포는 칼빈딘-D_{28K} (CB) 라는 세포 내 칼슘 완충 단백질이 발현 되어 있고, 이 단백질의 발현 감소는 인지 장애나 알츠하이머 병 환자와 질병 모델 쥐에서 관찰이 된다는 보고가 있다. 그러나 치상회 과립세포의 세포 내 칼슘 조절장애와 세포의 흥분성과의 관계에 대해 연구된 적이 없었다. 본 연구자는 한 달에서 두 달 된 정상 쥐와 알츠하이머 병 모델 쥐와 칼빈딘이 결핍된 쥐를 이용을 하여 성숙한 치상회 과립세포의 흥분성의 변화와 흥분성 조절 메커니즘을 연구 하고자 했다. 신경 세포의 흥분성을 조절

하는 채널로 잘 알려진 A 형 포타슘 채널은 Kv4.1 과 Kv4.2 와 Kv4.3 으로 구성되어 있으며, Kv4.1 채널의 발현은 다른 뇌 영역보다 치상회 영역에 높게 발현된다고 알려져 있으나 Kv4.1 채널에 관한 연구는 지금까지 거의 없다. 먼저 해마 뇌 조직에 항-Kv4.1 항체를 이용하여 면역화학염색을 하여 Kv4.1 의 발현이 치상회 과립세포에 높게 발현되어 있으며, 미성숙한 과립세포의 표지제인 항-doublecortin 항체를 이용하여 과립세포의 성숙화 단계에서 Kv4.1 의 발현 양상이 성숙한 과립세포에 상당히 높은 것을 확인하였다. 전 세포 전류 고정 기법을 통해 측정된 성숙한 과립세포 흥분성은 미성숙한 과립세포보다 낮으며, 항-Kv4.1 항체 주입에 의해 활동전압의 빈도수가 크게 증가한 것을 관찰 하였다. 동일한 실험을 미성숙한 과립세포와 CA1 피라미달 세포에 한 결과 이 두 세포의 흥분성은 변화하지 않았다. 이것으로 성숙한 과립세포의 낮은 흥분성은 Kv4.1 채널에 의해 조절이 됨을 확인하였다. 전 세포 전압고정 기법으로 Kv4.1의 전류를 측정하여 Kv4.1의 특성이 기존에 알려진 빠르게 활성화 되었다가 빠르게 비활성화 되는 A 형 포타슘 채널의 특성과는 달리 느리게 비활성화 되고 세포 내 칼슘에 의해 조절되는 것을 확인 하였다. 흥미롭게도, 칼빈딘이 결핍된 쥐와 알츠하이머 병 모델 쥐의 치상회 성숙한 과립세포의 흥분성이 증가 되어 있는 것을 발견 하였고, 실시간 역전사 중합효소 연쇄 반응 실험을 통해 Kv4.1 메신저 RNA 발현이 줄어 들어 있고, Kv4.1 에 의해 매

개되는 전류도 감소한 것을 확인 하였다. 칼빈딘이 결핍된 쥐와 알츠하이머 병 모델 쥐의 치상회 과립세포의 과 흥분성이 패턴 분리 능력의 장애를 야기 하는 것을 환경적 공포 동물 행동 실험을 통해 알 수 있었다. 또한 알츠하이머 병 모델 쥐에서 치상회 과립세포 내 칼슘 완충 수용력이 세포 내 칼슘 완충 단백질인 칼빈딘이 결핍된 쥐와 같은 정도로 떨어져 있으며, 외부적으로 아미로이드 베타 올리고머의 단백질을 처리하였을 때에도 동일한 결과가 나타났다. 이 현상은 항산화제인 Trolox 전 처리로 정상 쥐와 같은 정도의 세포 내 칼슘 완충 수용력으로 회복 할 수 있는 것을 확인하였다. 알츠하이머 병 모델 쥐에서 나타난 변화들은 1 주일 동안 Trolox 를 복용투여 한 결과 Kv4.1 에 의해 매개되는 전류의 회복과 정상 쥐와 같은 성숙한 과립세포의 흥분성을 보이는 것을 확인 할 수 있었다. 이 모든 실험 결과들을 종합 하였을 때, Kv4.1 채널은 치상회의 성숙된 과립세포의 과 흥분상태를 막아주는 아주 중요한 조절 제 역할을 하며, 이는 해마 의존적인 기억인 패턴 분리 능력에 중요하다는 점을 시사한다. 또한 칼빈딘이 결핍된 쥐와 알츠하이머 병 모델 쥐에서의 Kv4.1 채널 발현 감소는 칼슘 조절장애가 유발되는 다양한 조건에서 Kv4.1 채널의 병태생리학적 중요성을 시사한다.

주요어 : 내제적 흥분성, 치아이랑 성숙한 과립세포, A 형 포타슘 채널, Kv4.1, Kv4.2. 칼빈딘 D28K, 알츠하이머 병
학 번 : 2009-23550